Advances in diffraction of subnuclear waves

Laurent SCHOEFFEL
CEA Saclay/Irfu-SPP, 91191 Gif-sur-Yvette, France

October 31, 2018

Abstract

In this review, we present and discuss the most recent results on inclusive and exclusive diffractive processes at HERA and Tevatron colliders. Measurements from fixed target experiments at HERMES and Jefferson laboratory are also reviewed. The complementarity of all these results is analyzed in the context of perturbative QCD and new challenging issues in nucleon tomography are studied. A first understanding of how partons are localized in the nucleon to build orbital momenta can be addressed with these experimental results. Some prospects are outlined for new measurements in fixed target kinematic, at Jefferson laboratory and CERN, at COMPASS, or at the LHC. Of special interest is the exclusive (coherent) production of Higgs boson and heavy objects at the LHC. Based on the present knowledge, some perspectives are presented in this direction.

To be published in *Progress in Particle and Nuclear Physics*

Contents

1 Introduction

Understanding the fundamental structure of matter requires an understanding of how quarks and gluons are assembled to form hadrons. Of course, only when partons are the relevant degrees of freedom of the processes, which we design in the following as perturbative processes. The arrangement of quarks and gluons inside nucleons can be probed by accelerating electrons, hadrons or nuclei to precisely controlled energies, smashing them into a target nucleus and examining the final products. Two kinds of reactions can be considered.

The first one consists in low momentum transfer processes with particles that are hardly affected in direction or energy by the scattering process. They provide a low resolution image of the structure, which allows to map the static, overall properties of the proton (or neutron), such as shapes, sizes, and response to externally applied forces. This is the domain of form factors. They depend on the three-momentum transfer to the system. The Fourier transformation of form factors provides a direct information on the spatial distribution of charges in the nucleon.

A second type of reaction is designed to measure the population of the constituents as a function of momentum, momentum distributions, through deep inelastic scattering (DIS). It comes from higher energy processes with particles that have scored a near-direct hit on a parton inside the nucleon, providing a higher resolution probe of the nucleon structure. Such hard scattering events typically arise via electron-quark interactions or quark-antiquark annihilation processes. Nucleon can then be pictured as a large and ever-changing number of partons having appropriate distributions of momentum and spin.

Many experiments in the world located at DESY (Hamburg), Jefferson Lab or JLab (Virginia), Brookhaven (New York), Fermilab (Batavia) and CERN (Geneva) can measure these processes. Both approaches described above are complementary, but bear some drawbacks. The form factor measurements do not yield any information about the underlying dynamics of the system such as the momenta of the constituents, whereas the momentum distributions do not give any information on the spatial location of the constituents. In fact, more complete information about the microscopic structure lies in the correlation between momenta and transverse degrees of freedom. New results in this direction are presented in this review and the complementarity of these measurements, from all experiments listed above, is discussed.

2 Basics of diffraction at HERA and Tevatron

HERA was a collider where electrons or positrons of 27.6 GeV collided with protons of 920 GeV, corresponding to a center of mass energy of about 300 GeV. One of the most important experimental results from the DESY collider HERA is the observation of a significant fraction, around 10%, of large rapidity gap events in deep inelastic scattering (DIS) [1, 2, 3, 4]. In these events, the target proton emerges in the final state with a loss of a very small fraction ($x_{\mathbb{P}}$) of its energy-momentum.

In Fig. 1(a), we present this event topology, $\gamma^* p \to X\ p'$, where the virtual photon γ^* probes the proton structure and originates from the electron. Then, the final hadronic state X and the scattered proton are well separated in space (or rapidity) and a gap in rapidity can be observed in the event with no particle produced between X and the scattered proton. In the standard QCD description of DIS, such events are not expected in such an abundance since large gaps are exponentially suppressed due to color strings formed between the proton remnant and scattered partons (see Fig. 1(b)). The theoretical description of such processes, also called diffractive processes, is challenging since it must combine perturbative QCD effects of hard scattering with non perturbative phenomena of rapidity gap formation. The name diffraction in high-energy particle physics originates from the analogy between optics and nuclear high-energy scattering. In the Born approximation the equation for hadron-hadron

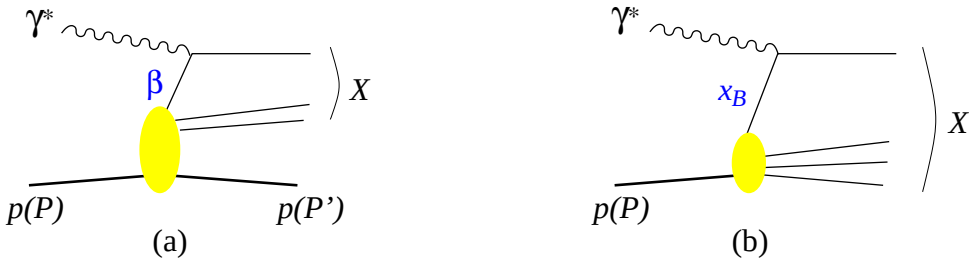

Figure 1: Parton model diagrams for deep inelastic diffractive (a) and inclusive (b) scattering observed at lepton-proton collider HERA. The variable β is the momentum fraction of the struck quark with respect to $P - P'$, and the Bjorken variable x_{Bj} its momentum fraction with respect to P.

elastic scattering amplitude can be derived from the scattering of a plane wave passing through and around an absorbing disk, resulting in an optic-like diffraction pattern for hadron scattering. The quantum numbers of the initial beam particles are conserved during the reaction and then the diffractive system is well separated in rapidity from the scattered hadron.

The early discovery of large rapidity gap events at HERA [1] has led to a renaissance of the physics of diffractive scattering in an entirely new domain, in which the large momentum transfer provides a hard scale. This observation has then revived the rapidity gap physics with hard triggers, as large-$p_\perp$ jets, at the proton-antiproton collider Tevatron (see Fig. 2). The Tevatron is a $p\bar{p}$ collider located close to Chicago at Fermilab, USA. It is presently the collider with the highest center-of-mass energy of about 2 TeV. Two main experiments are located around the ring, DØ and CDF.

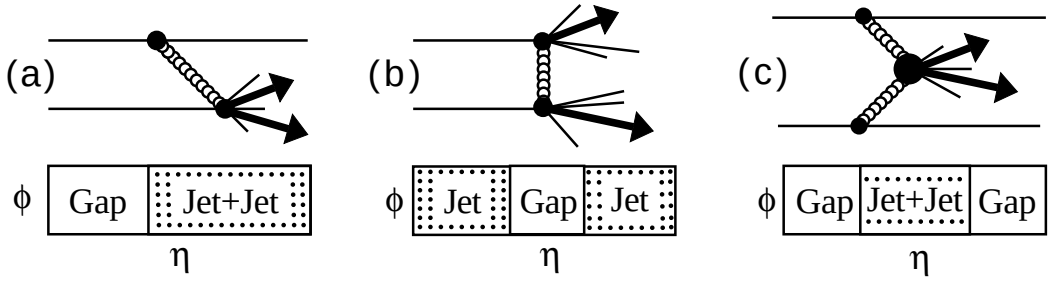

Figure 2: Schematic diagrams of topologies representative of hard diffractive processes studied by the proton-antiproton collider Tevatron.

In the single diffractive dissociation process in proton-proton scattering, $pp \to Xp$, at least one of the beam hadrons emerges intact from the collision, having lost only a small fraction of its energy and gained only a small transverse momentum. In the analogous process involving virtual photons, $\gamma^* p \to Xp$, an exchanged photon of virtuality Q^2 dissociates through its interaction with the proton at a squared four momentum transfer t to produce a hadronic system X with mass M_X. The fractional longitudinal momentum loss of the proton during the interaction is denoted $x_{I\!P}$, while the fraction of this momentum carried by the struck quark is denoted β. These variables are related to Bjorken x by $x = \beta\, x_{I\!P}$ (see Fig. 3).

Using the standard vocable, the vacuum/colorless exchange involved in the diffractive interaction is called Pomeron in this review. Whether the existence of such hard scales makes the diffractive processes tractable within perturbative QCD or not has been a subject of intense theoretical and experimental research during the past decade.

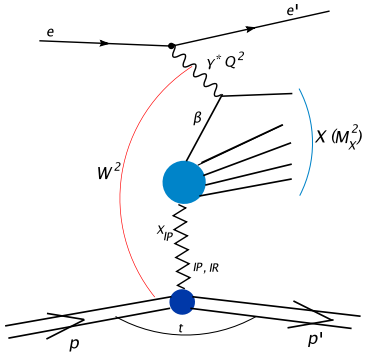

Figure 3: Diffractive kinematics.

3 Observation of diffractive events at HERA

3.1 The rapidity gap events

Let us start by giving a real example of a diffractive event in HERA experiments. See Fig. 4, which is the (exact) experimental reproduction of Fig. 1. A typical DIS event as shown in the upper plot of Fig. 4 is $ep \to eX$ where electron and jets are produced in the final state. The electron is scattered in the backward detector[1] (right of the figure) whereas some hadronic activity is present in the forward region of the detector. The proton is thus completely destroyed and the interaction leads to jets and proton remnants directly observable in the detector.

The fact that much energy is observed in the forward region is due to color exchange between the scattered jet and the proton remnants. However, for events that we have called diffractive, the situation is completely different. Such events appear like the one shown in the bottom of Fig. 4. The electron is still present in the backward detector, there is still some hadronic activity (jets) in the LAr calorimeter, but no energy above noise level is deposited in the forward part of the detectors. In other words, there is no color exchange between the proton and the produced jets. The reaction can then be written as $ep \to epX$. This is also called a Large Rapidity Gap (LRG) event, and constitutes an efficient experimental method to tag diffractive events.

3.2 Proton tagging

A second experimental technique to detect diffractive events is to tag the outgoing proton. The idea is then to detect directly the intact proton in the final state. The proton loses a small fraction of its energy and is thus scattered at very small angle with respect to the beam direction. Some special detectors called roman pots can be used to detect the protons close to the beam.

The basic idea is simple. The roman pot detectors are located far away from the interaction point and can move close to the beam, when the beam is stable, to detect protons scattered at vary small angles.

The inconvenience is that the kinematical reach of those detectors is much smaller than with the rapidity gap method. On the other hand, the advantage is that it gives a clear signal of diffraction since it measures the diffracted proton directly. A scheme of a roman pot detector as it is used by the H1 or ZEUS experiment is shown in Fig. 3.2. The beam is the horizontal line at the upper part of the figure. The detector is located in the pot itself and can move closer to the beam when the beam is stable enough (during the injection period, the detectors are protected in the home position).

[1] At HERA, the backward (resp. forward) directions are defined as the direction of the outgoing electron (resp. proton).

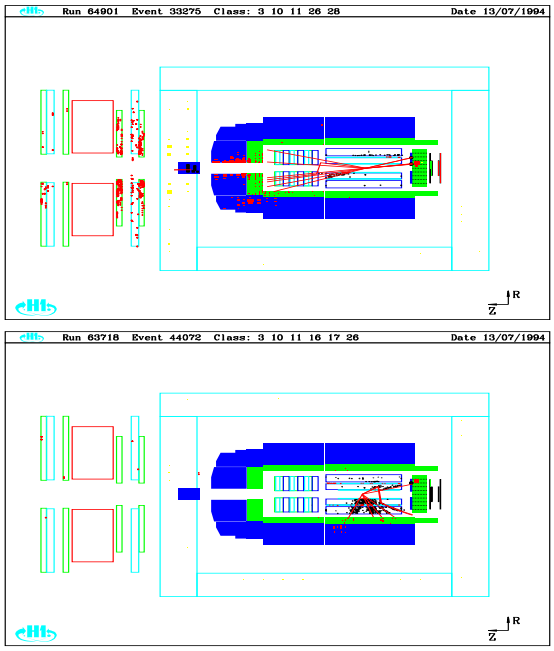

Figure 4: Usual (top) and diffractive (bottom) events in the H1 experiment at HERA. For a diffractive event, no hadronic activity is visible in the proton fragmentation region, as the proton remains intact in the diffractive process. On the contrary, for a standard DIS event, the proton is destroyed in the reaction and the flow of hadronic clusters is clearly visible in the proton fragmentation region (+z direction, i.e. forward part of the detector).

3.3 The M_X method

The third method used at HERA mainly by the ZEUS experiment is based on the fact that there is a different behavior in $\log M_X^2$, where M_X is the total invariant mass produced in the event, either for diffractive or non diffractive events. For diffractive events $d\sigma_{diff}/dM_X^2 = (s/M_X^2)^{\alpha-1} = const.$ if $\alpha \sim 1$ (which is the case for diffractive events). The ZEUS collaboration performs some fits of the $d\sigma/dM_X^2$ distribution:

$$\frac{d\sigma}{dM_X^2} = D + c\exp(b\log M_X^2) \tag{1}$$

as illustrated in Fig. 3.3 The usual non diffractive events are exponentially suppressed at high values of M_X. The difference between the observed $d\sigma/dM_X^2$ data and the exponential suppressed distribution is the diffractive contribution.

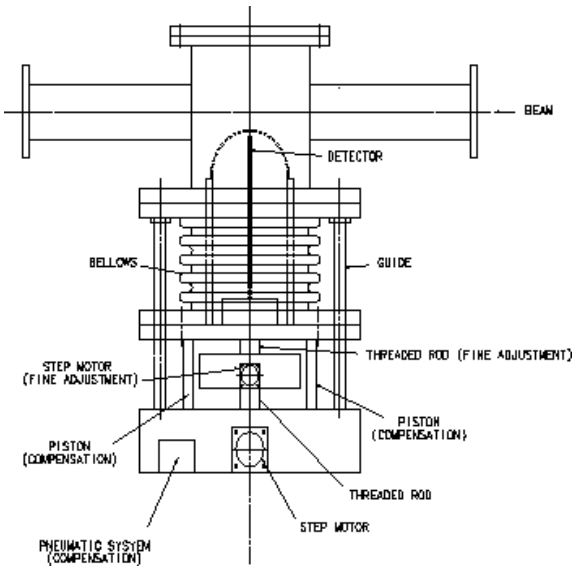

Figure 5: Scheme of a roman pot detector. The roman pot detectors are located far away from the interaction point and can move close to the beam, when the beam is stable, to detect protons scattered at vary small angles.

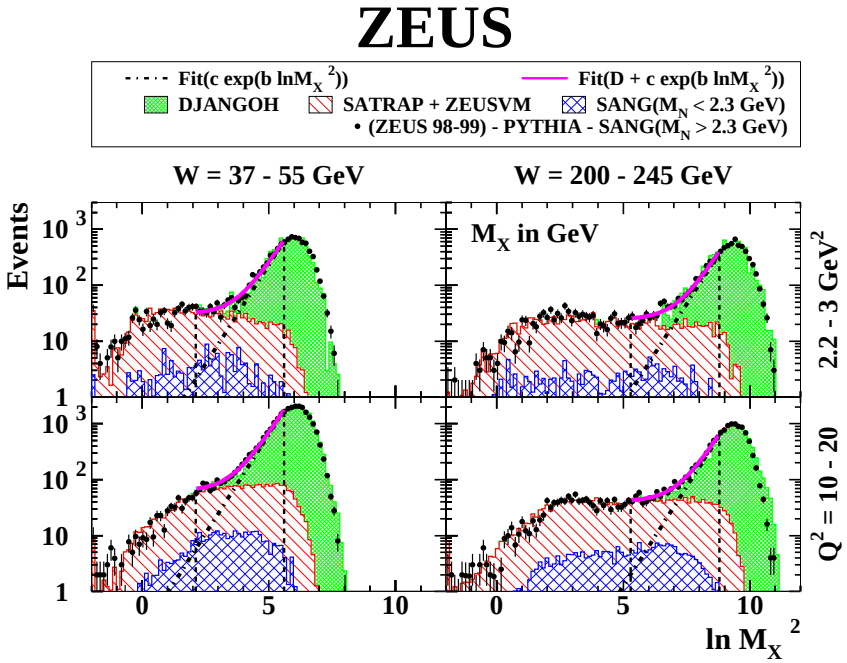

Figure 6: Illustration of the M_X method used by the ZEUS collaboration to define diffractive events. The diffractive contribution corresponds to $d\sigma_{diff}/dM_X^2 \simeq constont$, while the non diffractive part (at large M_X) leads to a shape in $\frac{d\sigma}{dM_X^2} \simeq \exp(b \log M_X^2)$.

4 Measurement of the inclusive diffractive cross section HERA

4.1 Inclusive diffraction as a leading twist process

From observation of diffractive events, using the different techniques exposed above, the inclusive diffractive cross section has been measured at HERA by H1 and ZEUS experiments over a wide kinematic range [1, 2, 3, 4]. Similarly to inclusive DIS, cross section measurements for the reaction $ep \to eXp$ are conventionally expressed in terms of the reduced diffractive cross section, $\sigma_r^{D(3)}$, which is related to the measured cross section by

$$\frac{\mathrm{d}\sigma^{ep\to eXp}}{\mathrm{d}\beta \mathrm{d}Q^2 \mathrm{d}x_{I\!P}} = \frac{4\pi\alpha^2}{\beta Q^4} \quad \left[1 - y + \frac{y^2}{2}\right] \quad \sigma_r^{D(3)}(\beta, Q^2, x_{I\!P}) \ . \tag{2}$$

At moderate inelasticities y, $\sigma_r^{D(3)}$ corresponds to the diffractive structure function $F_2^{D(3)}$ to good approximation.

Fig. 7 illustrates a first result for the diffractive cross section as a function of W for different Q^2 and M_X values. We notice that the diffractive cross section, $ep \to epX$, shows a hard dependence in the center-of-mass energy of the $\gamma^* p$ system W. Namely, we measure a W dependence of the form $\sim W^{0.6}$ for the diffractive cross section, compatible with the dependence expected for a hard process.

This first observation is fundamental and allows further studies of the diffractive process in the context of perturbative QCD (see next sections). The experimental selection of diffractive events is already a challenge but the discovery that these events build a hard scattering process is a surprise and makes the strong impact of HERA data into the field. Indeed, the extent to which diffraction, even in the presence of a hard scale, is a hard process, was rather unclear before HERA data. This has changed since then, with the arrival of accurate HERA data on diffraction in ep scattering and the realization that diffraction (measured to be a hard process) in DIS can be described in close analogy with inclusive DIS [2, 3, 4].

This is also confirmed in Fig. 8, where the ratio of diffractive to DIS cross sections is shown. This ratio is found to depend weakly on the Bjorken variable x_{Bj} (or W) at fixed values of the photon virtuality Q^2. Thus, we can conclude that diffraction in DIS is a leading twist effect with logarithmic scaling violation in Q^2, as for standard DIS. We discuss these results much further in the next sections.

4.2 Recent results on inclusive diffraction at HERA

Extensive measurements of diffractive DIS cross sections have been made by both the ZEUS and H1 collaborations at HERA, using different experimental techniques [2, 3, 4]. Of course, the comparison of these techniques provides a rich source of information to get a better understanding of their respective experimental gains and prejudices.

In Fig. 9, the basis of the last ZEUS experimental analysis is summarized [3]. Data are compared to Monte-Carlo (MC) expectations for typical variables. The MC is based on specific models for signal and backgrounds, and the good agreement with data is proof that the main ingredients of the experimental analysis are under control. These last sets of data (Fig. 9) [3] contain five to seven times more statistics than in preceding publications of diffractive cross sections, and thus opens the way to new developments in data/models comparisons.

A first relative control of the data samples is shown in Fig. 10, where the ratio of the diffractive cross sections is displayed, as obtained with the LPS and the LRG experimental techniques. The mean value of the ratio of 0.86 indicates that the LRG sample contains about 24% of proton-dissociation background, which is not present in the LPS sample. This background corresponds to events like $ep \to eXY$, where Y is a low-mass excited state of the proton (with $M_Y < 2.3$ GeV). It is obviously not present in the LPS analysis which can select specifically a proton in the final state. This is the

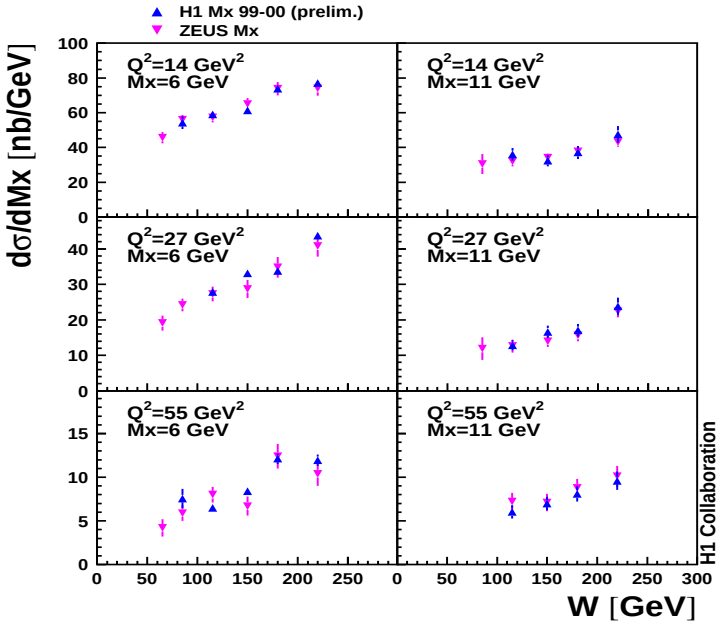

Figure 7: The cross section of the diffractive process $\gamma^* p \to p' X$, differential in the mass of the diffractively produced hadronic system X (M_X), is presented as a function of the center-of-mass energy of the $\gamma^* p$ system W. Measurements at different values of the virtuality Q^2 of the exchanged photon are displayed.

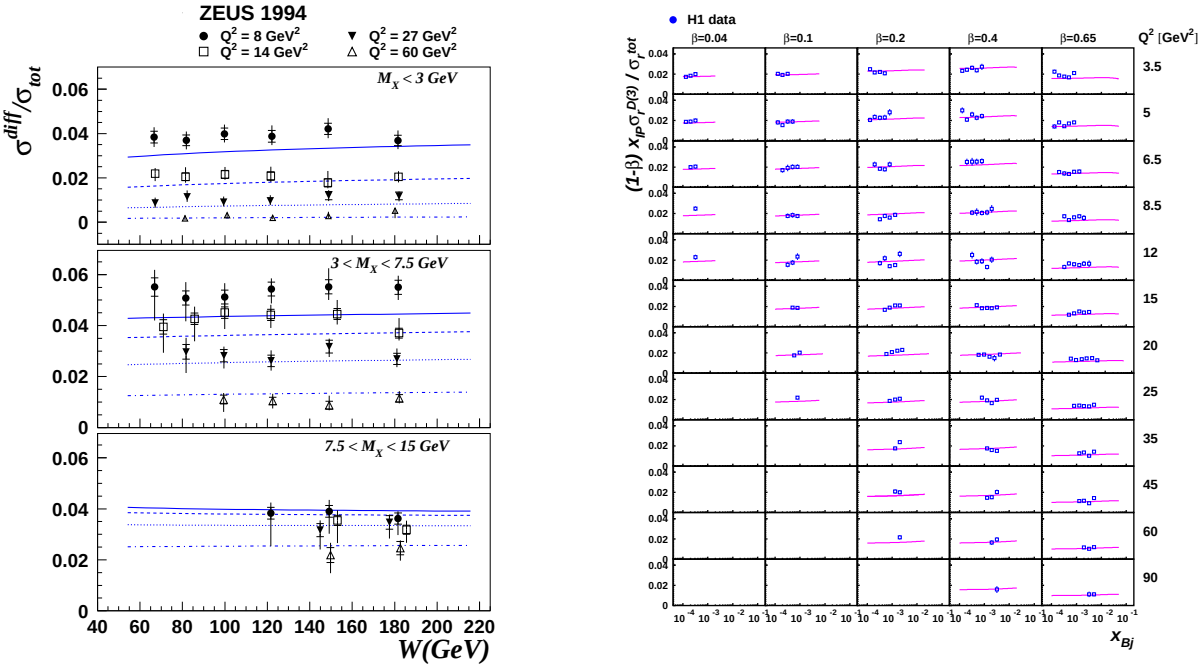

Figure 8: Left: Ratio of the diffractive versus the inclusive cross sections as a function of W for different values of Q^2 and the diffractive mass M_X, derived from early ZEUS data. Right: Ratio of the diffractive versus total cross sections, as a function of x_{Bj}, derived from H1 data for different values of Q^2 and β. A constant ratio of about 0.02 (2%) is observed for each bin of measurements. If we add up the five bins in β (for the bulk of the Q^2 domain), we find immediately the average number of 10%. It gives the fraction of diffractive events on the total DIS sample (see text).

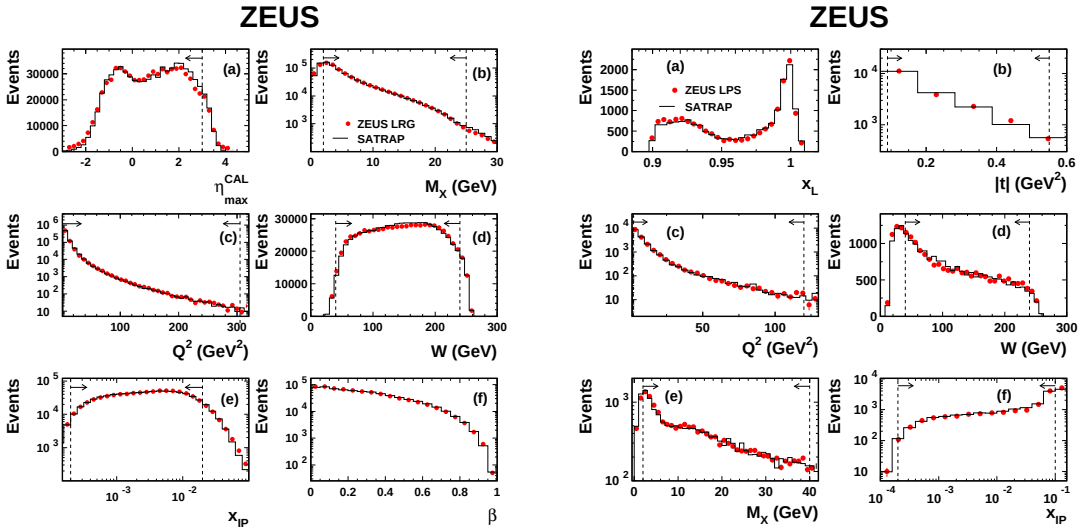

Figure 9: Left: Comparison of the distributions of data (dots) to those obtained with the Monte-Carlo (histograms) for typical variables in the LRG analysis. Right: Comparison of the distributions of data (dots) to those obtained with the Monte-Carlo (histograms) for typical variables in the LPS analysis.

main background in the LRG analysis. Due to a lack of knowledge of this background, it causes a large normalization uncertainty of 10 to 15 % for the cross sections extracted from the LRG analysis.

We can then compare the results obtained by the H1 and ZEUS experiments for diffractive cross sections (in Fig. 11), using the LRG method. A good compatibility of both data sets is observed, after rescaling the ZEUS points by a global factor of 13%. This factor is compatible with the normalization uncertainty described above.

We can also compare the results obtained by the H1 and ZEUS experiments (in Fig. 11), using the tagged proton method (LPS for ZEUS and FPS for H1). In this case, there is no proton dissociation background and the diffractive sample is expected to be clean. It gives a good reference to compare both experiments. A global normalization difference of about 10% can be observed in Fig. 11, which can be studied with more data. It remains compatible with the normalization uncertainty for this tagged proton sample. It is interesting to note that the ZEUS measurements are globally above the H1 data by about 10% for both techniques, tagged proton or LRG.

In Fig. 12, we compare the results using the LRG and the M_X methods, for ZEUS data alone. Both sets are in good agreement, which shows that there is no strong bias between these experimental techniques. The important message at this level is not only the observation of differences as illustrated in Fig. 11, but the opportunity opened with the large statistics provided by the ZEUS measurements. Understanding discrepancies between data sets is part of the experimental challenge of the next months. It certainly needs analysis of new data sets from the HERA experiments. However, already at the present level, much can be done with existing data for the understanding of diffraction at HERA.

4.3 Summary of recent results in one plot

A summary of present measurements using LRG event selection is shown in Fig. 13. The ZEUS LRG data are extracted at the H1 β and $x_{I\!P}$ values, but at different Q^2 values. In order to match the $M_N < 1.6\,\text{GeV}$ range of the H1 data, a global factor of 0.91 ± 0.07, estimated with PYTHIA, is applied to the ZEUS LRG data in place of the correction to an elastic proton cross section. After this procedure, the ZEUS data remain higher than those of H1 by 13% on average, as discussed above. The results of

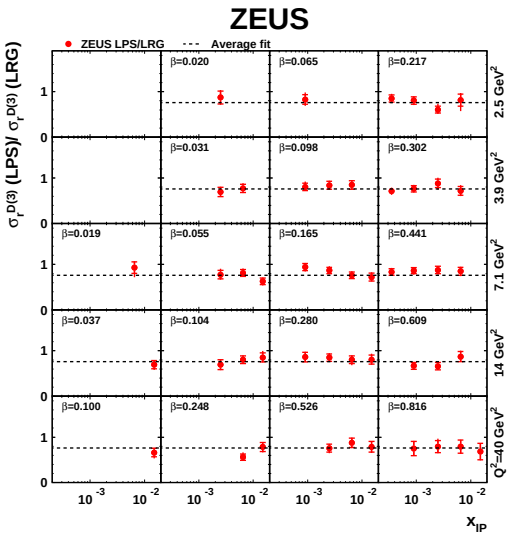

Figure 10: Ratio of the diffractive cross sections, as obtained with the LPS and the LRG experimental techniques. The lines indicate the average value of the ratio, which is about 0.86. It implies that the LRG sample contains about 24% of proton dissociation events, corresponding to processes like $ep \to eXY$, where $M_Y < 2.3$ GeV. This fraction is approximately the same for H1 data (of course in the same M_Y range).

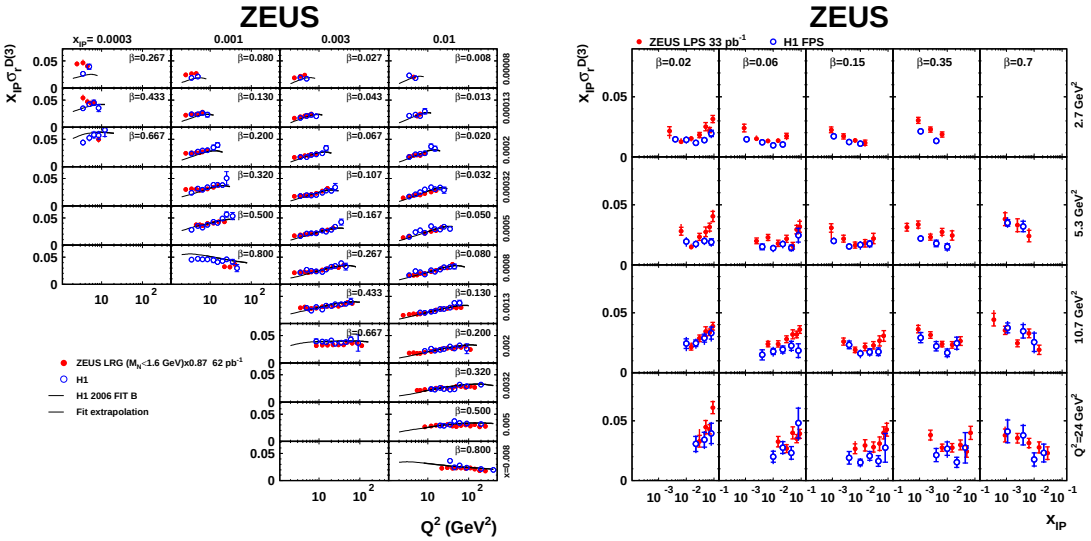

Figure 11: Left: The diffractive cross sections obtained with the LRG method by the H1 and ZEUS experiments. The ZEUS values have been rescaled (down) by a global factor of 13 %. This value is compatible with the normalization uncertainty of this sample. Right: The diffractive cross section obtained with the FPS (or LPS) method by the H1 and ZEUS experiments, where the proton is tagged. The ZEUS measurements are above H1 by a global factor of about 10%.

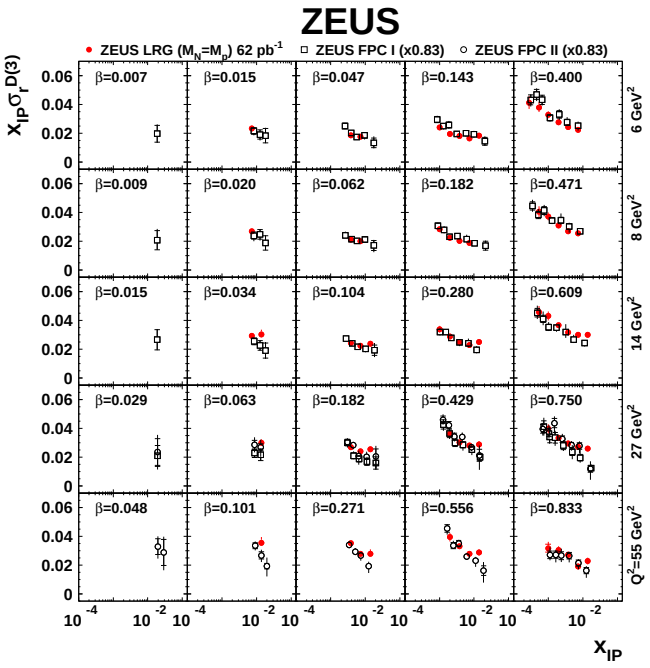

Figure 12: The diffractive cross sections obtained with the LRG method (full dots) compared with the results obtained with the M_X method (open symbols: FPC I and FPC II). All values are converted to $M_Y = M_p$.

the QCD fit to H1 LRG data [2] is also shown (see next section).

5 Diffraction and the resolved Pomeron model

5.1 Theoretical considerations

Several theoretical formulations have been proposed to describe the diffractive exchange. The purpose is to describe the *blob* displayed in Fig. 1 in a quantitative way, leading to a proper description of data shown in Fig. 7.

Among the most popular models, the one based on a point-like structure of the Pomeron assumes that the exchanged object, the Pomeron, is a color-singlet quasi-particle whose structure is probed in the reaction [5, 6]. In this approach, diffractive parton distribution functions (diffractive PDFs) are derived from the diffractive DIS cross sections in the same way as standard PDFs are extracted from DIS measurements. It assumes also that a certain flux of Pomeron is emitted off the proton, depending on the variable $x_{\mathbb{P}}$, the fraction of the longitudinal momentum of the proton lost during the interaction. The partonic structure of the Pomeron is probed during the diffractive exchange [5, 6].

In Fig. 3, we illustrate this factorization property and remind the notations for the kinematic variables used in this paper, as the virtuality Q^2 of the exchanged photon, the center-of-mass energy of the $\gamma^* p$ system W and M_X the mass of the diffractively produced hadronic system X. It follows that the Bjorken variable x_{Bj} verifies $x_{Bj} \simeq Q^2/W^2$ in the low x_{Bj} kinematic domain of the H1 and ZEUS measurements ($x_{Bj} < 0.01$). Also, the Lorentz invariant variable β defined in Fig. 1 is equal to $x_{Bj}/x_{\mathbb{P}}$ and can be interpreted as the fraction of longitudinal momentum of the struck parton in the (resolved) Pomeron.

Because the short-distance cross section $(\gamma^* - q)$ of hard diffractive DIS is identical to inclusive

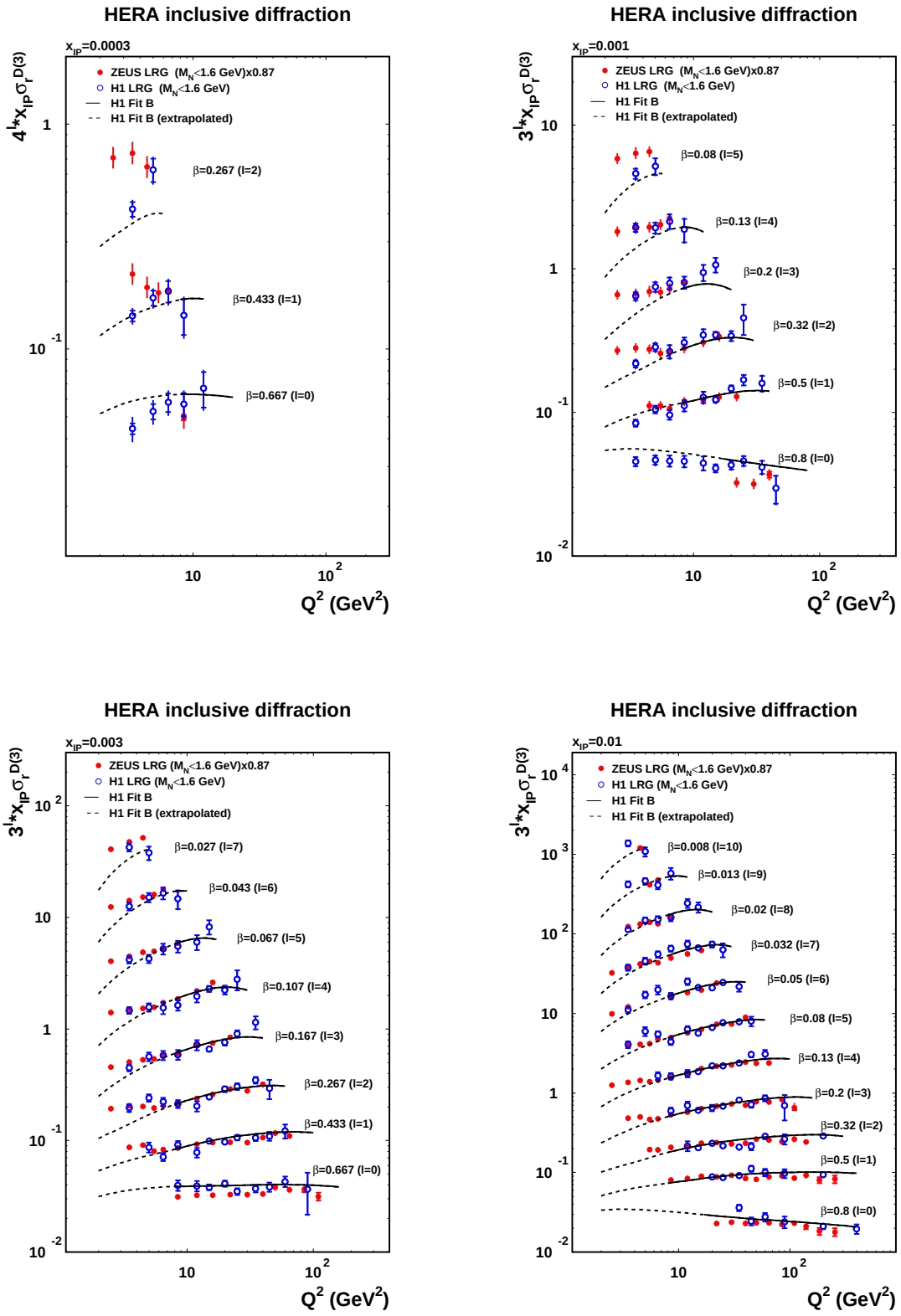

Figure 13: Comparison between the H1 and ZEUS LRG measurements after correcting both data sets to $M_N < 1.6$ GeV and applying a further scale factor of 0.87 (corresponding to the average normalization difference) to the ZEUS data. The measurements are compared with the results of the QCD fit prediction (see text). Further H1 data at $x_{I\!P} = 0.03$ are not shown.

DIS, the evolution of the diffractive parton distributions follows the same equations as ordinary parton distributions. Quantitatively, QCD factorization is expected to hold for F_2^D [5, 6] and it may then be decomposed into diffractive parton distributions, f_i^D, in a way similar to the inclusive F_2,

$$\frac{dF_2^D(x,Q^2,x_{I\!P},t)}{dx_{I\!P}dt} = \sum_i \int_0^{x_{I\!P}} dz \frac{df_i^D(z,\mu,x_{I\!P},t)}{dx_{I\!P}dt} \hat{F}_{2,i}(\frac{x}{z},Q^2,\mu)\,, \tag{3}$$

where $\hat{F}_{2,i}$ is the universal structure function for DIS on parton i, μ is the factorization scale at which f_i^D are probed and z is the fraction of momentum of the proton carried by the parton i.

The QCD evolution equation applies in the same way as for the inclusive case. Fig. 8 is a simple experimental proof of this statement. For a fixed value of $x_{I\!P}$, the evolution in x and Q^2 is equivalent to the evolution in β and Q^2.

If, following Ingelman and Schlein [6], one further assumes the validity of Regge factorization, F_2^D may be decomposed into a universal Pomeron flux and the structure function of the Pomeron,

$$\frac{dF_2^D(x,Q^2,x_{I\!P},t)}{dx_{I\!P}dt} = f_{I\!P/p}(x_{I\!P},t) F_2^{I\!P}(\beta,Q^2)\,, \tag{4}$$

where the normalization of either of the two components is arbitrary. It implies that the $x_{I\!P}$ and t dependence of the diffractive cross section is universal, independent of Q^2 and β, and given by [2, 5, 6]

$$f_{I\!P/p}(x_{I\!P},t) \sim \left(\frac{1}{x_{I\!P}}\right)^{2\alpha_{I\!P}(0)-1} e^{(b_0^D - 2\alpha'_{I\!P}\ln x_{I\!P})t}\,. \tag{5}$$

In this approach, the mechanism for producing LRG is assumed to be present at some scale and the evolution formalism allows to probe the underlying partonic structure. The latter depends on the coupling of quarks and gluons to the Pomeron. It follows that the characteristics of diffraction are entirely contained in the input distributions at a given scale. It is therefore interesting to model these distributions.

5.2 Diffractive parton densities

In Fig. 14 we present the result for diffractive PDFs (quark singlet and gluon densities), obtained using the most recent inclusive diffractive cross sections presented in Ref. [2]. For each experiment (H1 and ZEUS), we include measurements derived from Large Rapidity Gap (LRG) events in the QCD analysis.

We follow the procedure described in Ref. [7], with previous ZEUS data. Note also that in all QCD fits, we let the global relative normalization of the data set as a free parameter (with respect to H1 LRG sample) [7]. The typical uncertainties for the diffractive PDFs in Fig. 14 ranges from 5% to 10% for the singlet density and from 10% to 25% for the gluon distribution, with 25% at large z (which corresponds to large β for quarks) [7]. Similar results have been obtained by the H1 collaboration [2].

In order to analyze in more detail the large z behavior of the gluon distribution $zG(z,Q^2=Q_0^2)$ and give a quantitative estimate of the systematic error related to our parameterizations, we consider the possibility to change the gluon parameterization by a multiplicative factor $(1-z)^\nu$ (see Ref. [7]). If we include this multiplicative factor $(1-z)^\nu$ in the QCD analysis, we derive a value of $\nu = 0.0 \pm 0.5$ (using the most recent data). Thus, we have to consider variations of ν in the interval ± 0.5 in order to allow for the still large uncertainty of the gluon distribution (mainly at large z values). The understanding of the large z behavior is of essential interest for any predictions at the Tevatron or LHC in central dijets production (see below). In particular, a proper determination of the uncertainty in this domain of momentum is necessary and the method we propose in Ref. [7] is a quantitative estimate, that can be propagated easily to other measurements.

Of course, several checks need to be done to analyze the stability of the QCD fits procedure [7]. We present two of them below:

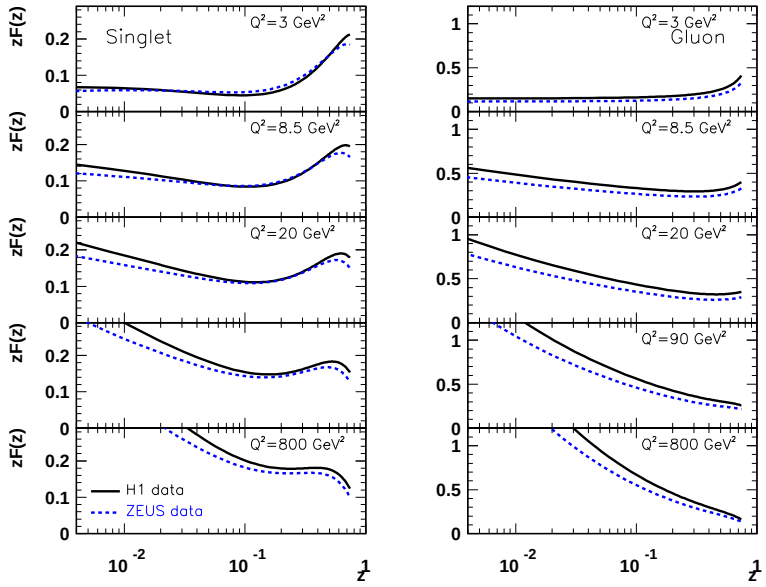

Figure 14: Singlet and gluon distributions of the Pomeron as a function of z, the fractional momentum of the Pomeron carried by the struck parton, derived from QCD fits on H1 and ZEUS inclusive diffractive data (LRG)[2]. The parton densities are normalised to represent $x_{\mathbb{P}}$ times the true parton densities multiplied by the flux factor at $x_{\mathbb{P}} = 0.003$ [7]. A good agreement is observed between both diffractive PDFs, which indicates that the underlying QCD dynamics derived in both experiments is similar.

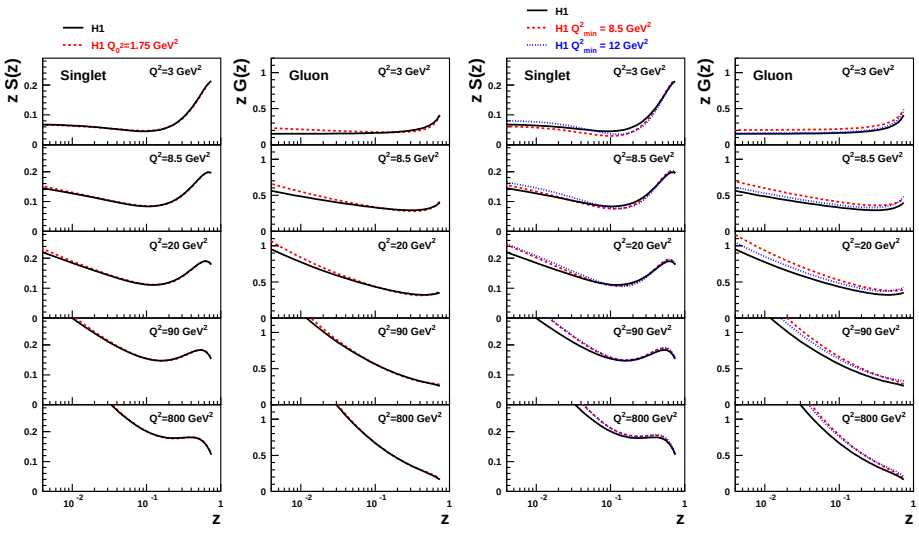

Figure 15: Left: Singlet and gluon distributions of the Pomeron as a function of z, the fractional momentum of the Pomeron carried by the struck parton, derived from QCD fits on H1 data. Results are presented with $Q_0^2 = 3$ GeV^2 (full lines) and $Q_0^2 = 1.75$ GeV^2 (dashed lines). normalization follows the convention explained in Fig. 14. Right: Singlet and gluon distributions of the Pomeron as a function of z derived from QCD fits on H1 data. Results are presented with $Q^2_{min} = 4.5$ GeV^2 (full lines), $Q^2_{min} = 8.5$ GeV^2 (dashed lines) and $Q^2_{min} = 12$ GeV^2 (dotted lines).

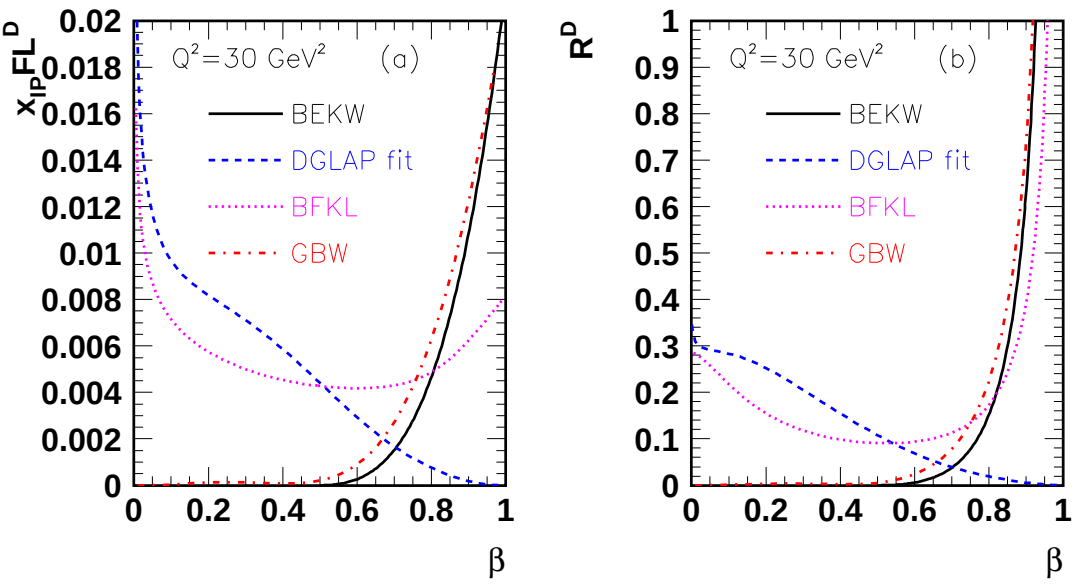

Figure 16: Predictions for $x_{\mathbb{P}}F_L^D$ and $R^D = \frac{F_L^D}{F_2^D - F_L^D}$ as a function of β at $Q^2 = 30$ GeV^2 and $x_{\mathbb{P}} = 10^{-3}$ [7]. The dashed line prediction refers to the diffractive PDFs analysis discussed in this part. Note that the longitudinal structure function F_L^D is directly related to the the reduced diffractive cross section: $\sigma_r^{D(3)} = F_2^{D(3)} - \frac{y^2}{1+(1-y)^2} F_L^{D(3)}$. Other curves represent dipole model calculations (see next sections).

- We have checked the dependence of the diffractive PDFs on variations of the starting scale Q_0^2 in Fig. 15 (left). Very small changes are observed while changing the starting scale form 3 to 1.75 GeV^2.

- We have checked the fit stability by changing the cut on Q^2_{min}, the lowest value of Q^2 of data to be included in the fit. The results are given in Fig. 15 (right), where we show the results of the fits after applying a cut on Q^2_{min} of 4.5, 8.5 and 12 GeV^2. Differences are noticeable at small β but well within the fit uncertainties. No systematic behavior is observed within Q^2_{min} variations.

Then, an important conclusion is the prediction for the longitudinal diffractive structure function. In Fig. 16 [7] and 17 [8], we display this function with respect to its dependence in β (Fig. 16 (a)) and the ratio R of the longitudinal to the transverse components of the diffractive structure function (Fig. 16 (b)). A comment is in order about the large β behavior. $x_{\mathbb{P}}F_L^D$ is essentially zero at large β from the pure QCD fits analysis. In fact, as illustrated in Fig. 16 and 17, a non-zero contribution to the longitudinal structure function at large β corresponds to a twist–4, and is simply incorporated in a dipole model formulation of diffraction (see next sections). Here, we give the qualitative feature of this effect on the predictions for $x_{\mathbb{P}}F_L^D$. There is a significant difference between predictions with or without this twist–4 component in the region of large β. However, the difference is negligible at low and medium β, where the measurements are possible. Indeed, a first measurements has been realized by the H1 collaboration [4], which is displayed in Fig. 18. It fits perfectly with the QCD fit prediction, as well as with the dipole prediction in the kinematic range accessible experimentally ($\beta < 0.2$). This Fig. 18 gives also directly the ratio of F_L^D versus F_2^D.

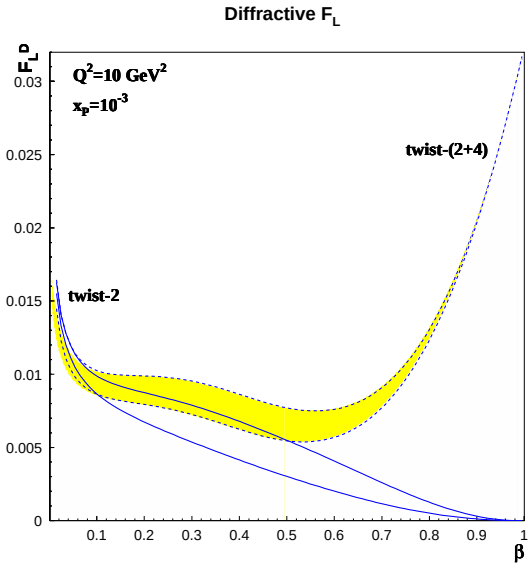

Figure 17: Predictions for F_L^D for $x_{I\!P} = 10^{-3}$ and $Q^2 = 10$ GeV^2 from fits with twist–4, dominant only at large β, to the HERA data. The solid lines show predictions from pure (twist–2) QCD fits [8].

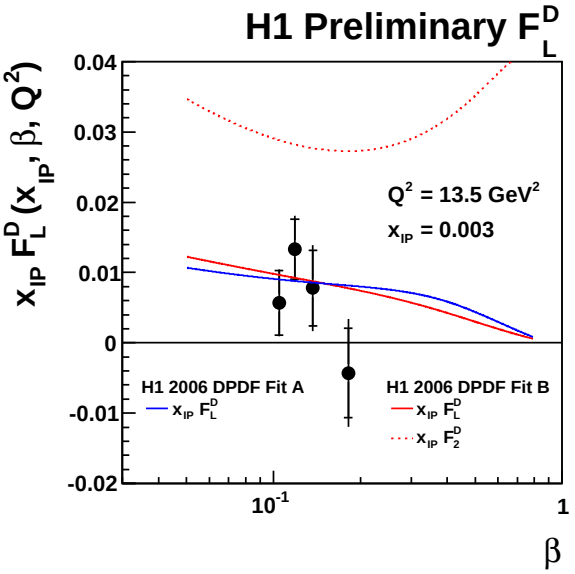

Figure 18: Measurements of the diffractive longitudinal structure function F_L^D multiplied by $x_{I\!P}$. The data are compared to QCD fits predictions (see text). Also shown for comparison is the value of F_2^D as a dashed line.

6 Diffraction at the Tevatron and prospects for LHC

6.1 Basics of diffraction at the Tevatron

Once the gluon and quark densities in the Pomeron are known, it is easy to make predictions for the Tevatron (or the LHC) if one assumes that the same mechanism is the origin of diffraction in both cases. We assume the same structure of the Pomeron at HERA and the Tevatron and we compute as an example the jet production in single diffraction or double Pomeron exchange using the parton densities in the Pomeron measured at HERA. The interesting point is to see if this simple argument works or not, or if the factorization property between HERA and the Tevatron — using the same parton distribution functions — holds or not [9, 10, 11]. In other words, we need to know if it is possible to use the parton distributions in the Pomeron obtained at HERA to make predictions at the Tevatron, and also further constrain the parton distribution functions in the Pomeron since the reach in the diffractive kinematical plane at the Tevatron and HERA is different.

Theoretically, factorization is not expected to hold between the Tevatron and HERA [5] due to additional pp or $p\bar{p}$ interactions. For instance, some soft gluon exchanges between protons can occur at a longer time scale than the hard interaction and destroy the rapidity gap or the proton does not remain intact after interaction. The factorization break-up is confirmed by comparing the percentage of diffractive events at HERA and the Tevatron (10% at HERA and about 1% of single diffractive events at the Tevatron) showing already that factorization does not hold. This introduces the concept of gap survival probability, the probability that there is no soft additional interaction or that the event remains diffractive.

The first experimental test of factorization concerns CDF data only. Fig. 19 shows the percentage of diffractive events as a function of x for different ξ bins and shows the same x-dependence within systematic and statistical uncertainties in all ξ bins supporting the fact that CDF data are consistent with factorization [9]. The CDF collaboration also studied the x dependence for different Q^2 bins which leads to the same conclusions.

A second step is to check whether factorization holds or not between Tevatron and HERA data. The measurement of the diffractive structure function is possible directly at the Tevatron. The CDF collaboration measured the ratio of dijet events in single diffractive and non diffractive events, which is directly proportional to the ratio of the diffractive to the standard proton structure functions, where

$$R(x) = \frac{Rate_{jj}^{SD}(x)}{Rate_{jj}^{ND}(x)} \sim \frac{F_{jj}^{SD}(x)}{F_{jj}^{ND}(x)}. \tag{6}$$

The comparison between the CDF measurement (black points, with systematics errors) and the expectation from the diffractive QCD fits on HERA data in full line is shown in Fig. 20 [10].

We notice a discrepancy of a factor 8 to 10 between the data and the predictions from the QCD fit, showing that factorization does not hold. However, the difference is compatible within systematic and statistical uncertainties with a constant on a large part of the kinematical plane in β, showing that the survival probability does not seem to be β-dependent within experimental uncertainties.

It would be interesting to make these studies again in a wider kinematical domain both at the Tevatron and at the LHC. The understanding of the survival probability and its dependence on the kinematic variables is important to make precise predictions on inclusive diffraction at the LHC.

6.2 Discussion on the factorization breaking HERA/Tevatron

In fact, from a fundamental point of view, it is natural that diffractive hard-scattering factorization does not apply to hadron-hadron collisions. Attempts to establish corresponding factorization theorems fail, because of interactions between spectator partons of the colliding hadrons. The contribution of these

interactions to the cross section does not decrease with the hard scale. Since they are not associated with the hard-scattering subprocess, we no longer have factorization into a parton-level cross section and the parton densities of one of the colliding hadrons. These interactions are generally soft, and we have at present to rely on phenomenological models to quantify their effects.

The yield of diffractive events in hadron-hadron collisions is then lowered precisely because of these soft interactions between spectator partons (often referred to as re-interactions or multiple scatterings). They can produce additional final-state particles which fill the would-be rapidity gap (hence the often-used term rapidity gap survival). When such additional particles are produced, a very fast proton can no longer appear in the final state because of energy conservation.

Diffractive factorization breaking is thus intimately related to multiple scattering in hadron-hadron collisions. We can also remark simply that the collision partners, in hadron-hadron reactions, are both composite systems of large transverse size, and it is not too surprising that multiple interactions between their constituents can be substantial.

In contrast, the virtual photon in $\gamma^* p$ collisions has small transverse size, which disfavors multiple interactions and enables diffractive factorization to hold. According to our discussion, we may expect that for decreasing virtuality Q^2 the photon behaves more and more like a hadron, and diffractive factorization may again be broken.

6.3 Restoring factorization at the Tevatron

The other interesting measurement which can be also performed at the Tevatron is the test of factorization between single diffraction and double Pomeron exchange. The results from the CDF collaboration are shown in Fig. 21 [10]. The left plot shows the definition of the two ratios while the right figure shows the comparison between the ratio of double Pomeron exchange to single diffraction and the QCD predictions using HERA data in full line.

Whereas factorization was not true for the ratio of single diffraction to non diffractive events, factorization holds for the ratio of double Pomeron exchange to single diffraction. In other words, the price to pay for one gap is the same as the price to pay for two gaps. The survival probability, i.e. the probability not to emit an additional soft gluon after the hard interaction needs to be applied only once to require the existence of a diffractive event, but should not be applied again for double Pomeron exchange.

To summarize, factorization does not hold between HERA and Tevatron as expected because of the long term additional soft exchanges with respect to the the hard interaction. However, experimentally, factorization holds with CDF data themselves and also between single diffraction and double Pomeron exchange which means that the soft exchanges do not depend on the hard scattering, which is somehow natural.

6.4 Interest of exclusive events

Once established some basics of the diffraction at the Tevatron, a fundamental topic concerns the analysis of exclusive events. A schematic view of non diffractive, inclusive double Pomeron exchange, exclusive diffractive events at the Tevatron or the LHC is displayed in Fig. 22. The upper left plot shows the standard non diffractive events where the Higgs boson, the dijet or diphotons are produced directly by a coupling to the proton and shows proton remnants. The bottom plot displays the standard diffractive double Pomeron exchange where the protons remain intact after interaction and the total available energy is used to produce the heavy object (Higgs boson, dijets, diphotons...) and the Pomeron remnants. We have so far only discussed this kind of events and their diffractive production using the parton densities measured at HERA.

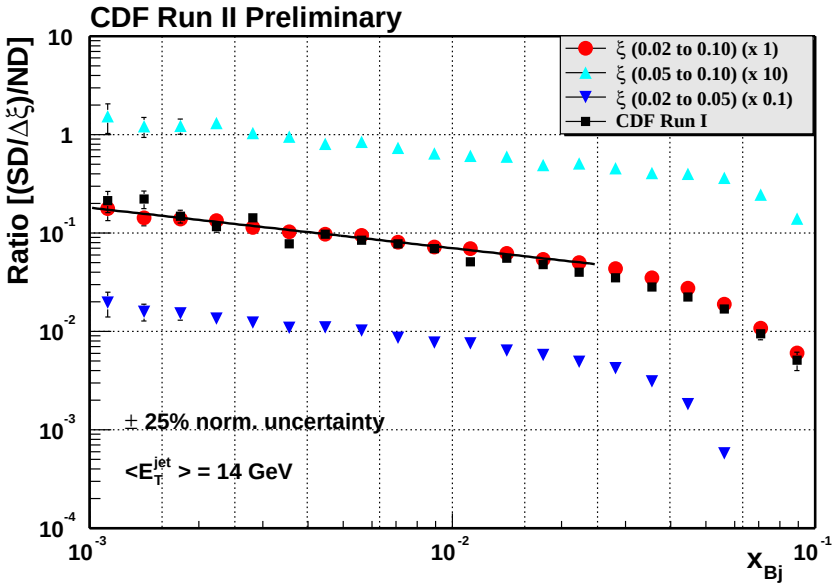

Figure 19: Test of factorization within CDF data alone. The percentage of diffractive events is presented as a function of x for different ξ bins. The same x-dependence is observed within systematic and statistical uncertainties in all ξ bins, supporting the fact that CDF data are consistent with factorization [9].

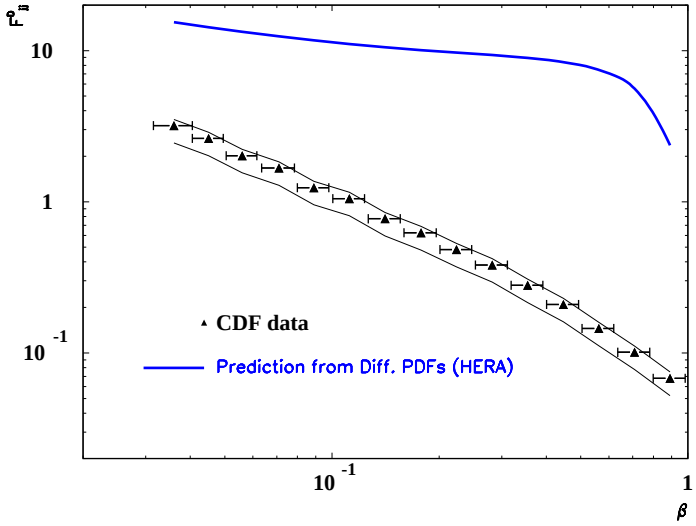

Figure 20: Comparison between the CDF measurements ($Q^2 = 75$ GeV^2, $0.035 < \xi < 0.095$ and $|t| < 1$ GeV^2) of diffractive structure function (black points) with the expectation of the HERA (using first H1 diffractive data) diffractive PDFs [7]. The large discrepancy both in shape and normalization between HERA predictions and CDF data illustrates the breaking of factorization at the Tevatron. Using the most recent measurements in QCD fits (and diffractive PDFs extraction) does not change this conclusion.

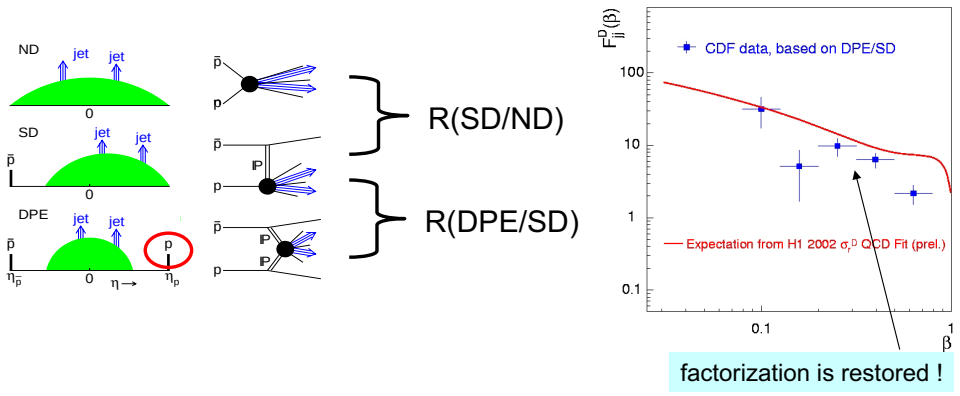

Figure 21: Restoration of factorization for the ratio of double Pomeron exchange to single diffractive events (CDF Coll.). Whereas factorization was not true for the ratio of single diffraction to non diffractive events, factorization holds for the ratio of double Pomeron exchange to single diffraction. The price to pay for one gap is the same as the price to pay for two gaps.

There may be a third class of processes displayed in the upper right figure, namely the exclusive diffractive production. In this kind of events, the full energy is used to produce the heavy object (Higgs boson, dijets, diphotons...) and no energy is lost in Pomeron remnants. There is an important kinematical consequence. The mass of the produced object can be computed using roman pot detectors and tagged protons

$$M = \sqrt{\xi_1 \xi_2 S}. \tag{7}$$

We see immediately the advantage of these processes. We can benefit from the good roman pot resolution on ξ_1 and ξ_2 to get a good resolution on mass. It is then possible to measure the mass and the kinematical properties of the produced object and use this information to increase the signal over background ratio by reducing the mass window of measurement. It is thus important to know if this kind of events exist or not.

In the following, we give some details of the search for exclusive events in the different channels which are performed by the CDF and D0 collaborations at the Tevatron. Prospects for the LHC are then outlined.

6.5 Search for exclusive events in χ_c production

For example, one way to look for exclusive events at the Tevatron is to search for the diffractive exclusive production of light particles like the χ mesons. This would give rise to high enough cross sections – contrary to the diffractive exclusive production of heavy mass objects such as Higgs bosons — to check the dynamical mechanisms and the existence of exclusive events. Exclusive production of χ_c has been studied by the CDF collaboration [11] with an upper limit for the cross section of $\sigma_{exc}(p\bar{p} \to p + J/\psi + \gamma + \bar{p}) \sim 49 \pm 18(stat) \pm 39(sys)$ pb, where the χ_c decays into J/Ψ and γ, the J/Ψ decaying itself into two muons. The experimental signature is thus two muons in the final state and an isolated photon, which is a very clear signal.

Unfortunately, the cosmics contamination is difficult to compute and this is why the CDF collaboration only quotes an upper limit on the χ_c production cross section. To know if the production is really exclusive, it is important to study the tail of inclusive diffraction which is a direct contamination of the

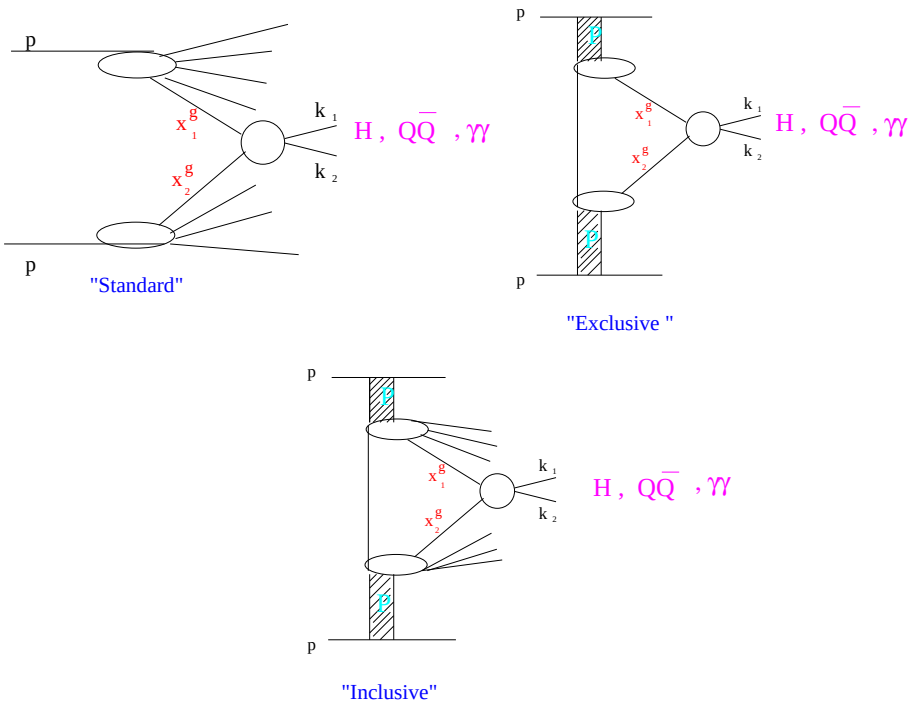

Figure 22: Scheme of non diffractive, inclusive double Pomeron exchange, exclusive diffractive events at the Tevatron or the LHC.

exclusive signal. The tail of inclusive diffraction corresponds to events which show very little energy in the forward direction, or in other words where the Pomeron remnants carry very little energy. This is why these events can be called quasi-exclusive.

In Ref. [12], it is shown that the contamination of inclusive events into the signal region depends strongly on the assumptions on the gluon distribution in the Pomeron at high β, which is poorly known as we mentioned in a previous section. Therefore, this channel is not conclusive concerning the existence of exclusive events. In the same spirit, the CDF collaboration also looked for the exclusive production of dilepton and diphoton [13].

6.6 Search for exclusive events using the dijet mass fraction

Another very important aspect of diffraction at the Tevatron is related to the diffractive production of dijet events in double Pomeron exchange (see Fig. 22). The CDF collaboration measured the so-called dijet mass fraction in dijet events — the ratio of the mass carried by the two jets produced in the event divided by the total diffractive mass — when the antiproton is tagged in the roman pot detectors and when there is a rapidity gap on the proton side to ensure that the event corresponds to a double Pomeron exchange.

The CDF collaboration has measured this quantity for different jet p_T cuts [14]. In Fig. 23, we compare this measurement to the expectation coming from the structure of the Pomeron coming from HERA. For this sake, one takes the gluon and quark densities in the Pomeron measured at HERA as described in Ref. [7] and the factorization breaking between HERA and the Tevatron is assumed to come only through the gap survival probability (0.1 at the Tevatron). The comparison between the CDF data for a jet p_T cut of 10 GeV as an example and the predictions from inclusive diffraction is given in Fig. 23, left.

We also display in the same figure the effects of changing the gluon density at high β (by changing the value of the ν parameter) and we note that inclusive diffraction is not able to describe the CDF

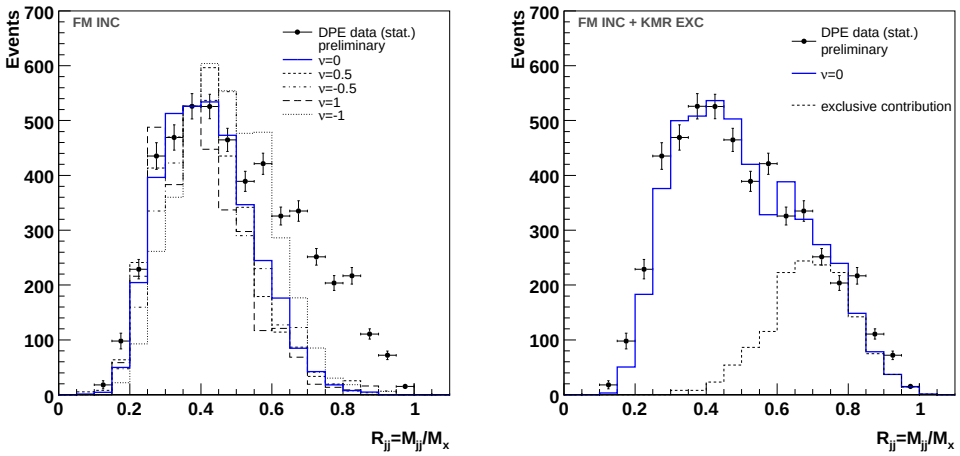

Figure 23: Left: Dijet mass fraction measured by the CDF collaboration compared to the prediction from inclusive diffraction based on the parton densities in the Pomeron measured at HERA. The gluon density in the Pomeron at high β was modified by varying the parameter ν. Right: Dijet mass fraction measured by the CDF collaboration compared to the prediction adding the contributions from inclusive and exclusive diffraction.

data at high dijet mass fraction, even after increasing the gluon density in the Pomeron at high β (multiplying it by $1/(1-\beta)$), where exclusive events are expected to appear [7, 15].

The conclusion remains unchanged when jets with $p_T > 25$ GeV are considered [7, 15]. Adding exclusive events to the distribution of the dijet mass fraction leads to a good description of data [7, 15] as shown in Fig. 23, right, where we superimpose the predictions from inclusive and exclusive diffraction.

This study does not prove explicitly that exclusive events exist but shows that some additional component with respect to inclusive diffraction is needed to explain CDF data. Adding exclusive diffraction allows to explain the CDF measurement. To be sure of the existence of exclusive events, the observation will have to be done in different channels and the different cross sections to be compared with theoretical expectations [2].

6.7 Prospects for LHC

The search for exclusive events at the LHC can be performed in the same channels as the ones used at the Tevatron. Let us recall that a strong motivation for this idea is that heavy objects, like Higgs boson, could be produced in double pomeron exchange at the LHC [16]. In addition, some other possibilities benefiting from the high luminosity of the LHC appear. One of the cleanest ways to show the existence of exclusive events would be to measure the dilepton and diphoton cross section ratios as a function of the dilepton/diphoton mass [16]. If exclusive events exist, this distribution should show a bump towards high values of the dilepton/diphoton mass since it is possible to produce exclusively diphotons but not dileptons at leading order as we mentioned in the previous paragraph.

The motivation to install forward detectors at in ATLAS and CMS is then quite clear. In addition, it extends nicely the project of measuring the total cross sections in ATLAS and TOTEM by measuring hard diffraction at high luminosity at the LHC. Of course, this is a very challenging technical project.

[2] In Ref. [15], the CDF data were also compared to the soft color interaction models. While the need for exclusive events is less obvious for this model, especially at high jet p_T, the jet rapidity distribution measured by the CDF collaboration is badly reproduced. This is due to the fact that, in the SCI model, there is a large difference between requesting an intact proton in the final state and a rapidity gap.

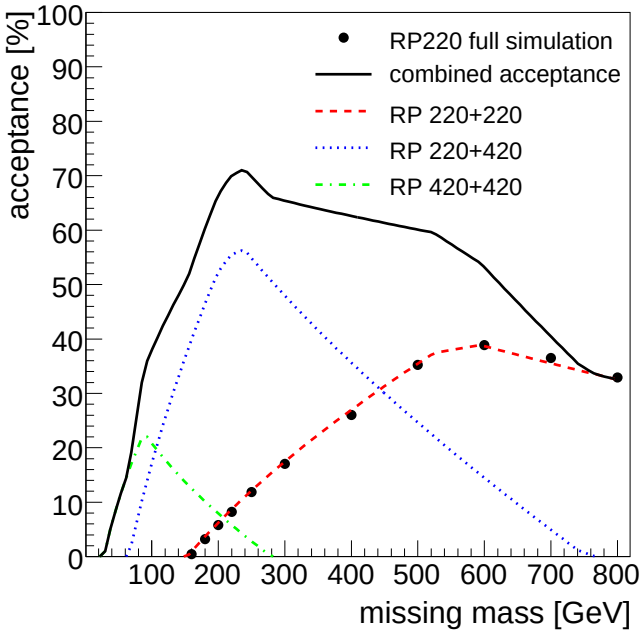

Figure 24: Roman pot detector acceptance as a function of missing mass assuming a 10σ operating positions, a dead edge for the detector of 50 μm and a thin window of 200 μm.

Without entering into details, a few technical issues can be discussed simply. Two locations for the forward detectors are considered at 220 and 420m respectively to ensure a good coverage in ξ or in mass of the diffractively produced object [16]. Installing forward detectors at 420m is quite challenging since the detectors will be located in the cold region of the LHC and the cryostat has to be modified to accommodate the detectors. In addition, the space available is quite small and some special mechanism called movable beam pipe are used to move the detectors close to the beam when the beam is stable enough. The situation at 220m is easier since it is located in the warm region of the LHC and both roman pot and movable beam pipe technics can be used. The AFP (ATLAS Forward Physics) project is under discussion in the ATLAS collaboration and includes both 220 and 420m detectors on both sides of the main ATLAS detector [16].

To conclude on the diffraction at the LHC, the missing mass acceptance is given in Fig. 24. The missing mass acceptance using only the 220m pots starts at 135 GeV, but increases slowly as a function of missing mass. It is clear that one needs both detectors at 220 and 420m to obtain a good acceptance on a wide range of masses since most events are asymmetric (one tag at 220m and another one at 420m). The precision on mass reconstruction using either two tags at 220m or one tag at 220m and another one at 420m is of the order of 2-4 % on the full mass range, whereas it goes down to 1% for symmetric 420m tags [16].

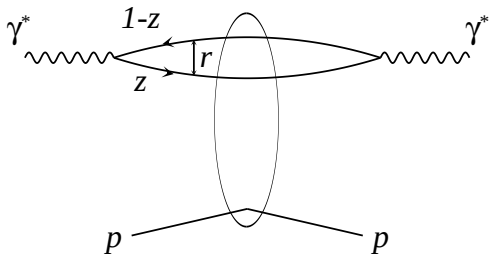

Figure 25: Picture for the total cross section ($\gamma^* p \to \gamma^* p$) in the dipole model.

7 Diffraction and the dipole model

7.1 Simple elements of theory

The physical picture of hard diffraction at HERA is interesting in the proton rest frame and reminiscent of the aligned jet model. In the proton rest frame, at small x_{Bj}, the virtual photon splits into a $q\bar{q}$ pair long before it hits the proton [17, 18, 19, 20] (see Fig. 25). The $q\bar{q}$ wave-function of the virtual photon suppresses configurations in which one of the quarks carries almost all momentum. In fact, these configurations are the ones that give rise to a large diffractive cross section, just because the wave-function suppression is compensated by the large cross section for the scattering of a $q\bar{q}$ pair of hadronic transverse size off the proton. The harder of the two quarks is essentially a spectator to diffractive scattering.

The scattering of the softer quark off the proton is non-perturbative and cannot be described by exchange of a finite number of gluons. Hence there is an unsuppressed probability that the softer quark leaves the proton intact. This explains simply the idea behind the leading twist nature of hard diffraction. The details of the scattering of the softer quark off the proton are encoded in the diffractive quark distribution. In a similar way, the $q\bar{q}g$ configuration in the virtual photon, in which the $q\bar{q}$ pair carries almost all momentum, gives rise to the diffractive gluon distribution.

Also, in the simplest case, the colorless exchange responsible for the rapidity gap is modeled by the exchange of two gluons (projected onto the color singlet state) coupled to the proton with some form factor or to a heavy onium which serves as a model of the proton [18, 19, 20]. We focus the following discussion on dipole approaches of diffractive interactions, that follow exactly these ideas.

Then, we can model the reaction in three different phases, as displayed in Fig. 26 -top-:

(1) the transition of the virtual photon to the $q\bar{q}$ pair (the color dipole) at a large distance $l \sim \frac{1}{m_N x}$ of about 10-100 fm for HERA kinematics, upstream the target,

(2) the interaction of the color dipole with the target nucleon, and

(3) the projection of the scattered $q\bar{q}$ onto the diffractive system X.

7.2 Confrontation of HERA measurements to the dipole approach

Following the arguments above, the inclusive diffractive cross section is described with three main contributions in dipole approaches. The first one describes the diffractive production of a $q\bar{q}$ pair from a transversely polarized photon, the second one the production of a diffractive $q\bar{q}g$ system, and the third one the production of a $q\bar{q}$ component from a longitudinally polarized photon (see Fig. 26 -top-). In Fig. 26 -bottom-, we show that this approach, also called two-gluon exchange model gives a good description of the diffractive cross section measurements [18, 19, 20].

One of the great advantage of the dipole model is that it provides a natural explanation of the rapidity gap formation. Another great advantage of the dipole formulation is that it provides a natural

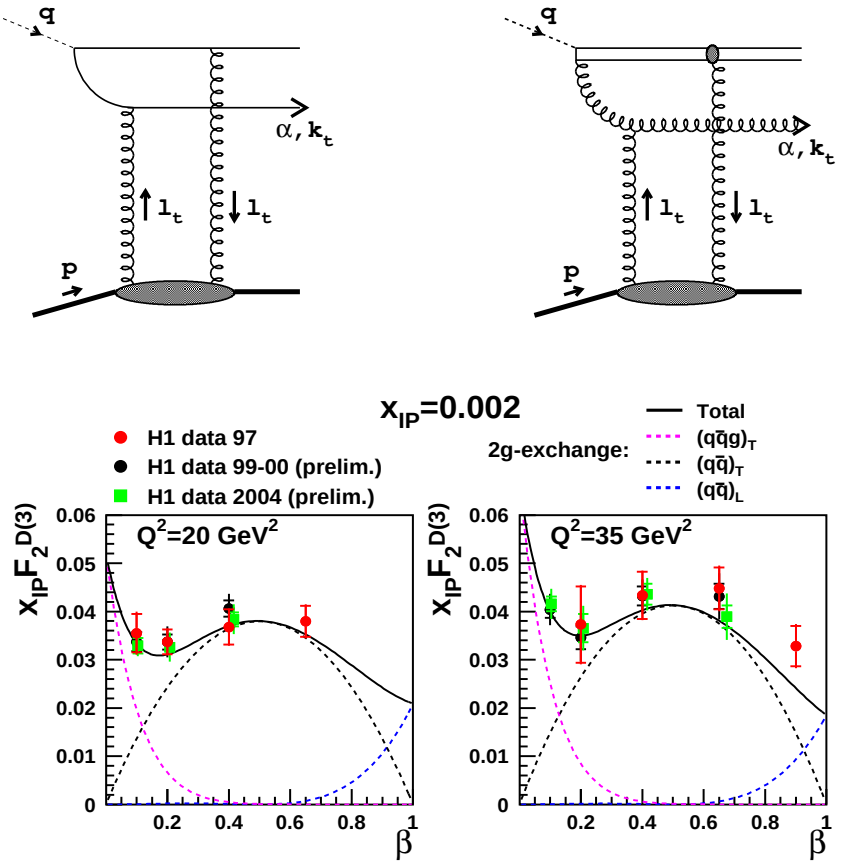

Figure 26: Top: The $q\bar{q}$ and $q\bar{q}g$ components of the diffractive system. Bottom: The diffractive structure function $x_{I\!P} F_2^{D(3)}$ is presented as a function of β for two values of Q^2. The different components of the two-gluon exchange model are displayed (see text). They add up to give a good description of the data. The structure function $x_{I\!P} F_2^{D(3)}$ is obtained directly from the measured diffractive cross section using the relation : $\frac{d^3\sigma^{ep\to eXp}}{dx_{I\!P}\ dx\ dQ^2} \simeq \frac{4\pi\alpha^2_{em}}{xQ^4}(1-y+\frac{y^2}{2})F_2^{D(3)}(x_{I\!P},x,Q^2)$, where y represents the inelasticity of the reaction.

explanation of the experimental observation that $\sigma^{diff}/\sigma^{tot} \simeq const$ as a function of energy W (see Fig. 8) [20]. Indeed, the dipole picture is valid in the frame in which the $q\bar{q}$ pair (dipole) carries most of the available rapidity $Y \sim \ln(1/x)$ of the system. The gluon radiation from the parent dipole can then be interpreted (in the large N_c limit) as a collection of dipoles of different transverse sizes which interact with the proton. If the proton stays intact, diffractive events with large rapidity gap are formed. In such case, the diffractive system is given by the color dipoles and the diffractive exchange can be modeled by color singlet gluons exchange (two-gluon exchange) between the dipole and the proton (see Fig. 25 and 26-top-). When only the parent $q\bar{q}$ dipole forms a diffractive system, the diffractive cross section at $t = 0$ reads

$$\frac{d\,\sigma^{diff}}{dt}_{|\,t=0} = \frac{1}{16\,\pi}\int d^2r\,dz\,|\Psi^\gamma(r,z,Q^2)|^2\;\hat{\sigma}^2(x,r), \tag{8}$$

where Ψ^γ is the well known light-cone wave function of the virtual photon, r is the dipole transverse size and z is a fraction of the photon momentum carried by the quark. Applying the $q\bar{q}$ dipole picture

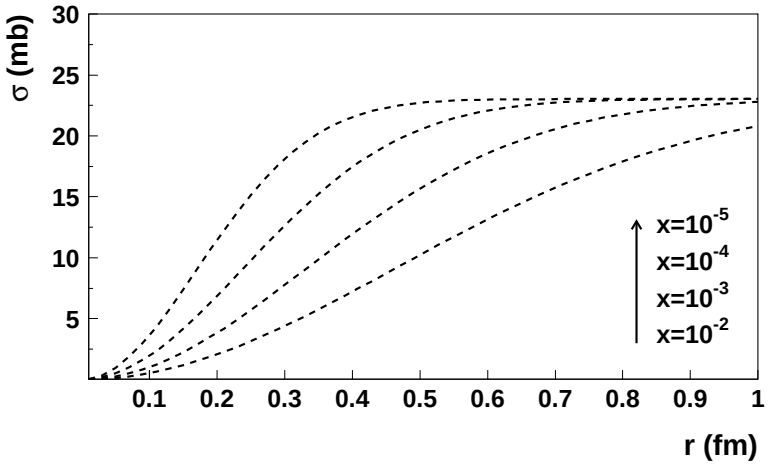

Figure 27: The dipole cross section $\sigma_{q\bar{q}}$ in the saturation model as a function of dipole size r for different x (see text).

to the total inclusive cross section, σ^{tot}, the following relation holds in the small-x limit

$$\sigma^{tot} \;=\; \int d^2r\, dz\, |\Psi^{\gamma}(r,z,Q^2)|^2\; \hat{\sigma}(x,r), \tag{9}$$

with the same dipole cross $\hat{\sigma}(x,r)$ as in Eq. (8). This Eq. (9) is pictured in Fig. 25.

7.3 Saturation, concepts and practice

In Eq. 8 and 9, the parameterization of $\hat{\sigma}(x,r)$ must be realized with caution [20, 19]. There are several features to consider. First, the density of gluons at given x increases with increasing Q^2, as described in perturbative QCD. According to QCD evolution it also increases at given Q^2 when x becomes smaller, so that the gluons become more and more densely packed. At some point, they start to overlap and thus re-interact and screen each other. Then, we enter a regime where the density of partons saturates and where the linear QCD evolution equations cease to be valid. To quantify these effects, a saturation scale Q_s^2 can be introduced, which also depends on x, such that for $Q^2 \sim Q_s^2(x)$ these effects of saturation become important.

In practice, essential features of the saturation phenomenon are verified in the following parameterization for the dipole cross section first proposed in Ref. [20]

$$\hat{\sigma}(x,r) \;=\; \sigma_0 \left\{1 - \exp(-r^2 Q_s^2(x))\right\}, \tag{10}$$

where $Q_s(x) \;=\; Q_0\,(x/x_0)^{-\lambda}$ is the saturation scale. In Fig. 27, we display the dipole cross section dependence of Eq. (10) as a function of r at given x in this model. At small dipole size $r \sim 1/Q$ (large Q^2), the cross section rises following the relation $\hat{\sigma}(x,r) \propto r^2 x g(x)$. At some value $R_s(x)$ of r, the dipole cross section is so large that this relation ceases to be valid, and $\hat{\sigma}(x,r)$ starts to deviate from the quadratic behavior in r. Therefore, $R_s(x) = 1/Q_s(x)$ represents a typical saturation scale. As r continues to increase, $\hat{\sigma}(x,r)$ eventually saturates at a value typical of a meson-proton cross section. For smaller values of x, the initial growth of $\sigma_{q\bar{q}}$ with r is stronger because the gluon distribution is larger. The target is thus more opaque and saturation sets in at lower r.

Parameters of the dipole cross section of Eq. (10) are obtained from the analysis of inclusive data, and then can be used to predict diffractive cross section in DIS, and even more processes as we discuss in the next section. An important aspect of Eq. (10), in which r and x are combined into one dimensionless

variable $rQ_s(x)$, is what is called geometric scaling, a new scaling property in inclusive DIS at small x. In Ref. [20], it has been shown to be valid for the total cross section (see Fig. 7.3).

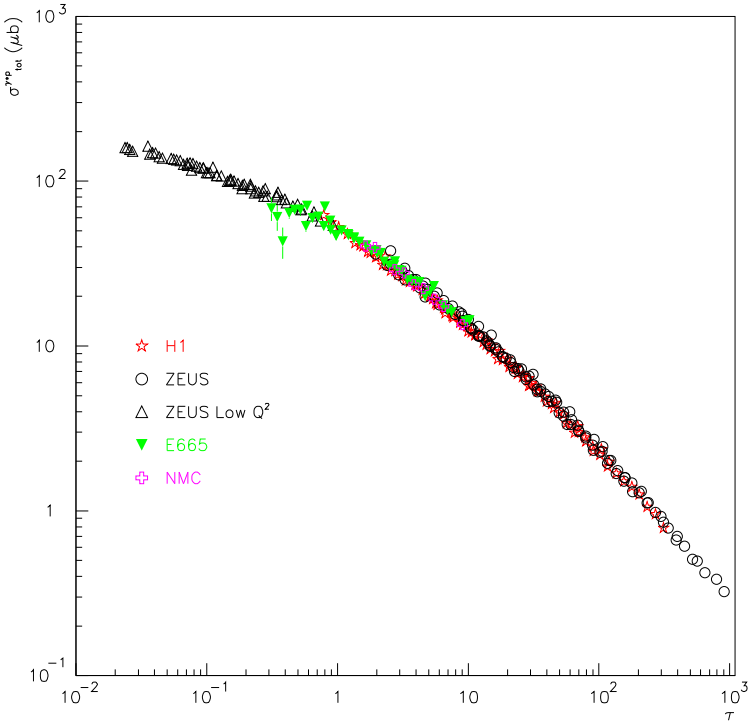

Figure 28: The total cross section $\sigma_{tot}^{\gamma^* p\to X}$ as a function of $\tau = Q^2/Q_s^2$ for $x < 0.01$. The saturation regime is reached when $Q_s \sim Q$. For inclusive events in deep inelastic scattering, this feature manifests itself (as displayed) via the geometric scaling property: instead of being a function of Q^2/Q_0^2 and x separately, the total cross-section is only a function of $\tau = Q^2/Q_s^2(x)$, up to large values of τ.

It happens that diffraction in DIS is an ideal process to study parton saturation since this process is especially sensitive to the large dipole contribution, $r > 1/Q_s(x)$ [20]. Unlike inclusive DIS, the region below, $r < 1/Q_s(x)$, is suppressed by an additional power of $1/Q^2$. This makes obviously diffractive interactions very important for tracting saturation effects. As already mentioned, the dipole cross section with saturation (see Eq. (10)) leads in a natural way to the constant ratio (up to logarithms)

$$\frac{\sigma^{diff}}{\sigma^{tot}} \sim \frac{1}{\ln(Q^2/Q_s^2(x))}\,. \tag{11}$$

We can present very simply the main elements of the calculation that bring this result. Indeed, the photon wave function, in Eq. (8), favors small dipoles (small $r \sim 1/Q$), which gives

$$\frac{d\,\sigma^{diff}}{dt}_{|\,t=0} = \frac{1}{16\,\pi}\int d^2r\,dz\,|\Psi^\gamma(r,z,Q^2)|^2\;\hat\sigma^2(x,r) \sim \frac{1}{Q^2}\int_{1/Q^2}^{\infty}\frac{dr^2}{r^4}\hat\sigma^2(x,r).$$

On the other hand, the dipole cross section favors relatively large dipoles, with $\hat\sigma(x,r) \sim r^2$. However, as discussed above in the building of Eq. (10), at sufficiently high energy, saturation cuts off the large dipoles already on the semi-hard scale $1/Q_s$. This leads to

$$\frac{d\,\sigma^{diff}}{dt}_{|\,t=0} \sim \frac{1}{Q^2}\int_{1/Q^2}^{1/Q_s^2}\frac{dr^2}{r^4}(r^2Q_s^2)^2 \sim \frac{Q_s^2(x)}{Q^2} \propto x^{-\lambda} \tag{12}$$

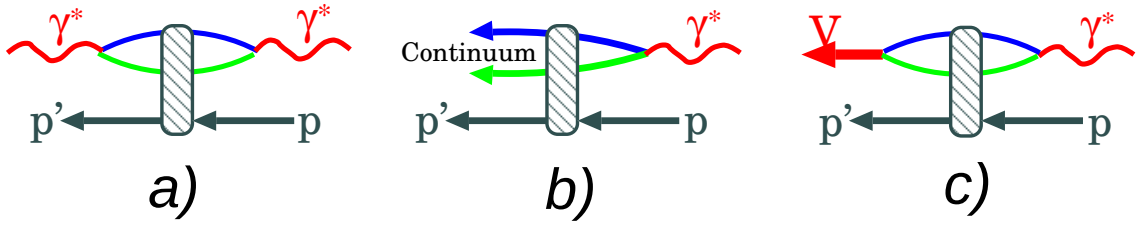

Figure 29: The unified picture of Compton scattering, diffraction excitation of the photon into hadronic continuum states and into the diffractive vector meson

and it follows immediately that $\frac{\sigma^{diff}}{\sigma^{tot}}$ is a constant of x at fixed values of Q^2. This result is illustrated experimentally at the beginning of this review, in Fig. 8.

With Eq. 10, we have also introduced above an interesting consequence of the dipole model for the total cross section, the geometric scaling property. Namely, the total cross section does not depend on x and Q^2 independently but can be expressed as a function of a single variable $\tau = Q^2/Q_s^2(x)$ [20]. This property has also been shown recently to be verified under minimal assumptions for all diffractive processes [21] (see Fig. 30). The experimental confirmation of this relation is an interesting piece of evidence that saturation effects are (already) visible in the inclusive diffractive DIS data. Extensions of these ideas at non-zero t values, rooted on fundamental grounds, have also been recently derived [19]. This provides essential perspectives to understand the transverse degrees of freedom which are discussed in the next sections.

7.4 Towards a common description of all diffractive processes

Let us mention that one of the great interest of the dipole model in its two-gluon exchange formulation is that it provides a unified description of different processes measured in $\gamma^* p$ collisions at HERA: inclusive $\gamma^* p \to X$, diffractive $\gamma^* p \to X\ p'$ and (diffractive) exclusive vector mesons (VM) production $\gamma^* p \to VM\ p'$ (see Fig. 29). In the last case, the step (3) described in Fig. 25 consists in the recombination of the scattered pair $q\bar{q}$ onto a real VM (as J/Ψ, ρ^0, ϕ,...) [22, 23, 24, 25] or onto a real photon for the reaction $\gamma^* p \to \gamma\ p'$. This last process is called deeply virtual Compton scattering (DVCS) [26, 27]. Also, we understand immediately the fundamental interest of exclusive VM production to clarify the generic mechanism of diffractive DIS. Indeed, the scales involved in the VM process can act as triggers to isolate when the virtual photon fluctuates mainly into small-size (small r) $q\bar{q}$ pair configurations, or mainly into large-size configurations. For example, a small-size $q\bar{q}$ dipole is most likely to be produced if the virtual photon is polarized longitudinally or if the dipole is built with heavy quarks. Therefore, we can already state that exclusive J/Ψ production is a good candidate for a hard diffractive process fully calculable in perturbative QCD. We discuss completely these ideas in the next section.

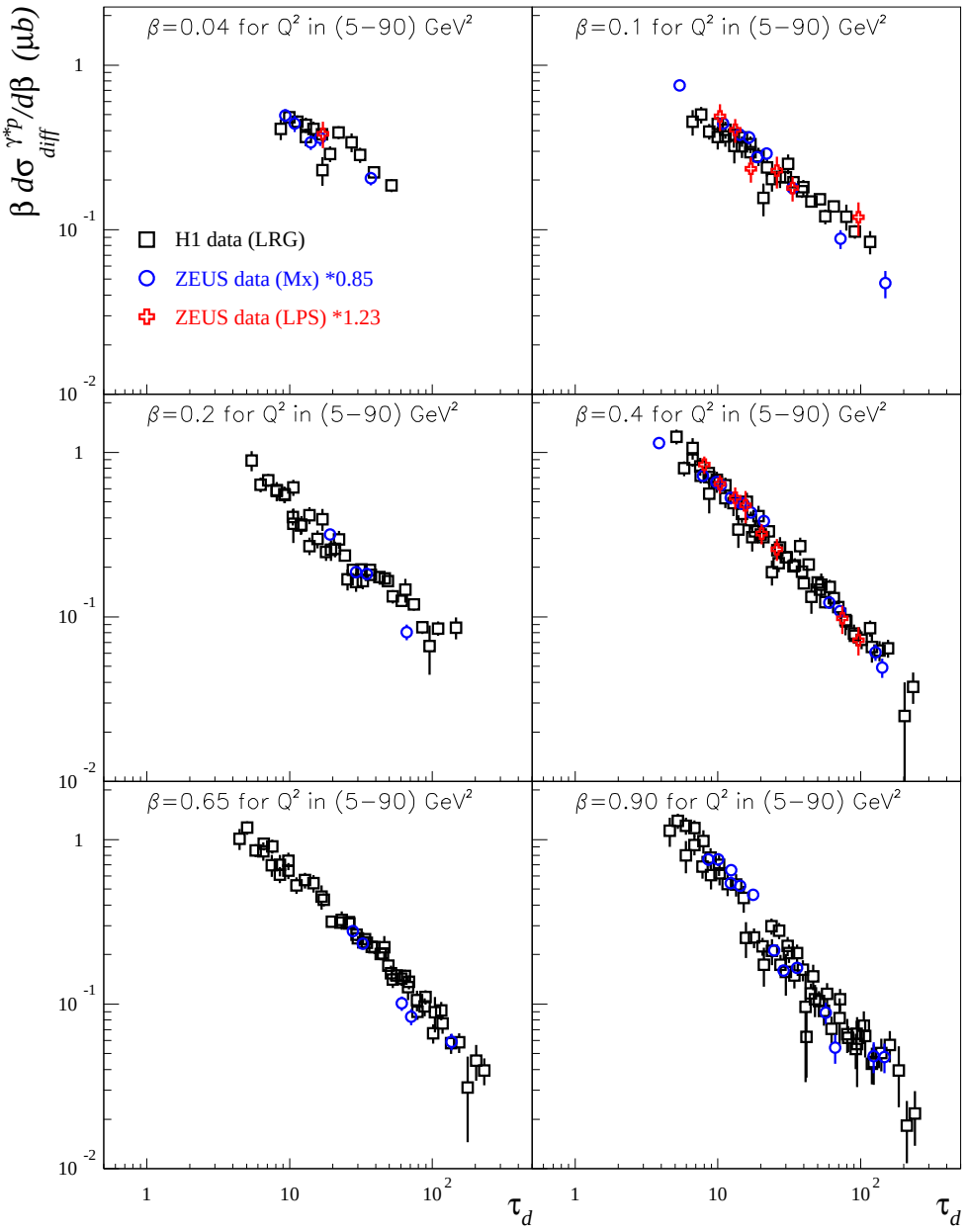

Figure 30: The diffractive cross section $\beta\, d\sigma_{diff}^{\gamma^* p \to Xp}/d\beta$ from H1 and ZEUS measurements, as a function of $\tau_d = Q^2/Q_s^2(x_{\mathbb{P}})$ in bins of β for Q^2 values in the range $[5; 90]$ GeV^2 and for $x_{\mathbb{P}} < 0.01$ [21]. The geometric scaling is confirmed with a good precision.

8 Exclusive particle production at HERA

8.1 Triggering the generic mechanism of diffractive production

There is a long experimental and theoretical history to the study of vector meson production, revived with the advent of HERA. On the experimental side, the important result is that the cross sections for exclusive vector meson production rise strongly with energy (if a hard scale is present) when compared to fixed target experiments. A compilation of experimental measurements are shown in Fig. 31 [22, 23, 24, 25]. We observe some statements mentioned briefly at the very end the previous section. For example, for J/ψ exclusive production, the W dependence of the cross section is typical of a hard process. Indeed, the mass of the J/ψ plays the role of the large scale, which mainly triggers small-size (small r) $q\bar{q}$ pair configurations of the initial virtual photon, which then build the hard process. If we follow the discussion of the previous section, we can also easily write the above argument at a quantitative level. Indeed, VM cross sections in the (hard) perturbative regime, $\gamma^* p \to VM\ p'$, depend on the square of the gluon density in the proton. A first approximation of the cross section can then be written as

$$\left|\frac{d\sigma}{dt}\right|_{t=0}(\gamma^* N \to VN) = 4\pi^3 \Gamma_V m_V \alpha_s^2(Q) \frac{\eta_V^2 \left(xg(x,Q^2)\right)^2}{3\alpha_{\rm em} Q^6}\ , \tag{13}$$

where the dependence on the meson structure is in the parameter

$$\eta_V = \frac{1}{2}\int \frac{dz}{z(1-z)} \phi^V(z) \left(\int dz \phi^V(z)\right)^{-1} \tag{14}$$

and $\phi^V(z)$ is the leading-twist light-cone wave function.

Fig. 31 presents also interesting features that we can comment at this level of the discussion. It shows the transition from soft to hard processes, using the mass of the VM as a trigger. From the lightest one, ρ^0, up to the Υ, Fig. 31 shows $\sigma(\gamma p \to Vp)$ as a function of W. For comparison, the total photoproduction cross section, $\sigma_{tot}(\gamma p)$, is also shown. The data at high W can be parameterized as W^δ, and the value of δ is displayed in Fig. 31 for each reaction. One sees clearly the transition from a shallow W dependence for low mass VM (soft) to a steeper one as the mass of the VM increases (hard) [22, 23, 24, 25].

An interesting phenomenon is observed for the DVCS cross section (see Fig. 32), which presents the same hard W dependence as for the J/ψ [26, 27], with a (zero mass) photon in the final state. It does not seem to follow the logic of the above argument and we come back later of this point. Obviously, Fig. 31 displays only one aspect of the problem, using the mass of the VM as the scale trigger for the soft-hard diffractive process. It is clear that the scale Q^2 is also particularly well suited, always for the exclusive electroproduction of light vector mesons [22, 23, 24, 25] and DVCS [26, 27]. The soft-hard transition can be observed experimentally in different ways when varying Q^2:

(1) In the change of the logarithmic derivative δ of the process cross section σ with respect to the $\gamma^* p$ center-of-mass energy W ($\sigma \sim W^\delta$). We expect a variation from a value of about 0.2 in the soft regime (low Q^2 values) to 0.8 in the hard one (large Q^2 values).

(2) In the decrease of the exponential slope b of the differential cross section with respect to the squared-four-momentum transfer t ($d\sigma/dt \sim e^{-b|t|}$), from a value of about 10 GeV^{-2} to an asymptotic value of about 5 GeV^{-2} when the virtuality Q^2 of the photon increases.

We illustrate this procedure on recent data on ρ^0 production [22]. The cross section $\sigma(\gamma^* p \to \rho^0 p)$ is presented in Fig. 33 as a function of W, for different values of Q^2. The cross section rises with W in all Q^2 bins. The same conclusion holds for DVCS, as already discussed and shown in Fig. 32 [26, 27].

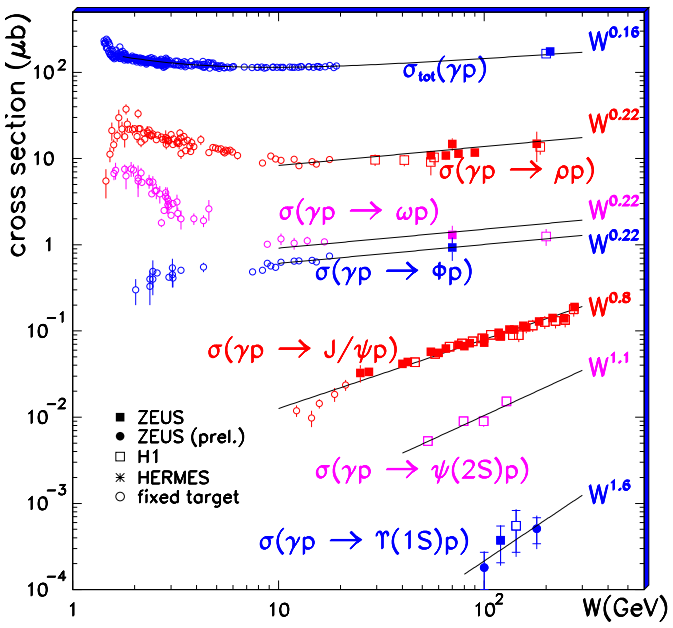

Figure 31: W dependence of the exclusive vector meson cross section in photoproduction, $\sigma(\gamma p \to Vp)$. The total photoproduction cross section is also shown. The lines are the fit result of the form W^{δ} to the high energy part of the data.

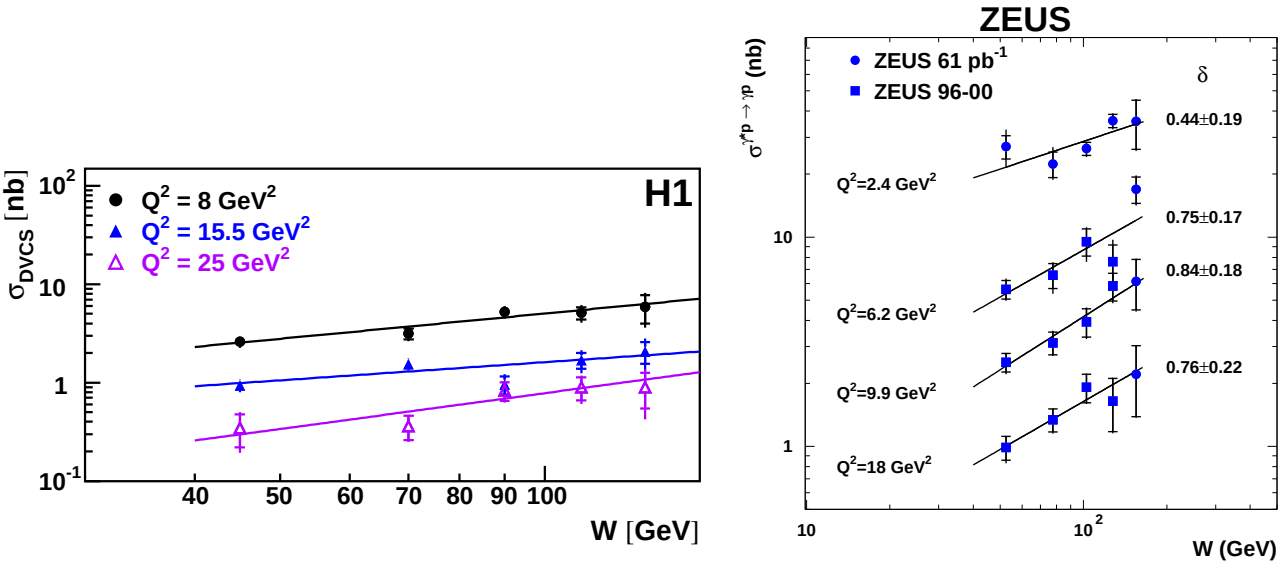

Figure 32: The DVCS cross section, $\sigma^{\gamma^* p \to \gamma p}$, as a function of W for different Q^2 values. The solid lines are the results of a fit of the form $\sigma^{\gamma^* p \to \gamma p} \propto W^{\delta}$. The values of δ and their statistical uncertainties are given in the figure.

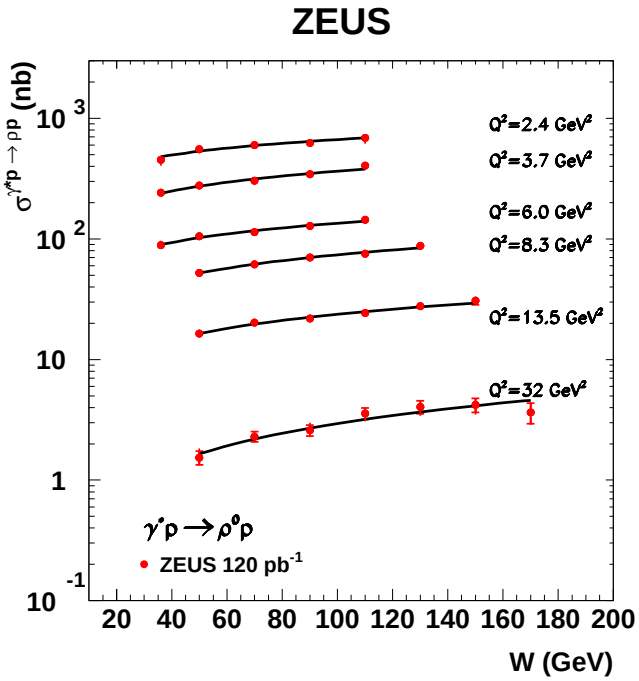

Figure 33: W dependence of the cross section for exclusive ρ^0 electroproduction, for different Q^2 values, as indicated in the figure. The lines are the fit results of the form W^δ to data.

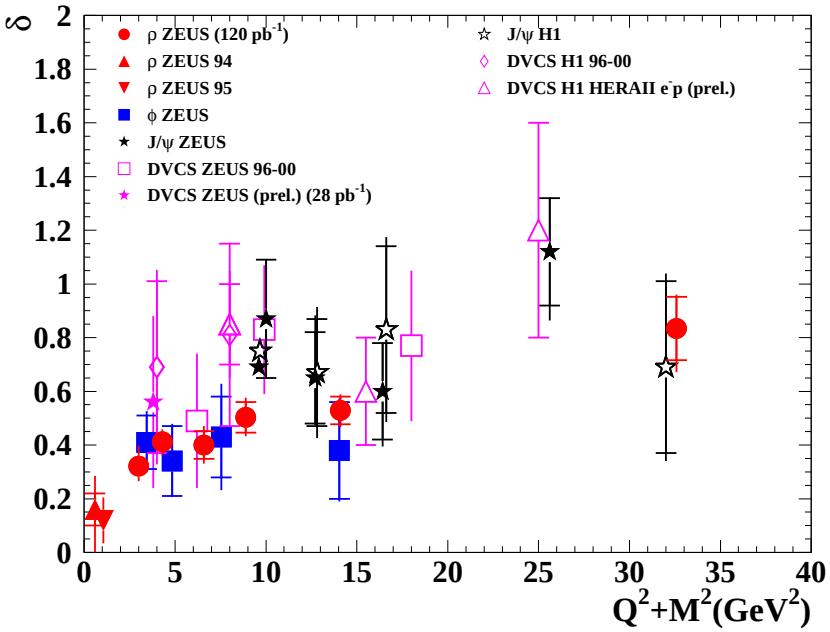

Figure 34: A compilation of values of δ from fits of the form W^δ for exclusive VM electroproduction, as a function of $Q^2 + M^2$. It includes also the DVCS results.

A compilation of values of δ from DVCS and VM measurements are presented in Fig 34. Results are plotted as a function of $Q^2 + M^2$, where M is the mass of the vector meson (equal to zero in case of DVCS). We observe a universal behavior, showing an increase of δ as the scale becomes larger. The value of δ at low scale is the one expected from the soft Pomeron intercept, while the one at large scale is in accordance with twice the logarithmic derivative of the gluon density with respect to W.

8.2 Deeply virtual Compton scattering

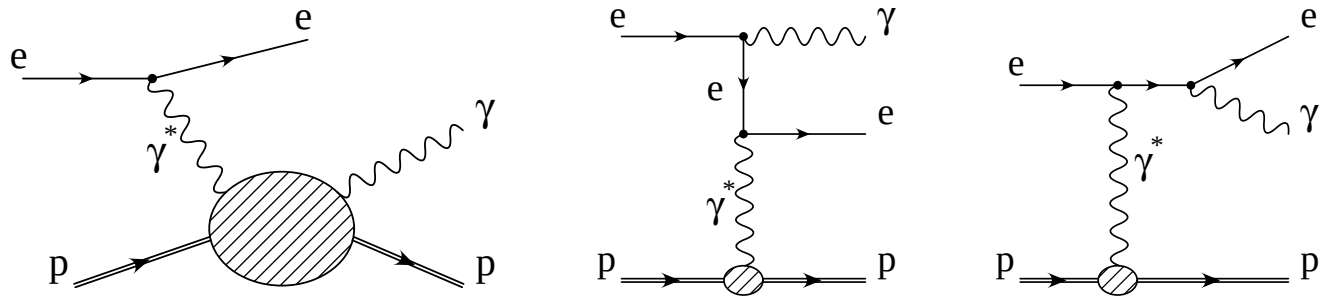

Figure 35: Diagrams illustrating the DVCS (left) and the Bethe-Heitler (middle and right) processes. The reaction studied receives contributions from both the DVCS process, whose origin lies in the strong interaction, and the purely electromagnetic Bethe-Heitler (BH) process, where the photon is emitted from the positron. The BH cross section can be precisely calculated in QED using elastic proton form factors.

Let us comment in more details the analysis of the DVCS signal, which we discuss in a different context in further sections. The DVCS process, $ep \to ep\gamma$, also receives a contribution from the purely electromagnetic Bethe-Heitler (BH) process, where the photon is emitted from the electron, as displayed in Fig. 35.

Let us notice that the final state for DVCS (QCD process) and BH (QED process) are identical. This means that both processes interfere, which is of fundamental interest in the next sections. In this part, we only use the fact that the BH cross section is precisely calculable in QED and can be subtracted from the total process rate to extract the DVCS cross section. Of course, only if the BH contribution is not dominating the process rate and if the (integrated) interference term is negligible. Otherwise, the subtraction procedure would be hopeless. It is the case at low x_{Bj}, and then for H1 and ZEUS experiments, the DVCS contribution can be measured directly. Fig. 36 presents the different contribution (for the scattered electron variables), after the experimental analysis of the reaction $ep \to ep\gamma$.

We observe that DVCS and BH contributions are of similar size and thus, the BH contribution can be subtracted with a systematic uncertainty determined from a specific experimental study. In Fig. 37, we present the DVCS cross sections, $\gamma^* p \to \gamma p$, obtained over the full kinematic range of the analysis [26, 27], as a function of Q^2 and W. The behavior in W has been discussed qualitatively above, it corresponds to the dependence characteristic for a hard process. The Q^2 dependence, measured to be in $\sim 1/Q^3$ in Fig. 37, is also understandable qualitatively.

Indeed, following the discussion of the previous section (see Eq. (12)), we expect a behavior of the imaginary DVCS amplitude ($\gamma^* p \to \gamma p$) in

$$ImA \sim \sigma_0 \frac{1}{Q^2} \int_{1/Q^2}^{1/Q_s^2} \frac{dr^2}{r^4} (r^2 Q_s^2) \tag{15}$$

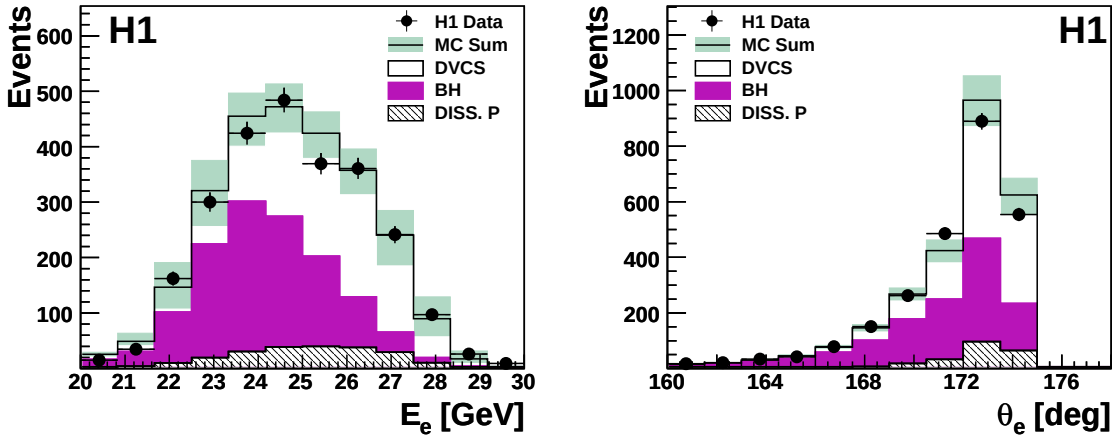

Figure 36: Distributions of the energy and polar angle of the scattered electron. The data are compared with Monte Carlo expectations for elastic DVCS, elastic and inelastic BH and inelastic DVCS (labelled DISS. p). All Monte Carlo simulations are normalized according to the luminosity of the data. The open histogram shows the total prediction and the shaded band its estimated uncertainty.

which leads to a DVCS cross section of the form

$$\sigma \sim \sigma_0 (\frac{Q_s(x)^2}{Q^2})^2 \sim \frac{W^\delta}{Q^4}$$

With this expression, we find again the qualitative behavior in W. Interestingly also, the measured Q^2 dependence in $\sim 1/Q^3$ is smaller than expected from this relation. In fact, to describe qualitatively the observed DVCS cross section, we must consider a parameterization in

$$\sigma \sim \sigma_0 \frac{W^\delta [Q^2]^\gamma}{Q^4},$$

after introducing a term in $[Q^2]^\gamma$ in the expression of the DVCS cross section. The term in $[Q^2]^\gamma$ is reminiscent from the QCD evolution of the DVCS amplitude (QCD evolution of the gluon/sea distributions). The experimental observation in $\sigma \sim 1/Q^3$ is compatible with $\gamma \sim 1/2$ (using our notations). Of course, we do not stay at this qualitative understanding and we describe quantitative estimates of the DVCS cross sections in the following.

A comment is in order concerning the W dependence of DVCS. It reaches the same value of δ as in the hard process of J/ψ electroproduction. Given the fact that the final state photon is real, and thus transversely polarized, the DVCS process is produced by transversely polarized virtual photons, assuming s-channel helicity conservation. The steep energy dependence thus indicates that the large configurations of the virtual transverse photon are suppressed and the reaction is dominated by small $q\bar{q}$ configurations (small dipoles), leading to the observed perturbative hard behavior. A similar effect is observed for ρ^0 production [22].

8.3 Saturation in exclusive processes

Coming back to the discussion of the previous section about saturation, we can mention also that among diffractive interactions, exclusive vector meson production and DVCS are probably the best processes

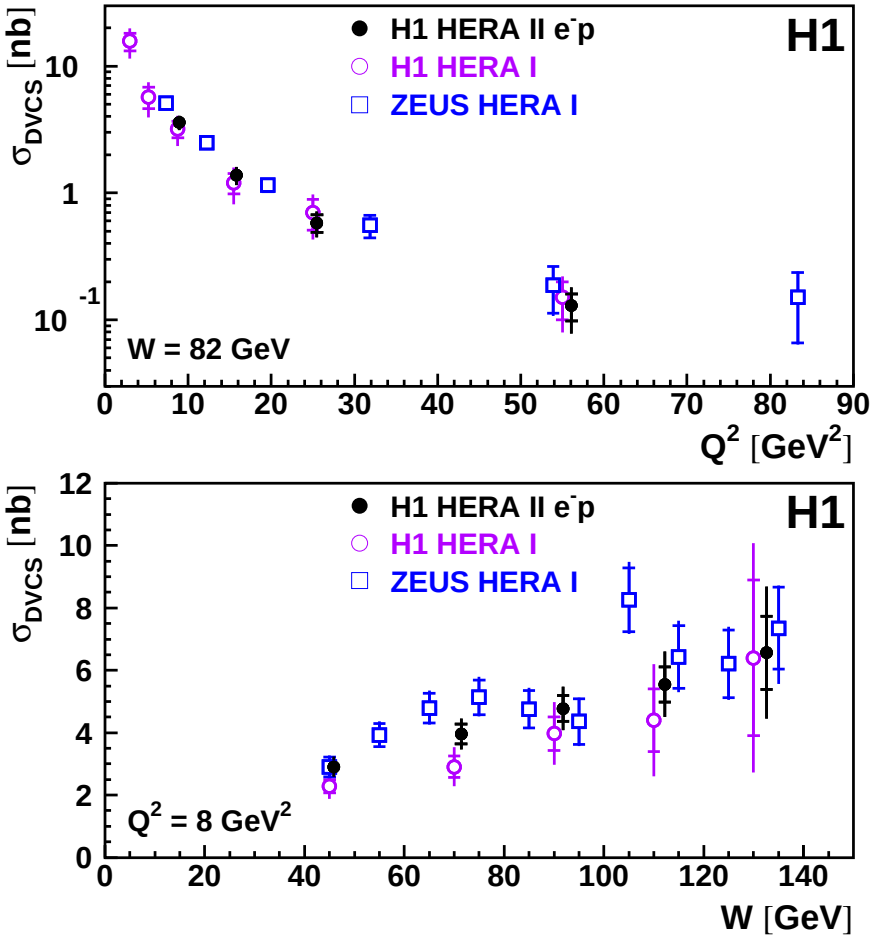

Figure 37: The DVCS cross section as a function of Q^2 at $W = 82$ GeV and as a function of W at $Q^2 = 8$ GeV^2. The inner error bars represent the statistical errors, the outer error bars the statistical and systematic errors added in quadrature.

to study saturation effects in DIS since the transverse size of the $q\bar{q}$ pair forming a meson is controlled by the vector meson mass with $< r > \simeq 1/\sqrt{M_V^2 + Q^2}$. Thus we expect saturation effects to be more important for larger (lighter) vector mesons. An interesting consequence of this feature is illustrated in Fig. 38, where we show that VM and DVCS process exhibit the property of geometric scaling [21]. This illustrates that this qualitative discussion (related to Eq. (15)) gives the main elements of understanding of the DVCS and VMs cross sections dependences. More generally, as for all other diffractive processes presented in this review, it means that the mechanism included in the parameterization of the dipole cross section of the form written in Eq. (10) is correct and predictive.

In recent works, it has been shown that dipole models can be extended at non-zero t values, with a refined definition of the saturation scale [19]. Then, the geometric scaling property is predicted to manifest itself in exclusive vector meson production and deeply virtual Compton scattering (DVCS), also at moderate non-zero momentum transfer. In Fig. 39, we compare data with predictions of Ref. [19], We observe the very good agreement between data and predictions.

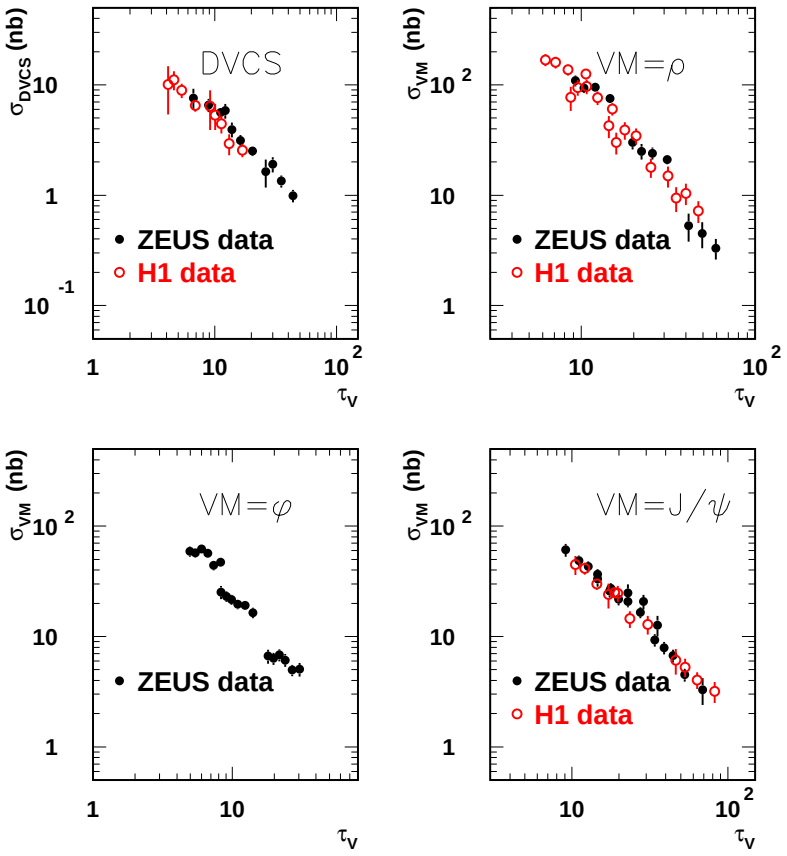

Figure 38: The ρ, J/Ψ and ϕ production cross-sections $\sigma_{VM}^{\gamma^* p \to Vp}$ and the DVCS cross-section $\sigma_{DVCS}^{\gamma^* p \to \gamma p}$ from H1 and ZEUS measurements, as a function of $\tau_V = (Q^2 + M_{VM}^2)/Q_s^2(x_{\mathbb{P}})$ and for $x_{\mathbb{P}} < 0.01$ [21]. Each process verifies the geometric scaling property.

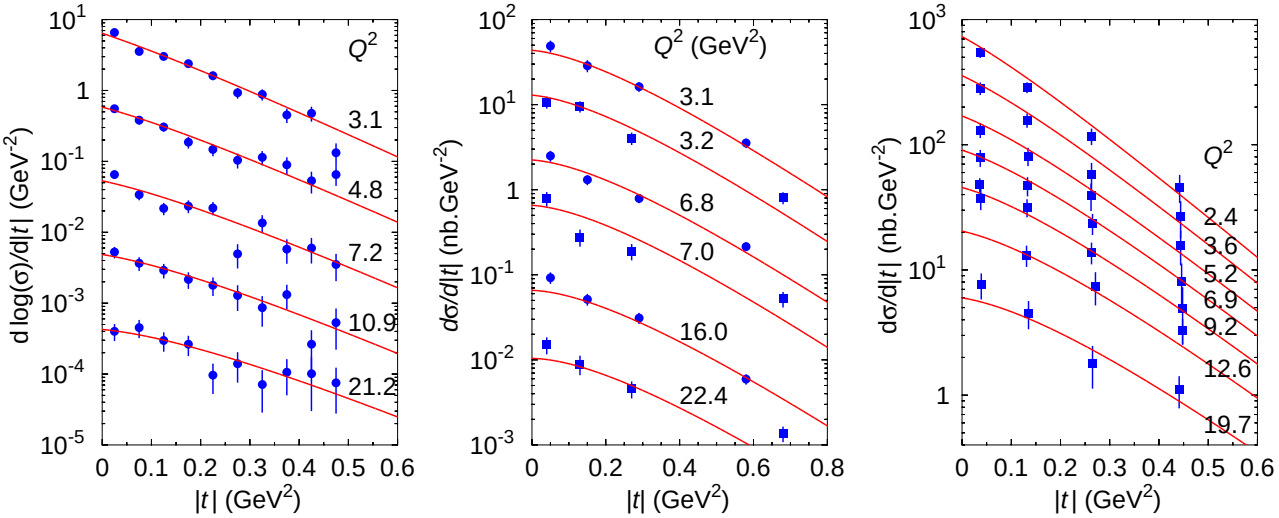

(a) ρ meson at $W = 75$ (b) J/Ψ meson at $W = 90$ (c) ϕ meson at $W = 75$

Figure 39: Fit results for the ρ, ϕ and J/Ψ differential cross-section.

9 Nucleon tomography

9.1 t dependence of exclusive diffractive processes revisited

With $t = (p - p')^2$, the measurement of the VM and DVCS cross section, differential in t is one of the key measurement in exclusive processes. A parameterization in $d\sigma/dt \sim e^{-b|t|}$, as shown in Fig. 40, gives a very good description of measurements. In addition, in Fig. 40, we show that fits of the form $d\sigma/dt \sim e^{-b|t|}$ can describe DVCS measurements to a very good accuracy for different Q^2 and W values. The same conclusions hold in the case of VM production. That's the reason why we use this parameterization of the t dependence, with a factorized exponential slope b, to describe the HERA data on DVCS or VM production at low x_{Bj}. Note that this parameterization

Concerning the interpretation, we have already briefly mentioned the importance of the observation of the decrease of the exponential slope b, from a value of about 10 GeV^{-2} to an asymptotic value of about 5 GeV^{-2}, when the virtuality Q^2 of the photon increases (see Fig. 41). The resulting values of b as a function of the scale $Q^2 + M^2$ are plotted in Fig. 41.

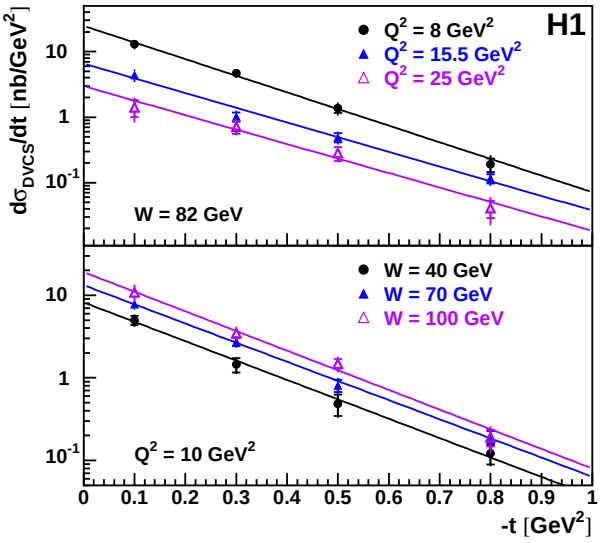

Figure 40: The DVCS cross section, differential in t, for three values of Q^2 expressed atand for three values of W. The solid lines represent the results of fits of the form $e^{-b|t|}$.

A qualitative understanding of this behavior is simple. Indeed, b is essentially the sum of a component coming from the probe in $1/\sqrt{Q^2 + M_{VM}^2}$ and a component related to the target nucleon. Then, at large Q^2 or large M_{VM}^2, the b values decrease to the solely target component. That's why in Fig. 41, we observe that for large Q^2 or for heavy VMs, like J/ψ, b is reaching a universal value of about 5 GeV^{-2}, scaling with Q^2 asymptotically. This value is related to the size of the target probed during the interaction and we do not expect further decrease of b when increasing the scale, once a certain scale is reached.

To understand this shape of $b(Q^2)$ more quantitatively, we need to define a function that generalizes the gluon density which appears in Eq. (13) at non-zero t values. That's why, we define a generalised gluon distribution F_g which depends both on x and t (at given Q^2). From this function, we can compute a gluon density which also depends on a spatial degree of freedom, a transverse size (or impact parameter), labeled $R_\perp$, in the proton. Both functions are related by a Fourier transform

$$g(x, R_\perp; Q^2) \equiv \int \frac{d^2\Delta_\perp}{(2\pi)^2} e^{i(\Delta_\perp R_\perp)} F_g(x, t = -\Delta_\perp^2; Q^2).$$

At this level of the discussion, there is no need to enter into further details concerning these functions. We just need to know that the functions introduced above define proper (generalized) PDFs, with gauge invariance and all the good theoretical properties of PDFs in terms of operator product expansion. In fact, they are rooted on fundamental grounds [28], that we develop in further sections (without heavy formalism).

9.2 Extracting the transverse distribution of the quarks and gluons

From the Fourier transform relation above, the average impact parameter (squared), $\langle r_T^2 \rangle$, of the distribution of gluons $g(x, R_\perp)$ is given by

$$\langle r_T^2 \rangle \equiv \frac{\int d^2R_\perp \; g(x,R_\perp) \; R_\perp^2}{\int d^2R_\perp \; g(x,R_\perp)} = 4 \, \frac{\partial}{\partial t} \left[\frac{F_g(x,t)}{F_g(x,0)} \right]_{t=0} = 2b, \tag{16}$$

where b is the exponential t-slope. In this expression, $\sqrt{\langle r_T^2 \rangle}$ is the transverse distance between the struck parton and the center of momentum of the proton. The latter is the average transverse position of the partons in the proton with weights given by the parton momentum fractions. At low x_{Bj}, the transverse distance defined as $\sqrt{\langle r_T^2 \rangle}$ corresponds also to the relative transverse distance between the interacting parton (gluon in the equation above) and the system defined by spectator partons. Therefore provides a natural estimate of the transverse extension of the gluons probed during the hard process.

In other words, a Fourier transform of momentum to impact parameter space readily shows that the t-slope b is related to the typical transverse distance in the proton. This t-slope, b, corresponds exactly to the slope measured once the component of the probe itself contributing to b can be neglected, which means at high scale: Q^2 or M_{VM}^2. Indeed, at high scale, the $q\bar{q}$ dipole is almost point-like, and the t dependence of the cross section is given by the transverse extension of the gluons in the proton for a given x_{Bj} range.

9.3 Comments on the physical content of $\langle r_T^2 \rangle$

A short comment is in order concerning the fundamental relation (16) for DVCS at HERA (at low x_{Bj}). Does it make sense to keep only the gluon distribution in this expression or do we need to consider also sea quarks? This issue can be addressed simply by coming back to Eq. (15), where we have approximated the imaginary DVCS amplitude ($\gamma^* p \to \gamma p$) in

$$ImA \sim \sigma_0 \frac{1}{Q^2} \int_{1/Q^2}^{1/Q_s^2} \frac{dr^2}{r^4} (r^2 Q_s^2).$$

Let us give first a more general form to this formula, keeping the tracks of the photon wave functions

$$ImA = \int d^2r \, dz \, \Psi^*(r,z,Q_1^2 = Q^2) \Psi(r,z,Q_2^2 = 0) \hat{\sigma}(x,r), \tag{17}$$

where $\Psi^*(r,z,Q_1^2 = Q^2)$ is the wave function for the virtual photon and $\Psi(r,z,Q_2^2 = 0)$ for the real photon. Also, following the previous discussion on the dipole cross section, we can write: $\hat{\sigma}(x,r) \sim \sigma_0 r^2 Q_s(x,r)^2$, with

$$Q_s(x,r)^2 \sim \frac{\alpha_S \; xg(x,1/r^2)}{\pi R_p^2} \sim Q_0^2 (\frac{x_0}{x})^\lambda,$$

where R_p is the proton radius. We conclude immediately that the imaginary part of the DVCS amplitude is dependent on the gluon density convoluted by the photon (virtual and real) wave functions. It gives the rationale behind formula (16).

Of course, this is a matter of representation. In the Eq. (17), we write the photon-gluon interaction through a quark loop, with a virtual photon fluctuating in a $q\bar{q}$ pair, which is exactly the dipole $q\bar{q}$ component entering in $\Psi^*(r, z, Q_1^2 = Q^2)$ (see also Fig. 29). In other words, at low x_{Bj} ($x_{Bj} \simeq 10^{-3}$), the idea is that quarks (sea quarks) are produced by gluons.

Then, the dipole formalism, summarized in Eq. (17) or Fig. 29, provides a very powerful expression of this behavior. Of course, in other formalisms, that we present latter, we can express the cross sections at the level of the photon-quark interaction and thus consider directly the sea quark distribution.

9.4 Experimental results

DVCS results lead to $\sqrt{r_T^2} = 0.65 \pm 0.02$ fm at large scale $Q^2 > 8$ GeV^2 for $x_{Bj} \simeq 10^{-3}$ [26]. This value is smaller than the size of a single proton, and, in contrast to hadron-hadron scattering, it does not expand as energy W increases (see Fig. 42). Then, we can parametrize the measured b values displayed in Fig. 42 in the form of a Pomeron trajectory: $b = b_0 + 2\alpha' \ln \frac{1}{x_{Bj}}$. We obtain that the α' value, which is characteristic of the energy dependence of the trajectory, is close to zero.

This is not useless to recall that this observation is extremely challenging on the experimental analysis side. We are dealing with nano-barn cross sections, that we measure as a function of t, and finally, we measure the energy dependence of this behavior in t. Of course, the gain is important. In particular, the great interest of the DVCS is that the t dependence measured is free of effects that could come from VM wave functions (in case of VMs) and then spoil (to a certain limit) the interpretation of b described above. Thus, with DVCS, we have the advantage to work in a controlled environment (photon wave functions) where the generic Eq. (16) can be applied to the measurement (almost directly) and must not be corrected with effects arising from VMs wave function.

It is obviously very interesting to extend the result presented in Fig. 42 to all VMs. Indeed, we can study the W dependence of $\mathrm{d}\sigma/\mathrm{d}t$ and extract the energy dependence as done above for all VMs, using $b = b_0 + 2\alpha' \ln \frac{1}{x_{Bj}}$. Results are presented in Fig. 43 (bottom). Values are plotted as a function of $Q^2 + M^2$. We observe that the values of α' tends to decrease with the scale. In particular, the measurement of α' done for the J/Ψ [24], leading to a small value for α', is well compatible with the DVCS result [26].

A short comment can be done qualitatively on such small α' value. We can rephrase this observation as an evidence of no shrinkage of $d\sigma/dt$ in the process $\gamma^* p \to J/\Psi p$ or $\gamma^* p \to \gamma p$. Looking at the diagram describing two gluon exchange in Fig. 44, the virtual photon fluctuates into two high k_T quarks. Although in the diagram there are only two gluons linked to the proton, we actually have a whole ladder due to the large rapidity range available at these high W energies (see Fig. 44). From the virtual photon vertex down to the proton, the average k_T of the gluons gets smaller, the configuration larger and we enter the region of low k_T physics governed by non-perturbative QCD. This process is called Gribov diffusion. Thus a process can start as a hard process at the photon vertex but once it couples to the proton it gets a soft component which makes the process non calculable in pQCD. The average k_T of the partons in the process can be estimated by the slope of the trajectory since $\alpha' \sim 1/ < k_T >$.

The fact that no shrinkage is observed indicates that Gribov diffusion is not important in this process at the presently available W values, and the average k_T remains large. Such a behavior is expected for hard processes, where $\alpha' \ll 0.25$ GeV^{-2}. The experimental results for exclusive J/Ψ production and DVCS confirm that both processes are fully calculable in perturbative QCD.

9.5 Link with LHC issues

Let us finish this section by a comment making the link with LHC issues. Indeed, the correlation between the transverse distribution of partons and their momentum fraction is not only interesting

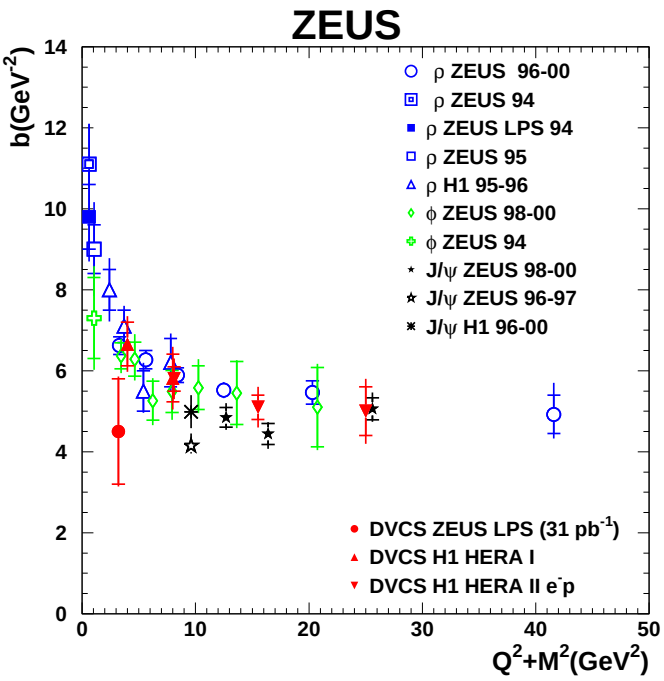

Figure 41: A compilation of the values of the slope b as a function of $Q^2 + M^2$ for various exclusive processes including the present DVCS measurement. The inner error bars represent the statistical uncertainty while the outer error bars the statistical and systematic uncertainties added in quadrature. Note that the latest t slope measurement of DVCS by the ZEUS collaboration [27] is shown. It falls below (1 sigma effect) the H1 measurement at a comparable Q^2 value [26]. The main result does not change: at large Q^2, exponential t slopes converge to a scaling value (see text) ans this is a common trend for all VM processes. However, at low Q^2 ($Q^2 \simeq 3$ GeV^2), ZEUS result indicates the absence of effects in $b \sim 1/Q^2$ (from the probe) for DVCS, whereas H1 result shows a behavior comparable to ρ at this Q^2, with a clear influence of the probe to the building of the measured b.

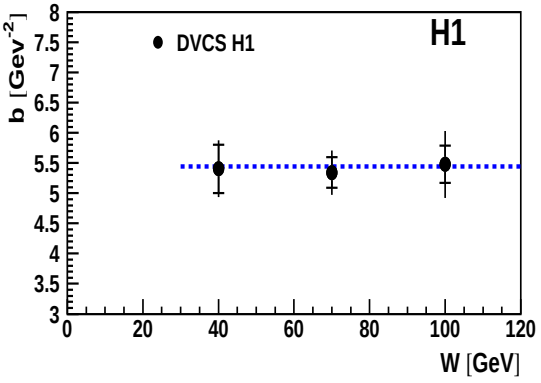

Figure 42: The logarithmic slope of the t dependence for DVCS as a function of W.

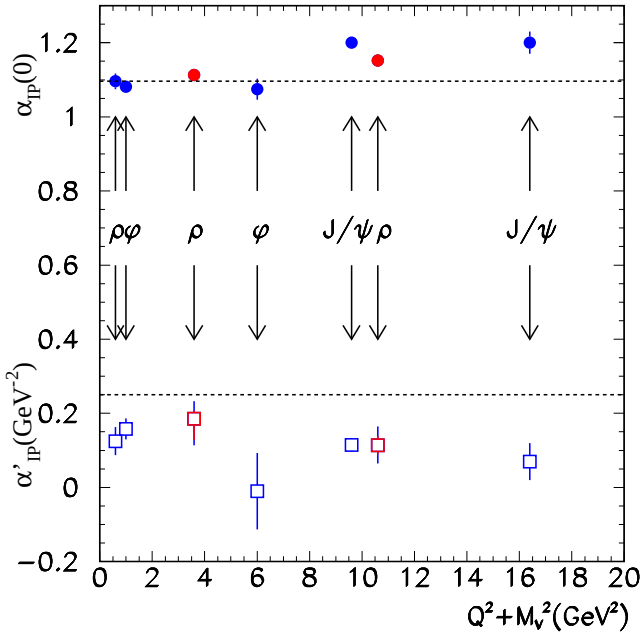

Figure 43: Values of the intercept and slope of the effective Pomeron trajectory as a function of $Q^2 + M^2$, as obtained from measurements of exclusive VM electroproduction.

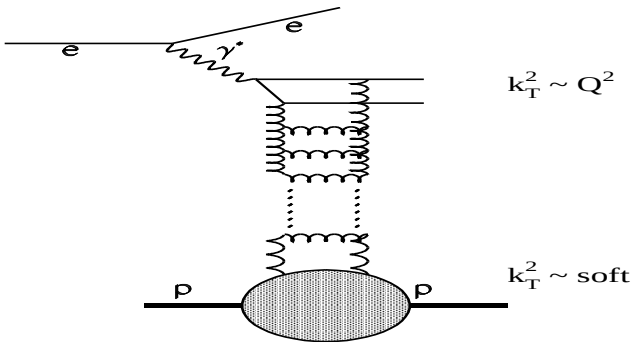

Figure 44: A diagram describing a gluon ladder in a diffractive process.

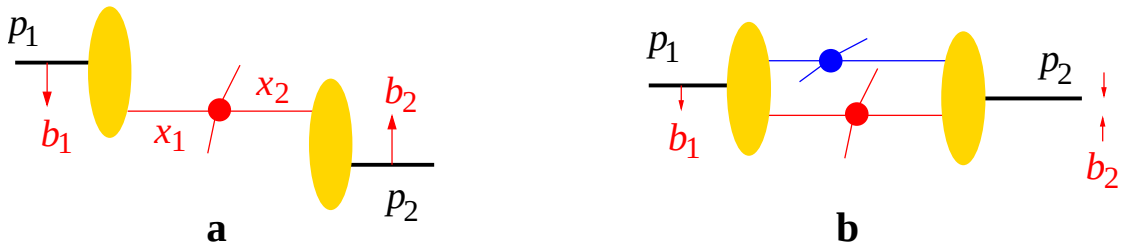

Figure 45: a: Graph with a single hard interaction in a hadron-hadron collision. The impact parameters b_1 and b_2 are integrated over independently. b: Graph with a primary and a secondary interaction.

from the perspective of hadron structure, but also has practical consequences for high-energy hadron-hadron collisions. Consider the production of a high-mass system (a dijet or a heavy particle). For the inclusive production cross section, the distribution of the colliding partons in impact parameter is not important: only the parton distributions integrated over impact parameters are relevant according to standard hard-scattering factorization (see Fig. 45(a)). There can however be additional interactions in the same collision, especially at the high energies for the Tevatron or the LHC, as shown in Fig. 45(b). Their effects cancel in sufficiently inclusive observables, but it does affect the event characteristics and can hence be quite relevant in practice. In this case, the impact parameter distribution of partons must be considered.

The production of a heavy system requires large momentum fractions for the colliding partons. A narrow impact parameter distribution for these partons forces the collision to be more central, which in turn increases the probability for multiple parton collisions in the event (multiple interactions).

10 Generalised parton distributions

10.1 A brief introduction in simple terms

We have already defined in a previous section a first form for a generalized gluon distribution. In this part, we move into further details and explain the wide experimental field opened in the area of generalized parton distributions.

First, a short contrarian comment: DIS can not be considered as the continuation of the original Rutherford experiment. Indeed, Rutherford measured that the nucleus is concentrated in a very small part of the atom, and, as far as we consider only PDFs, we have no possibility to explore the spatial structure of the nucleon. The reason is that in the infinite momentum frame picture, the light-cone description of the Feynman parton model does not explore the space-time location of partons. In other words, within the infinite momentum frame description, the variable x_{Bj} has no direct relation to the space coordinate of a parton but is related to a combination of the energy and momentum of this parton.

In the previous section, we have shown that data on exclusive particle production can give access to the spatial distribution of quarks and gluons in the proton at femto-meter scale. Then, we have defined functions, which model this property (for gluons) through the relation

$$g(x, R_\perp; Q^2) \equiv \int \frac{d^2\Delta_\perp}{(2\pi)^2}\, e^{i(\Delta_\perp R_\perp)}\, F_g(x, t = -\Delta_\perp^2; Q^2).$$

Of course, a similar relation holds for quarks, linking the two functions $q(x, R_\perp; Q^2)$ and $F_q(x, t = -\Delta_\perp^2; Q^2)$. The general framework for this physics is encoded in the so-called generalized parton distributions (GPDs).

We already know that the reconstruction of spatial images from scattering experiments by way of Fourier transform of the observed scattering pattern is a technique widely used in physics, for example, in X-rays scattering from crystals. In simple words, what we have done experimentally is that we have extended this technique to the spatial distribution of quarks and gluons within the proton, using processes that probe the proton at a tiny resolution scale. Of course, as already mentioned, working at a femto-meter scale with nano-barn cross sections is very challenging from the experimental front. We have achieved this and it immediately opens a way in the ambitious program of mapping out the GPDs. We come back below in a more systematic way on different aspects of that program that requires a large amount of experimental informations, for which future programs at JLab and CERN are appealing.

Before coming back to the experimental side, we can present a short overview of GPDs, in simple terms. It is interesting, even for an experimentalist, as it clarifies the Fourier transform relation discussed above and makes more transparent the goals for the future. For complete reviews, see Ref. [28, 29, 30].

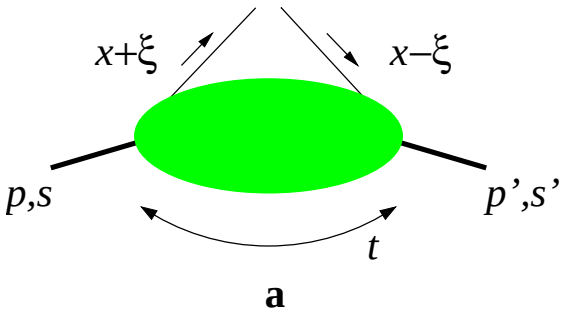

Figure 46: Picture of a GPD and its variables. The momentum fractions x and ξ refer to the average hadron momentum $\frac{1}{2}(p+p')$. Note that x is an internal variable and is not equal to x_{Bj}. However, there is a relation between the skewing variable ξ and x_{Bj}, $\xi = x_{Bj}/(2-x_{Bj})$.

GPDs are defined through matrix elements $\langle p'|\mathcal{O}|p\rangle$ between hadron states $|p'\rangle$ and $|p\rangle$, with non-local operators $\mathcal{O}$ constructed from quark and gluon fields. From this expression, we understand why GPDs are directly related to the amplitude for VM or real gamma exclusive production. For unpolarized quarks there are two distributions $H^q(x,\xi,t)$ and $E^q(x,\xi,t)$, where x and ξ are defined in Fig. 46. The former is diagonal in the proton helicity, whereas the latter describes proton helicity flip. For $p = p'$ and equal proton helicities, we recover the diagonal matrix element parameterized by usual quark and antiquark densities, so that $H^q(x,0,0) = q(x)$ and $H^q(-x,0,0) = -\bar{q}(x)$ for $x > 0$. Note that the functions of type E are not accessible in standard DIS, as it corresponds to matrix elements $\langle p', s'|\mathcal{O}|p, s\rangle$ with $s \neq s'$. Even in DVCS-like analysis, it is very difficult to get a sensitivity to these functions, as in most observables, their contributions are damped by kinematic factors of orders $|t|/M_p^2$, with an average $|t|$ value in general much smaller that 1 GeV^2. Then, till stated otherwise, our next experimental discussions are concentrated on the determination of GPDs of type H_q or H_g. We come back later on this point and show specific cases where E-type functions can be accessed and why this is an important perspective.

10.2 Fundamental relations between GPDs and form factors

An interesting property of GPDs, which lightens their physics content, is that their lowest moments give the well-known Dirac and Pauli form factors

$$\sum_q e_q \int dx\, H^q(x,\xi,t) = F_1(t) \qquad \sum_q e_q \int dx\, E^q(x,\xi,t) = F_2(t), \tag{18}$$

where e_q denotes the fractional quark charge. It means that GPDs measure the contribution of quarks/gluons, with longitudinal momentum fraction x, to the corresponding form factor. In other words, GPDs are like mini-form factors that filter out quark with a longitudinal momentum fraction x in the proton. Therefore, in the same way as Fourier transform of a form factor gives the charge distribution in position space, Fourier transform of GPDs (with respect to variable t) contains information about the spatial distribution of partons in the proton.

10.3 New insights into proton imaging

This discussion clarifies also the Fourier transforms, that can relate $g(x, R_\perp; Q^2)$ and $F_g(x, t = -\Delta_\perp^2; Q^2)$ or $q(x, R_\perp; Q^2)$ and $F_q(x, t = -\Delta_\perp^2; Q^2)$. We have already discussed these functions and from their relations, it follows that $q(x, R_\perp; Q^2)$ is the probability density to find a quark with momentum fraction

x at a transverse distance $R_\perp$ from the (transverse) center of momentum of the proton. More formal discussions can be found in Ref. [28].

Exactly, what must be confronted with the proton radius is not $\sqrt{r_T^2}$ but $\sqrt{r_T^2}/(1-x_{Bj})$, which does not change our result with $x_{Bj} \simeq 10^{-3}$ ($\sqrt{r_T^2} = 0.65 \pm 0.02$ fm), but must be taken into account for fixed target kinematics at larger x_{Bj}. In particular, at very large x_{Bj} ($x_{Bj} \to 1$), the struck quark is carrying almost the entire proton momentum, thus its relative distance to the center of momentum of the proton obviously tends to zero. This means that $\sqrt{r_T^2}$ tends to zero (by definition). In order to keep finite the ratio $\sqrt{r_T^2}/(1-x_{Bj})$, we can conclude that the asymptotic form of $\sqrt{r_T^2}$ at large x_{Bj} is likely in $(1-x_{Bj})^2$.

The distance $\sqrt{r_T^2}/(1-x_{Bj})$ is the associated transverse distance between the struck parton (probed during the hard interaction) and the center of momentum of the spectators. That's why it can be interpreted as a typical spatial extension of partons in the proton.

What we have learned so far with the present experimental situation is already very rich: slow partons (at low x_{Bj}) are located at the periphery of the proton whereas fast partons (at large x_{Bj}) make up the core of the proton (in its center). This last property is only an indirect observation from fits of form factor measurements [29] (see below for a short discussion).

We need to get more information. How large can be the spread in space of slow partons? Could it be larger that 1 fm? Also, what is the spread for the large x (constituent) partons? Where is the transition between the large x partons and the peripheric partons? We need more experimental results and then more experiments with different setups to address these questions from all possible angles.

For example, if we would observe a gradual increase of the t dependence of the GPD $H(x,0,t)$ (quarks or gluons) when varying x_{Bj} from large to small values, it would mean exactly that quarks at large x_{Bj} come from the more localized valence core of the proton, while the small x_{Bj} region receives contribution from the periphery or, in other words, from the wider meson cloud. This is a very nice perspective for the future to expect direct measurements of $\sqrt{r_T^2}$ from many experiments in the world.

10.4 An elegant application

Let us come back briefly to form factors and their essential role in the interplay between x and t kinematic variables. A complete analysis is presented by Diehl et al. in Ref. [31]. Indeed, it is clear that indirect information on impact parameter distributions can be obtained by using the sum rules presented in Eq. (18), which provides a natural link between the GPDs dependences in x and t. We can exemplify the structure of the link on the Dirac form factor for proton and neutron

$$F_1^p(t) = \int_0^1 dx[\frac{2}{3}H_v^u(x,t) - \frac{1}{3}H_v^d(x,t)]$$

$$F_1^n(t) = \int_0^1 dx[\frac{2}{3}H_v^d(x,t) - \frac{1}{3}H_v^u(x,t)]$$

where we have neglected the contribution from the s quarks. Note that only valence type distributions appear in these relations, since the electromagnetic current is only sensitive to the difference of quark and antiquark distributions. Then, from an ansatz for the functional dependence of $H_v^q(x,0,t)$ and measurements of the Dirac form factor $F_1(t)$ (and $F_2(t)$), a fit of some GPDs parameters can be performed [31].

Obviously, the sensitivity of such a fit is governed by the parameters building the interplay of x and t dependences (for valence distributions), which is the purpose of this approach. In Fig. 47 the default results for GPDs as tomography plots in impact parameter space is illustrated for fixed longitudinal momentum fraction x [31].

This confirms the results on $\sqrt{r_T^2}$ discussed above: low x_{Bj} partons are located at the periphery of the proton whereas valence like partons make up the core of the proton (in its center).

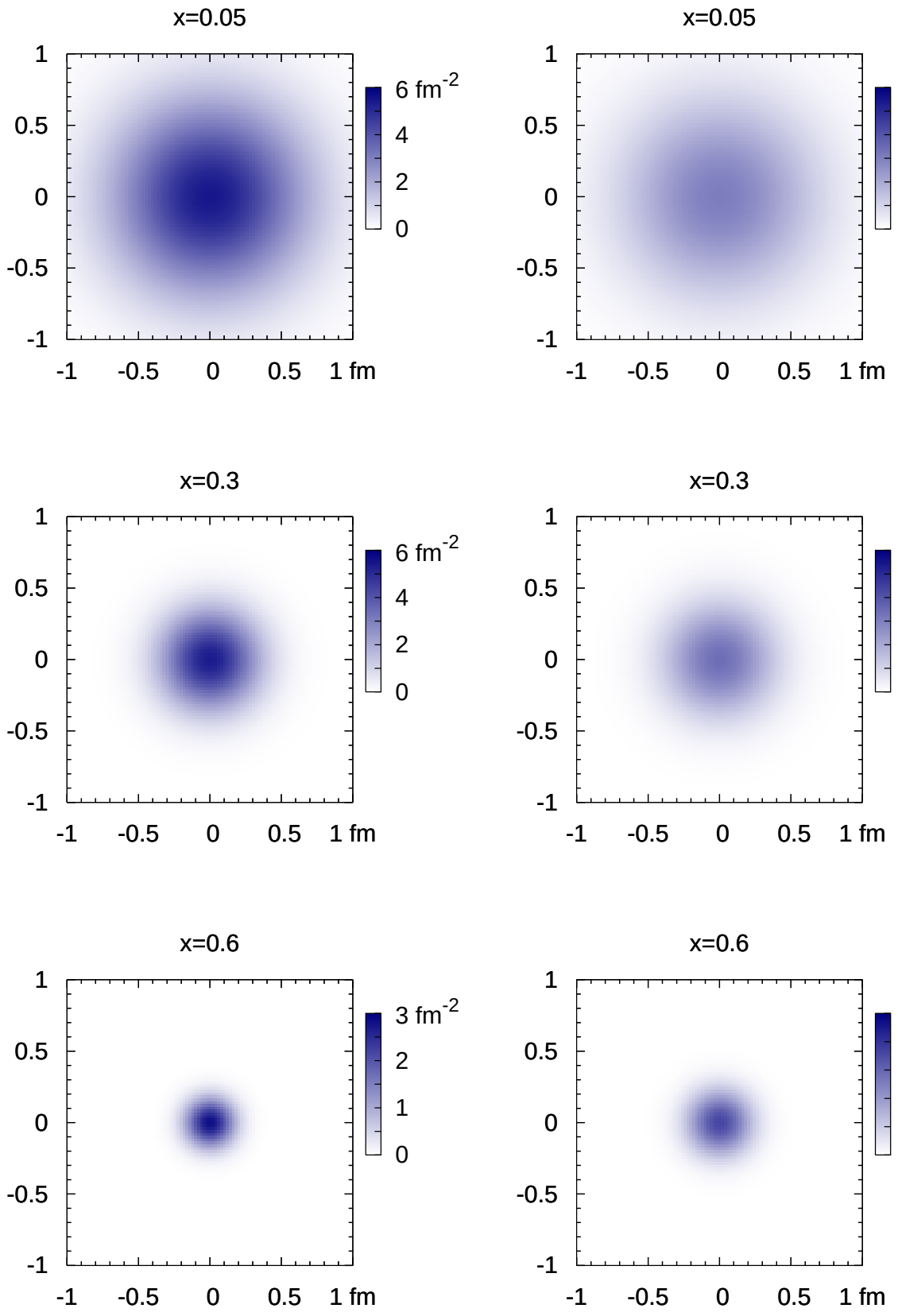

Figure 47: Tomography plots of $u_v(x, \mathbf{r_T})$ (left) and $d_v(x, \mathbf{r_T})$ (right) in the transverse r_T^x–r_T^y plane. Note that the scale of intensity for longitudinal momentum fraction $x = 0.6$ differs from the one for $x = 0.3$ and $x = 0.05$ [31].

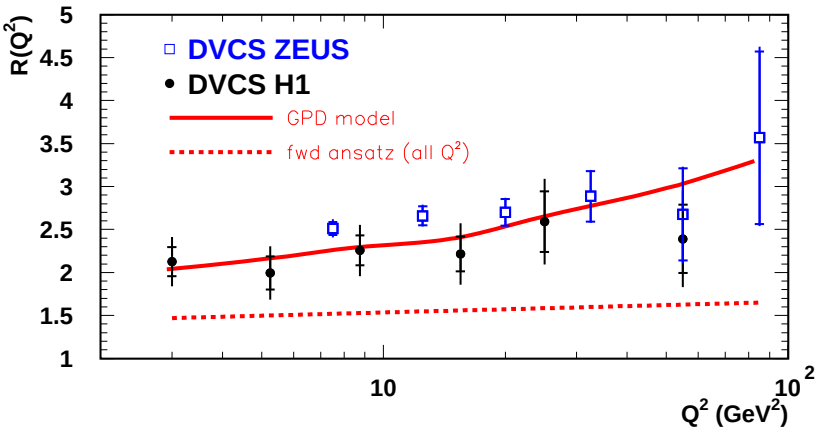

Figure 48: Skewing factor $R \equiv \mathcal{I}m\, A\,(\gamma^* p \to \gamma p)_{t=0} / \mathcal{I}m\, A\,(\gamma^* p \to \gamma^* p)_{t=0}$ extracted from DVCS and DIS cross sections [32] The GPD model is also displayed and gives a good agreement of the data (full line). The forward ansatz model [33], used at all values of Q^2, fails to reproduce the total skewing effects generated by the QCD evolution (dashed line).

11 Quantifying skewing effects on DVCS at low x_{Bj}

11.1 DVCS in the context of GPDs

After this short overview of GPDs physics, we understand clearly why DVCS is the typical (and cleanest) process to extract GPDs, or at least to extract informations on GPDs. Then, we can come back on the DVCS cross section measurements and their interpretation in terms of GPDs. In order to quantify the magnitude of skewing effects, and thus the impact of GPDs on the DVCS process ($\gamma^* p \to \gamma p$), we need to derive for example the following ratio from measured cross sections [26]

$$R \equiv Im\, A\,(\gamma^* p \to \gamma p)_{t=0} / Im\, A\,(\gamma^* p \to \gamma^* p)_{t=0}.$$

In this expression, $ImA(\gamma^* p \to \gamma p)_{t=0}(Q^2, W)$ is the imaginary part of the DVCS process and is directly proportional to the GPDs. Also, the diagonal term $Im\, A\,(\gamma^* p \to \gamma^* p)_{t=0}$ is directly proportinal to the total cross section. The ratio R is then is equivalent to the ratio of the GPDs to the PDFs. That's why its measurement can provide directly the impact of GPDs, when compared to pure PDFs predictions.

11.2 Experimental results

In Ref. [32], we have shown how to extract this ratio from the DVCS and DIS cross sections. Results are presented in Fig. 48. The typical values of R are found around 2, whereas in a model without skewing R would be equal to unity. Therefore, the present measurements confirm the large effect of skewing.

Values of R are also compared with a GPDs model based on a forward ansatz at low scale ($Q_0 = 1.3$ GeV) [33]. Namely, the singlet GPD is parametrized as follows: $H_S(x, \xi) = Q_S(x)$, where $Q_S(x)$ is the singlet PDFs and x and ξ are the variables used in the previous part for the definition of GPDs (see Fig. 46). It does not mean that the GPD is taken to be exactly the PDF. Indeed, at $x = \xi$, we get $H_S(\xi, \xi) = Q_S(\xi) = Q_S(x_{Bj}/2)$ and not $Q_S(x_{Bj})$. In other words, in this forward ansatz parameterization of the GPDs, we simply consider that at a low scale Q_0, we can forget the profile function and take directly the parameterization of the GPD from a PDF like form. The same is done with non-singlet and gluon distributions.

If the GPDs are parametrized in such a way at initial scale, then we have two possibilities. Either, we evolve the GPDs using skewed QCD evolution equations, which naturally generates the skewing dependence (in ξ) along the Q^2 evolution, or we forget about the skewed evolution and we consider only the standard QCD evolution equations like for PDFs [32, 33]. This corresponds to the two curves presented in Fig. 48. The full line represents the complete GPDs model, with skewed evolution equations and the dashed curve, labeled forward ansatz (all Q^2), represents the case where initial distributions are evolved with standard QCD evolution equations. Then, Fig. 48 demonstrates that we need the full GPDs model to describe our data on DVCS cross sections (converted in R values). If we forget about the skewing generated during the QCD evolution, we miss the data by about 30%. This is clearly a deep impact of the skewing effects present in the data [32, 33].

Another influence of GPDs that we can check on data concerns the t dependence. We have already shown that in the kinematic domain of H1 and ZEUS measurements, DVCS cross section ($d\sigma/dt$) can be factorized and approximated to a good accuracy by an exponential form $e^{-b|t|}$, which implies a factorized dependence in $e^{-b/2|t|}$ for GPDs. However, we can think of taking into account a non-factorized form in $|x|^{-\alpha'/2t}$ as well. With the small α' value determined previously, we know that this term can only be small (negligible) correction to the dominant (factorized) t dependence in $e^{-b/2|t|}$ for GPDs.

12 On the way of mapping out the GPDs

12.1 Prospects for the COMPASS experiment at CERN

As we have shown, the mapping of the GPDs is certainly a difficult work due to the flexibility of these functions. However, we have already illustrated some elements that can be constrained with the present DVCS data at low x_{Bj}. Concerning the t dependence of the GPDs in this kinematic domain, we have shown that the impact of a potential non-factorized term in $|x|^{-\alpha' t}$ is small, due to the small value of α' observed at low x_{Bj}.

This is one important element of the experimental project to measure DVCS at COMPASS in the future,as we need to check this kind of effects at larger x_{Bj}. DVCS at COMPASS (located at CERN) can be measured with muon beams on fixed target, $\mu p \to \mu p \gamma$. If the muon energy is large enough, for example $E_\mu = 190$ GeV, DVCS dominates over the BH contribution (as for H1 and ZEUS) so that DVCS cross section can be measured directly.

At smaller lepton energy, $E_\mu = 100$ GeV, the DVCS signal is not dominant and can not be measured directly. Then, we need to use the property that DVCS and BH, having identical final state, can interfere. When the DVCS cross section itself can not be measured, the interference can be observed. The strong interest is that the x_{Bj} kinematic domain of COMPASS follows the one of H1 and ZEUS at larger x_{Bj}, with $x_{Bj} \sim [0.05 - 0.15]$, thus much larger values than in the kinematic domain of H1 and ZEUS. A project is ongoing to install a proton recoil detector in the COMPASS setup and then measure DVCS cross section or DVCS/BH interference [36]. Some tests have already been done to show the technical feasibility of the proposed experiment.

Let us discuss how we can access an interference between DVCS and BH reactions. In fact, since these two processes have an identical final state, they can obviously interfere. The squared photon production amplitude is then given by

$$|A|^2 = |A_{BH}|^2 + |A_{DVCS}|^2 + \underbrace{A_{DVCS}\, A^*_{BH} + A^*_{DVCS}\, A_{BH}}_{I}, \tag{19}$$

where A_{BH} is the BH amplitude, A_{DVCS} represents the DVCS amplitude and I denotes the interference term.

For unpolarized proton target and lepton beam, the interference term can be written quite generally as a linear combination of harmonics of the azimuthal angle ϕ, which is the angle between the plane

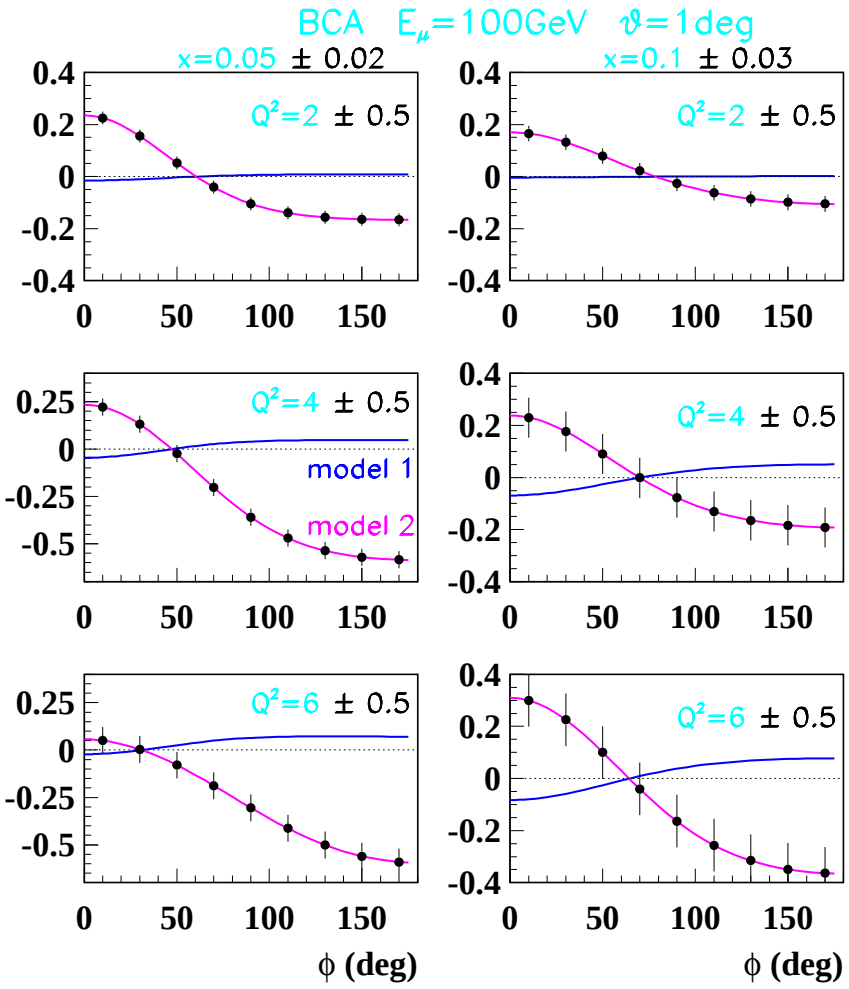

Figure 49: Azimuthal distribution of the beam charge asymmetry measured at COMPASS at E_μ= 100 GeV and $|t| \leq 0.6$ GeV^2 for 2 domains of x_{Bj} ($x_{Bj} = 0.05 \pm 0.02$ and $x_{Bj} = 0.10 \pm 0.03$) and 3 domains of Q^2 ($Q^2 = 2 \pm 0.5$ GeV^2, $Q^2 = 4 \pm 0.5$ GeV^2 and $Q^2 = 6 \pm 0.5$ GeV^2) obtained in 6 months of data taking with a global efficiency of 25% and with $2 \cdot 10^8$ μ per SPS spill ($P_{\mu^+} = -0.8$ and $P_{\mu^-} = +0.8$) [36].

containing the incoming and outgoing leptons and the plane defined by the virtual and real photons. In the leading twist approximation (at sufficiently high Q^2), if only the first term in $\cos\phi$ and $\sin\phi$ are considered, it can be written as:

$$I \propto -C\,[a\cos\phi\,\mathrm{Re}A_{DVCS} + bP_l\sin\phi\,\mathrm{Im}A_{DVCS}.] \tag{20}$$

In this expression, $C = \pm 1$ is the lepton beam charge, P_l its longitudinal polarization and a and b are functions of the ratio of longitudinal to transverse virtual photon flux [29].

At COMPASS, if we measure a beam charge asymmetry (BCA), the polarization of the muon beam flips with the charge and so, the $\sin\phi$ terms disappears. Then, the BCA reads

$$A_C = \frac{d\sigma^+/d\phi - d\sigma^-/d\phi}{d\sigma^+/d\phi + d\sigma^-/d\phi} \sim p_1\cos\phi = 2A_{BH}\frac{\mathrm{Re}A_{DVCS}}{|A_{DVCS}|^2 + |A_{BH}|^2}\cos\phi. \tag{21}$$

Note that DVCS cross section measurements which are integrated over ϕ are not sensitive to the interference term (see Eq. 20). Simulations done for COMPASS [36] are shown in Fig. 49 for BCA in a setup described in the legend of the figure. Two models of GPDs, with a factorized and non-factorized t dependence, are shown in Fig. 49 and we can observe easily the great discrimination power offered by

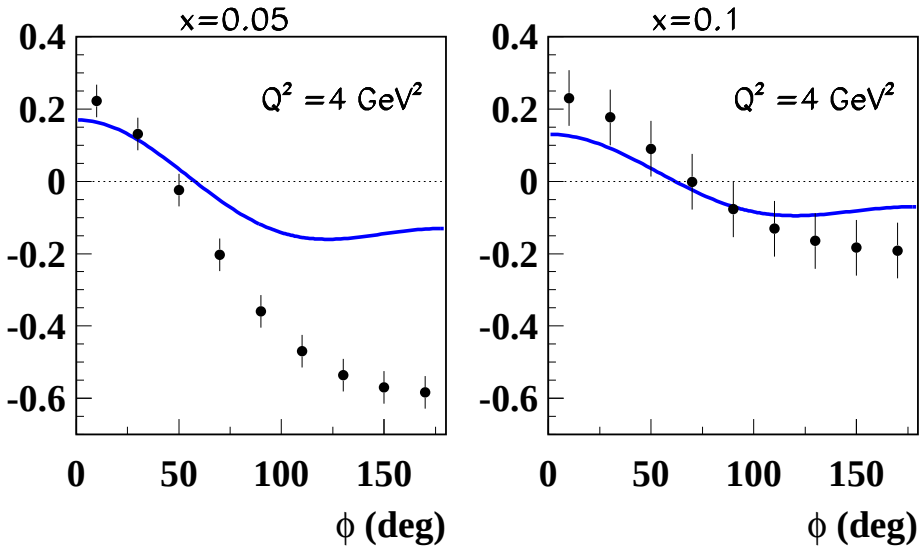

Figure 50: Simulation of the azimuthal angular distribution of the beam charge asymmetry measurable at COMPASS at $E_\mu = 100$ GeV. We present the projected values and error bars in the range $|t| < 0.6$ GeV^2 for 2 values of x_{Bj} (0.05 and 0.1) at $Q^2 = 4$ GeV^2 (see Ref. [36]). The prediction of the GPD model with a non-factorized t dependence is shown (full line). The case of a factorized t dependence would lead to a prediction of the BCA compatible with zero and is not displayed.

COMPASS, with the proton recoil detector fully operational [36]. Of course, the discrimination is large in Fig. 49 due to the fact that α' is taken to be large ($\alpha' \sim 0.8$ GeV^{-2}) in simulations. If it happens to be much smaller, as measured at low x_{Bj} by H1 [26] (see previous section), both predictions for BCA in Fig. 49 would be of similar shape, as both curves would converge to the factorized case.

In Fig. 50, we compare predictions of the GPD model used in the previous section for H1 data to simulations of the BCA extraction at COMPASS using a muon beam of 100 GeV [32]. We present the comparison for one value of Q^2 (4 GeV^2) and two values of x_{Bj} (0.05 and 0.1). When we compute the BCA in the factorized exponential t dependence approximation, we find values compatible with zero, which are not represented in Fig. 50.

Therefore, we display only the predictions of the model obtained in the non-factorized case using the same $\alpha' \sim 0.8$ GeV^{-2} value than in Ref. [36]. Both the $\cos(\phi)$ and $\cos(2\phi)$ terms contribute to a significant level to the BCA at COMPASS, as illustrated in Fig. 50. We notice that our predictions do not match with the COMPASS simulation done with the model described in Ref. [36]. This is another illustration of the large discriminative power of this observable on GPDs parameterizations, even for identical t dependence input.

12.2 Recent results on azimuthal asymmetries at HERA

At HERA, we have also samples of data with electron and positron beams. Therefore, it has been possible to extract the beam charge asymmetry, $A_C = \frac{d\sigma^+/d\phi - d\sigma^-/d\phi}{d\sigma^+/d\phi + d\sigma^-/d\phi}$. A former pioneering measurement of the BCA at HERMES [34] is shown in Fig. 51. HERMES was a fixed target experiment located at DESY operating with the electrons or positrons beams of 27.6 GeV. Recent results from HERMES [34] and H1 [26] are presented in Fig. 52 and 53, which correspond to $x_{Bj} \sim 0.1$ for HERMES and $x_{Bj} \sim 10^{-3}$ for H1. Note that for H1 results, we have kept a different convention in the definition of ϕ than in fixed target experiments, namely $\phi_{H1} = \pi - \phi_{HERMES}$. The advantage of the convention we have considered in H1 is that, a positive p_1 (with $BCA = p_1 \cos\phi$) means a positive real part of the

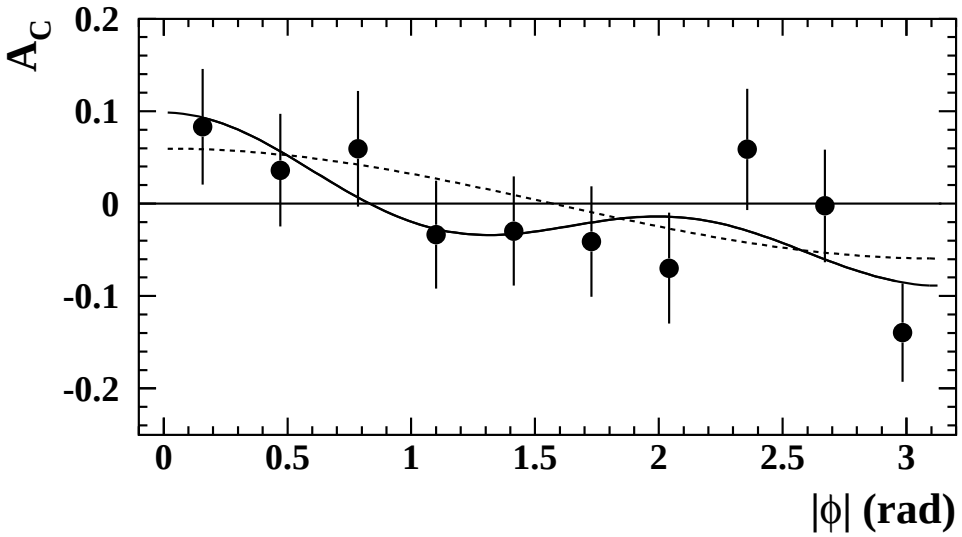

Figure 51: Beam charge asymmetry A_C from HERMES data as a function of $|\phi|$. Statistical uncertainties are shown. The solid curve represents the four–parameter fit: $(-0.011 \pm 0.019) + (0.060 \pm 0.027)\cos\phi + (0.016 \pm 0.026)\cos 2\phi + (0.034 \pm 0.027)\cos 3\phi$. The dashed line shows the pure $\cos\phi$ dependence.

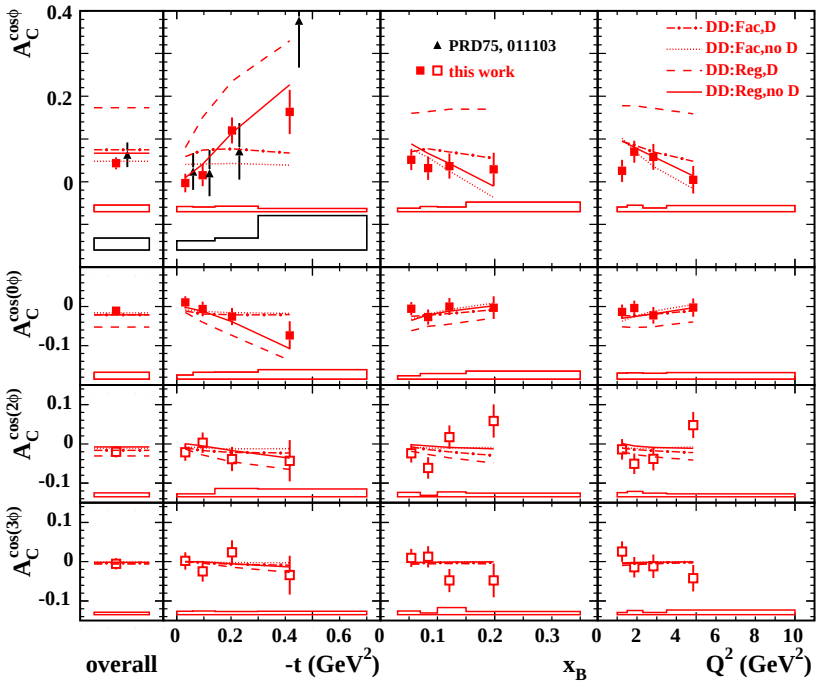

Figure 52: Moments of the Beam charge asymmetry from HERMES data.

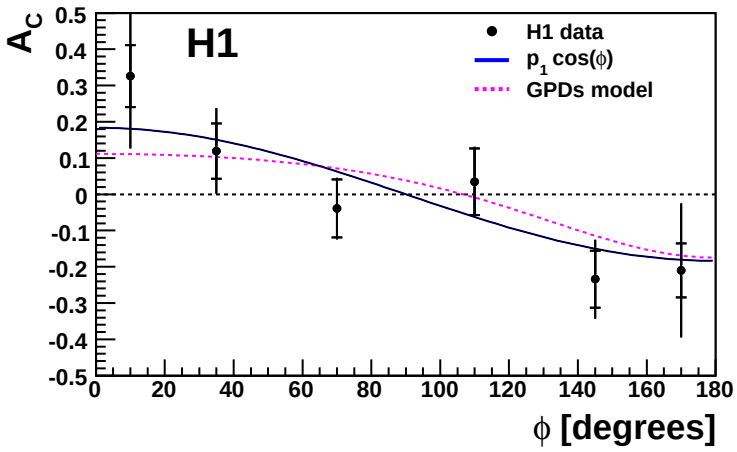

Figure 53: Beam charge asymmetry as a function of ϕ from H1 data [26]. Note that the ϕ convention chosen in H1 is different from HERMES (see text). The inner error bars represent the statistical errors, the outer error bars the statistical and systematic errors added in quadrature. A fit in $p_1 \cos\phi$ is presented, where p_1 is a free parameter (full line), together with the GPDs model prediction (dashed line).

DVCS amplitude.

Both experiments show that the present status of GPD models can correctly described the BCA measurements. In case of H1, factorized parameterizations of GPDs (in t) are the most simple choices compatible with measurements (see above), and for HERMES, the sensitivity of the hypothesis of the t-dependence is illustrated in Fig. 52.

If we consider the overall description in Fig. 52, the factorized ansatz (without D-term) is favored by HERMES BCA measurements. The so-called D-term is part of some parameterizations of GPDs [34]. That's why BCA, which provides a sensitivity the real part of the DVCS amplitude, gets a sensitivity to this (unknown) term. In general also, the factorized ansatz is much more stable with respect to the D-term contribution, when compared to the non-factorized (Regge) ansatz. Indeed, the spread between Regge with/without D-term predictions is huge, whereas the D-term has only a small impact on the factorized predictions. As the D-term is almost completely unknown, it is interesting to make choice of parameterizations (if possible) that can reduce their sensitivity to it.

In Ref. [34], it is mentioned that the Regge (without D-term) is favored, based on the observation of the t dependence. However, it is not that clear when considering all data points.

In any case, the experimental results presented in Fig. 52 and 53 are the first obtained on BCA and then important pieces to provide constraints on the real part of the amplitude in future developments of GPDs phenomenology. A compilation of H1 and HERMES results is presented in Fig. 54.

12.3 Experimental analysis of dispersion relations

A specific analysis has been done in the H1 experiment concerning the real part of the DVCS amplitude [26]. From Eq. (21) and measurements of BCA and DVCS cross section, it is possible to extract the ratio of the real to imaginary parts of the DVCS amplitude

$$\rho = \mathrm{Re}A_{DVCS}/\mathrm{Im}A_{DVCS}.$$

This ratio is a key quantity which can also be derived through a dispersion relation, which takes a simple form in the high energy limit. Indeed, at low x_{Bj}, when the W dependence of the DVCS cross

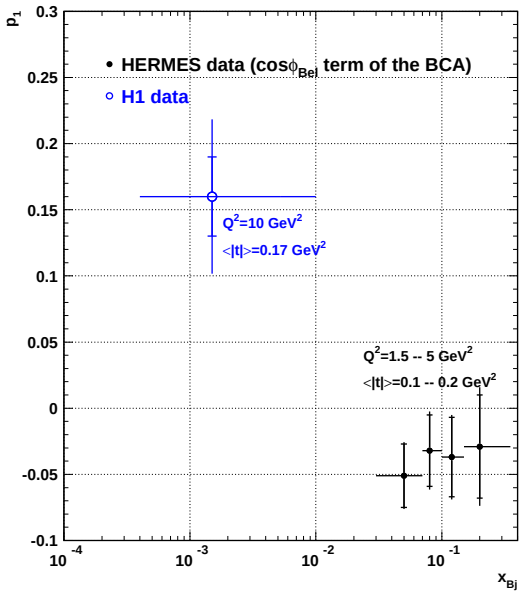

Figure 54: The beam charge asymmetry for H1 and HERMES is fitted by a the dominant harmonic in $p_1 \cos\phi$, where p_1 is a free parameter (see text). Results for p_1 are presented for both experiments as a function of x_{Bj}. This plot can be interpreted as a reflection of the different values of α' in both kinematic ranges, negligible value in the H1 domain and large value for HERMES. We understand immediately the great interest of COMPASS kinematical domain, lying at intermediate x_{Bj}.

section is dominated by a single term in W^δ (with $\delta > 0.3$), the dispersion relation can be written as

$$\mathrm{Re}A_{DVCS}/\mathrm{Im}A_{DVCS} = \tan\left(\frac{\pi\delta(Q^2)}{8}\right), \tag{22}$$

where $\delta(Q^2)$ is the power governing the W dependence of the DVCS cross section at a given Q^2. As we have measured δ independently from DVCS cross sections only [26] (see previous section), we can compute this ratio, with the very reasonable assumption that the dispersion relation are correct. We obtain: $\rho = 0.25 \pm 0.06$. To be compared to the value extracted from BCA measurement and the subsequent extraction of p_1, which gives $\rho = 0.23 \pm 0.08$. Both values are found in good agreement.

After this brief discussion, we can also understand simply how the sensitivity of the beam charge asymmetry observable is built with α'. The BCA is proportional to the ratio of real to imaginary part of the DVCS amplitude and this ratio can be expressed with respect to t as

$$\rho[t] = \mathrm{Re}A_{DVCS}/\mathrm{Im}A_{DVCS}[t] \simeq \mathrm{Re}A_{DVCS}/\mathrm{Im}A_{DVCS}[0](1 - \alpha'|t|).$$

Then, trivially, for small values of α' at low $|t|$ values, we do not expect much sensitivity (on α') of this ratio and thus of the BCA. This is what is illustrated for HERMES results in Fig. 54.

12.4 Jefferson Laboratory experiments

Regarding the kinematic coverage of fixed-target experiments (see Fig. 55), the Jefferson Lab (JLab) experiments play a major role in the field, exploring the large x_{Bj} and low Q^2 kinematic domain. JLab experiments, colliding an electron beam in the energy range of 6 GeV on a fixed target, can measure

beam spin or target spin asymmetries [35] and then access directly the imaginary part of the DVCS amplitude in the valence domain.

Of course, we can not exclude a priori that higher twists effects would completely spoil any perturbative treatment of the experimental results in this area. Below, we describe briefly few characteristic measurements at JLab related to GPDs physics.

First, let us recall that in this kinematic domain, the BH cross section is completely dominating the $ep \to ep\gamma$ cross section. Then, the DVCS signal can hardly be observed and only the BH/DVCS interference can be accessed through different observables with different sensitivities to GPDs [35].

An important recent result has been obtained by the Hall A E-00-110 experiment [35], which demonstrates that measurements at JLab are dominated by leading twists contributions. It is shown in Fig. 56. From the observed Q^2 scaling of the imaginary part of the DVCS amplitude (see Fig. 56) this result provides an indication that the measurement of the imaginary part of the DVCS amplitude follows a typical Bjorken scaling, observed over the Q^2 range covered by the experiment. Which means that leading twists terms are likely to dominate. Of course, the range in Q^2 accessible is not large but the the high precision of the data makes this last statement quite reasonable. An upgrade at larger energies of the lepton beam is obviously an important issue to get a sensitivity to higher Q^2 values (and larger W).

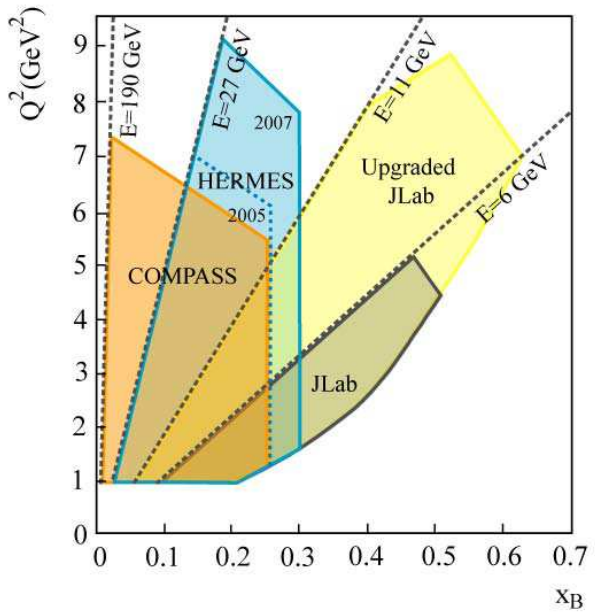

Figure 55: Kinematic coverage for fixed-target experiments: (i) COMPASS at 190 GeV; (ii) HERMES at 27.6 GeV, dotted line for existing data ($\leq$ 2005), solid line for future (2005-2007) data with an integrated luminosity higher by about one order of magnitude; (iii) JLAB experiments at 6 GeV, and at 11 GeV (after upgrade).

Apart from DVCS/BH interference measurements, a separation between BH and DVCS processes has been obtained with the Hall A E-00-110 experiment. The measurement of the 4-fold (polarized and unpolarized) differential cross sections $\frac{d\sigma}{dx_B dQ^2 dt d\phi}$ (for the real photon production process) has been done for three values of Q^2(in the kinematic domain $W \approx 2$ GeV and $x > 0.1$). Results are shown in Fig. 57 for $< Q^2 >$=2.3 GeV^2 [35]. The particular shape in ϕ of the unpolarized cross section (Fig. 57) is typical of the BH process. The dot-dot-dashed curve in Fig. 57 shows its precise shape and contribution. It can be seen that it dominates most of the cross sections and, only around $\Phi = 180^o$, there is a large discrepancy (a factor ≈ 2) between the BH and the data which could be attributed to the DVCS process

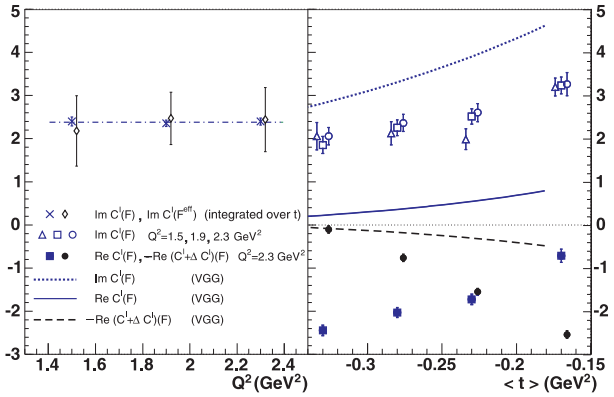

Figure 56: Q^2 dependence of imaginary part of the DVCS amplitude (left). We observe a scaling over the range in Q^2 covered by the analysis.

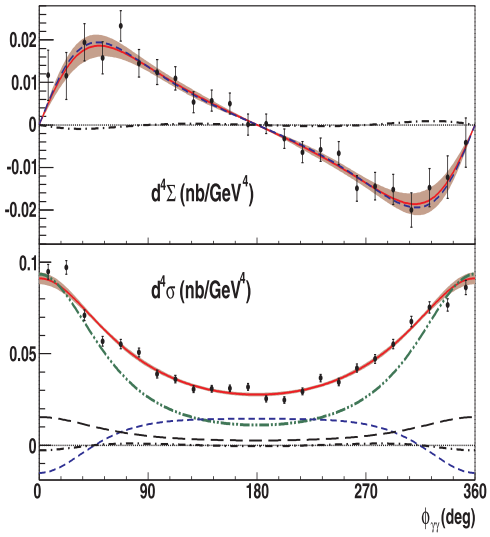

Figure 57: Difference of (beam) polarized cross sections for DVCS on the proton, as a function of the Φ angle, measured by the JLab Hall A collaboration. The average kinematics is $< x_{Bj} >$=0.36, $< Q^2 >$=2.3 GeV^2 and $< -t >$=0.28 GeV^2. The figure on the bottom shows the total (i.e unpolarized) cross section as a function of Φ. The BH contribution is represented by the dot-dot-dashed curve.

itself. It opens a possibility in a future analysis to extract directly a DVCS signal, which would be a first time measurement in this kinematic range.

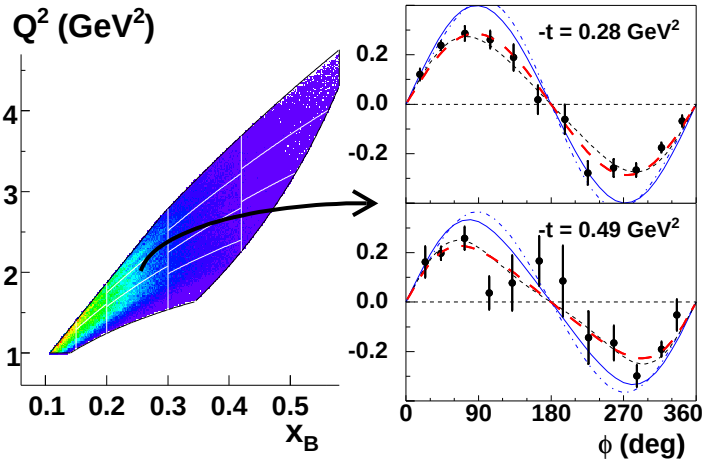

Figure 58: Left: kinematic coverage and binning in the (x_B, Q^2) space. Right: Beam spin asymmetry $A(\phi)$ for 2 of the 62 (x_B, Q^2, t) bins, corresponding to $\langle x_B \rangle = 0.249$, $\langle Q^2 \rangle = 1.95$ GeV^2, and two values of $\langle t \rangle$. The long-dashed curves correspond to fits with $A = \frac{a \sin\phi}{1+c\cos\phi}$. The dashed curves correspond to a Regge calculation. GPDs calculations are also shown as full lines.

Let us present a final measurement from the (JLab) Hall B E-00-113 experiment, concerning beam spin asymmetries (BSAs) [35], which shows (again) clearly the interest for an upgrade at larger energies. Results are presented in Fig. 58 with GPDs or Regge (non-perturbative) models. The asymmetries are fitted according to the relation

$$A = \frac{a \sin\phi}{1 + c\cos\phi + d\cos 2\phi} \tag{23}$$

and extracted values of a are displayed in Fig. 59. As can be seen in Fig. 59, the discrimination of Regge (soft) or GPDs (hard) approaches is not conclusive from the present data. Therefore, the upgrade with 12 GeV electrons is very interesting to address this separation between soft and hard physics at JLab.

12.5 Experimental prospects on the orbital angular momentum of partons

A final comment is in order concerning the measurement of asymmetries (from DVCS/BH interference) in fixed target experiments. Experiments at JLab and data collected by HERMES allow to determine transverse target-spin asymmetries, by controlling the polarization of the target. This would be also a possibility of the future COMPASS project described above. Experimentally, we need to introduce another azimuthal angle ϕ_S to characterize completely the events measured in such configurations, where ϕ_S represents the direction of the spin of the target with respect to the plane of the leptons (incident and scattered).

The great interest is then that the $\cos\phi$ moment of the asymmetry $d\sigma(\phi, \phi_S) - d\sigma(\phi, \phi_S + \pi)$ is proportional to the imaginary part of GPDs of types H and E. Remind the short note we have written in the last section: the contribution of GPDs of type E are damped by kinematic factors of orders $|t|/M_p^2$ in all the observables we have discussed till now. This is not the case for transverse target-spin asymmetries.

Therefore, these measurements are particularly interesting in the quest for GPDs. The strong interest in determining GPDs of type E is that these functions appear in a fundamental relation between GPDs and angular momenta of partons. Indeed, GPDs have been shown to be related directly to the total

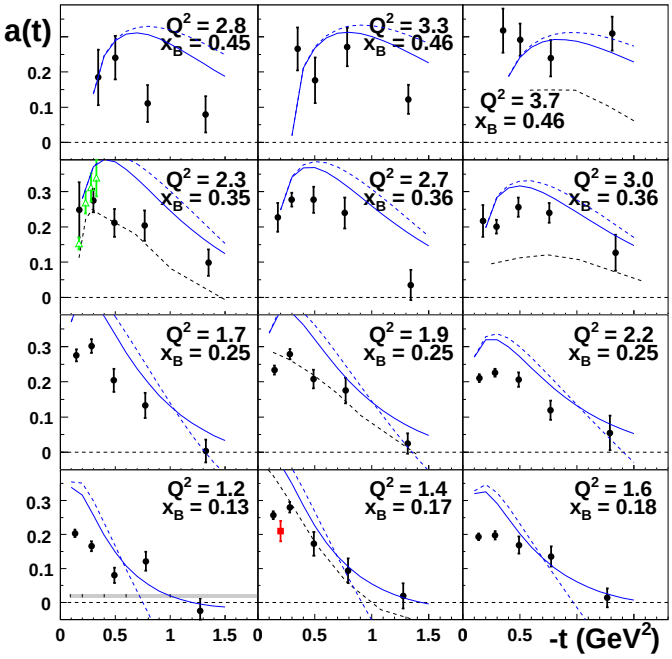

Figure 59: Extracted values a of the DVCS-BH interference as measured in a spin asymmetry, with $A = \frac{a \sin\phi}{1+c\cos\phi+d\cos 2\phi}$. They are shown as a function of $-t$ for different bins in (x_B, Q^2). The solid curves represent a GPD model and the dashed curves a Regge approach.

angular momenta carried by partons in the nucleon, via the Ji relation [29]

$$\frac{1}{2}\int_{-1}^{1} dx x \left(H_q(x,\xi,t) + E_q(x,\xi,t)\right) = J_q. \tag{24}$$

As GPDs of type E are essentially unknown apart from basic sum rules, any improvement of their knowledge is essential. From Eq. (24), it is clear that we could access directly to the orbital momentum of quarks if we had a good knowledge of GPDs H and E. Indeed, J_q is the sum of the longitudinal angular momenta of quarks and their orbital angular momenta. The first one is relatively well known through global fits of polarized structure functions. It follows that a determination of J_q can provide an estimate of the orbital part of its expression. In Ji relation (Eq. (24)), the function H is not a problem as we can take its limit at $\xi = 0$, where H merges with the PDFs, which are well known. But we need definitely to get a better understanding of E.

First measurements of transverse target-spin asymmetries have been realized at JLab [35] and HERMES [34]. We present results obtained by HERMES [34] in Fig. 60. The typical sensitivity to hypothesis on J_q values is also illustrated in Fig. 60, with the reserve that in this analysis, the observed sensitivity to J_q is model dependent. It is already a first step, very challenging from the experimental side. Certainly, global fits of GPDs (if possible) would give a much more solid (less model dependent) sensitivity to J_q (see next section).

12.6 A few comments on the Ji relation

In order to give more intuitive content to the Ji relation (24), we can comment further its dependence in the function E. From our short presentation of GPDs, we know that functions of type E are related to matrix elements of the form $\langle p', s'|\mathcal{O}|p, s\rangle$ for $s \neq s'$, which means helicity flip at the proton vertex ($s \neq s'$). That's why their contribution vanish in standard DIS or in processes where t tends to zero.

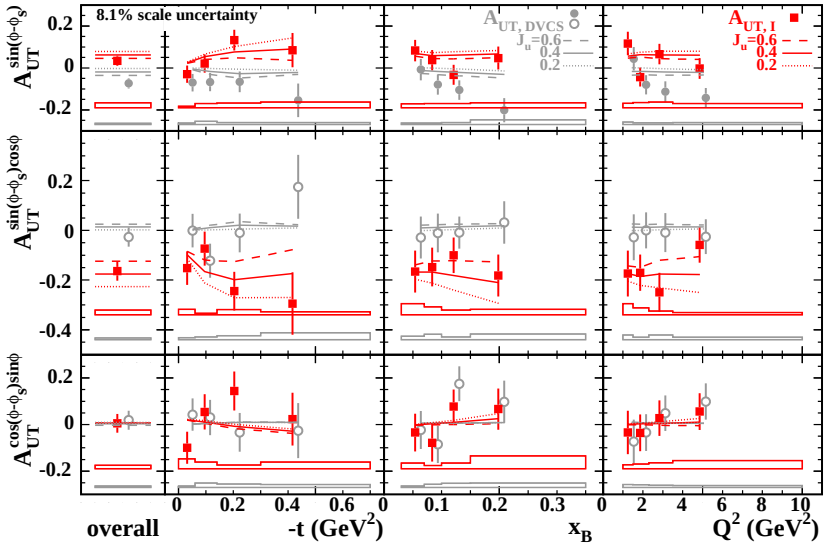

Figure 60: Target-spin asymmetry amplitudes describing the dependence of the squared DVCS amplitude (circles, $A_{\mathrm{UT,DVCS}}$) and the interference term (squares, $A_{\mathrm{UT,I}}$) on the transverse target polarisation. In the notations, U refers to Unpolarized beam and T to Transversely polarized target. The circles (squares) are shifted right (left) for visibility. The curves are predictions of a GPD model with three different values for the u-quark total angular momentum J_u and fixed d-quark total angular momentum $J_d = 0$ (see [34]). This is a first important (model dependent) check of the sensitivity these data to the Ji relation.

More generally, their contribution would vanish if the proton had only configurations where helicities of the partons add up to the helicity of the proton. In practice, this is not the case due to angular momentum of partons. This is what is reflected in a very condensed way in the Ji relation (Eq. (24)).

Then, we get the intuitive interpretation of this formula: it connects E with the angular momentum of quarks in the proton. A similar relation holds for gluons [29], linking J_g to H_g and E_g and both formulae, for quarks and gluons, add up to build the proton spin

$$J_q + J_g = 1/2.$$

This last equality must be put in perspective with the asymptotic limits for J_q and J_g at large scale Q^2, which read $J_q \to \frac{1}{2}\frac{3n_f}{16+3n_f}$ and $J_g \to \frac{1}{2}\frac{16}{16+3n_f}$, where n_f is the number of active flavors of quarks at that scale (typically $n_f = 5$ at large scale Q^2) [29].

In words, half of the angular momentum of the proton is carried by gluons (asymptotically). It is not trivial to make quantitative estimates at medium scales, but it is a clear indication that orbital angular momentum plays a major role in building the angular momentum of the proton. It implies that all experimental physics issues that intend to access directly or indirectly to GPDs of type E are essential in the understanding of the proton structure, beyond what is relatively well known concerning its longitudinal momentum structure in x_{Bj}. And that's also why first transverse target-spin asymmetries (which can provide the best sensitivity to E) are so important and the fact that such measurements have already been done is promising for the future.

Clearly, we understand at this level the major interest of GPDs and we get a better intuition on their physics content. They simultaneously probe the transverse and the longitudinal distribution of quarks and gluons in a hadron state and the possibility to flip helicity in GPDs makes these functions sensitive to orbital angular momentum in an essential way. This is possible because they generalize the purely collinear kinematics describing the familiar twist-two quantities of the parton model. This is obviously illustrating a fundamental feature of non-forward exclusive processes.

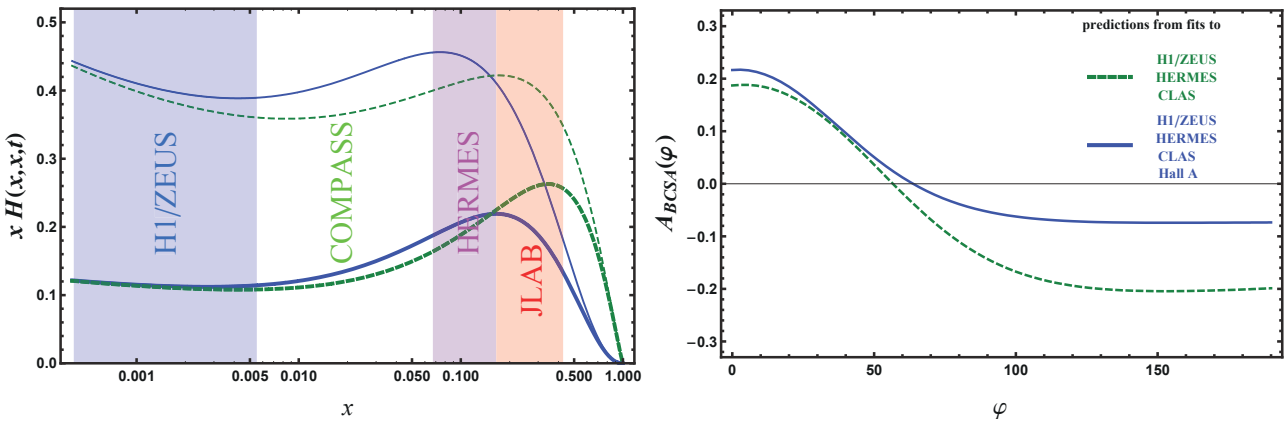

Figure 61: (a) Global GPD fits at $t = -0.3$ GeV^2 (thick) and $t = 0$ (thin) are displayed as dashed and solid lines, respectively. (b) Prediction of the BCA for COMPASS kinematics ($E_\mu = 160$ GeV, $\mathcal{Q}^2 = 2$ GeV^2, $t = -0.2$ GeV^2) [30].

12.7 Towards global fits in the GPDs context

A direct continuation of the analysis exposed in the previous section is to perform a global fit of all previous experimental results. In the same spirit as it is done for global QCD fits of proton structure function data, obtained in DIS scattering, a global fit can be done of observables measured for exclusive processes, like exclusive real gamma production. Instead of defining initial conditions on PDFs (at a low scale Q_0), initial conditions on GPDs must be assumed. An important step in this direction is presented in Ref.[30].

A typical result derived in this work is displayed in Fig. 61. The GPD of type H is shown for two values of t (see Fig.61-left-) and the influence of JLab results is illustrated on the prediction of the BCA in the COMPASS kinematics (see Fig.61-right-).

From these global GPDs fits [30], the impact parameter space distribution can be extracted with

$$\rho(r_T, x, \mathcal{Q}^2) = \frac{\int_{-\infty}^{\infty} d^2\vec{\Delta}\; e^{i\vec{\Delta}\vec{r_T}} H(x, \eta = 0, t = -\vec{\Delta}^2, \mathcal{Q}^2)}{\int_{-\infty}^{\infty} d^2\vec{\Delta}\; H(x, \eta = 0, t = -\vec{\Delta}^2, \mathcal{Q}^2).} \tag{25}$$

Results obtained in Ref.[30] confirms what we have already discussed in previous sections [31]. This theoretical framework to analyze GPDs is a promising trend for the future, in parallel to the production of new experimental measurements.

13 Outlook

We have reviewed the most recent experimental results from hard diffractive scattering at HERA and Tevatron. We have shown that many aspects of diffraction in ep collisions can be successfully described in QCD if a hard scale is present. A key to this success are factorization theorems, which render parts of the dynamics accessible to calculation in perturbation theory. The remaining non-perturbative quantities, namely diffractive PDFs and generalized parton distributions, can be extracted from measurements and contain specific information about small-x_{Bj} partons in the proton that can only be obtained in diffractive processes. To describe hard diffractive hadron-hadron collisions is more challenging since factorization is broken by re-scattering between spectator partons. These re-scattering effects are of interest in their own right because of their intimate relation with multiple scattering effects, which at LHC energies are expected to be crucial for understanding the structure of events in hard collisions.

A combination of data on inclusive and diffractive ep scattering hints at the onset of parton saturation at HERA, and the phenomenology developed there is a helpful step towards understanding high-density effects in hadron-hadron collisions. In this respect, we have discussed a very important aspect that makes diffraction in DIS so interesting at low x_{Bj}. Its interpretation in the dipole formalism and its connection to saturation effects. Indeed, diffraction in DIS has appeared as a well suited process to analyze saturation effects at large gluon density in the proton. In the dipole model, it takes a simple and luminous form, with the introduction of the so-called saturation scale Q_s. Diffraction is then dominated by dipoles of size $r \sim 1/Q_s$. In particular, it provides a simple explanation of the constance of the ratio of diffractive to total cross sections as a function of W (at fixed Q^2 values).

Then, exclusive processes in DIS, like VMs production or DVCS, have appeared as key reactions to trigger the generic mechanism of diffractive scattering. Decisive measurements have been performed recently, in particular concerning dependences of exclusive processes cross section within the momentum exchange (squared) at the proton vertex, t. This allows to extract first experimental features concerning proton tomography, on how partons are localized in the proton. It provides a completely new information on the spatial extension of partons inside the proton (or more generally hadrons), as well as on the correlations of longitudinal momenta. A unified picture of this physics is encoded in the GPDs formalism. We have shown that Jefferson laboratory experiments or prospects at COMPASS are essential, to gain relevant information on GPDs. Of course, we do not forget that the dependence of GPDs on three kinematical variables, and the number of distributions describing different helicity combinations present a considerable complexity. In a sense this is the price to pay for the amount of physics information encoded in these quantities. It is however crucial to realize that for many important aspects we need not fully disentangle this complexity. The relation of longitudinal and transverse structure of partons in a nucleon, or of nucleons in a nucleus, can be studied quantitatively from the distribution in the two external kinematical variables x_{Bj} and t.

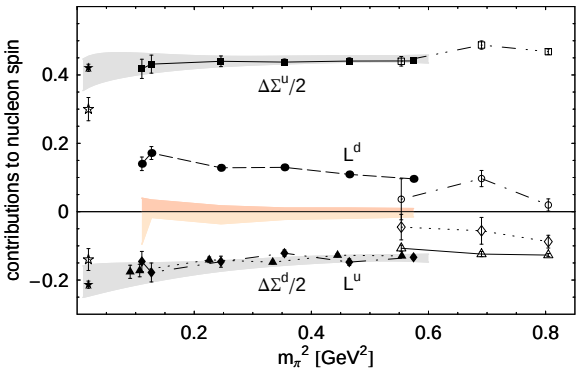

Figure 62: Quark spin and orbital angular momentum contributions to the spin of the nucleon for up and down quarks. Squares and triangles denote $\Delta\Sigma^u$ and $\Delta\Sigma^d$ respectively, and diamonds and circles denote L^u and L^d respectively [37].

To conclude, we can illustrate these issues with results from lattice QCD [37]. In Ref. [37], lattice QCD calculations are performed. They show two remarkable features of the quark contributions to the nucleon spin. The first is that the magnitude of the orbital angular momentum contributions of the up and down quarks, L^u and L^d, are separately quite substantial, and yet they cancel nearly completely (see Fig. 62). The second is the close cancellation between the orbital and spin contributions of the d quarks, L^d and $\Delta\Sigma^d/2$. Of course, we can not take these results as granted but calculations are solid. It would be obviously valuable to understand the physical origin of both features, with more data.

References

[1] M. Derrick *et al.* [ZEUS Collaboration], Z. Phys. C **68** (1995) 569;
C. Adloff *et al.* [H1 Collaboration], Z. Phys. C **76** (1997) 613.

[2] S. Chekanov *et al.* [ZEUS Collaboration], Eur. Phys. J. **C38** (2004) 43; Nucl. Phys. **B713** (2005) 3;
A. Aktas *et al.* [H1 Collaboration], Eur. Phys. J. C **48** (2006) 715; Eur. Phys. J. C **48** (2006) 749;
E. Sauvan, Published in Tsukuba 2006, Deep inelastic scattering 211-214, arXiv:hep-ex/0607038.

[3] S. Chekanov [ZEUS Collaboration], Nucl. Phys. B **800** (2008) 1;
P. Newman and M. Ruspa, arXiv:0903.2957 [hep-ex].

[4] D. Salek, to be published in the proceedings of the 17th International Workshop on Deep Inelastic Scattering and Related Subjects (DIS2009), Madrid, Spain, April 2009.

[5] J. C. Collins, Phys. Rev. D **57** (1998) 3051 [Erratum-ibid. D **61** (2000) 019902].

[6] G. Ingelman and P. E. Schlein, Phys. Lett. B **152** (1985) 256.

[7] L. Schoeffel, Nucl.Instrum.Meth. **A423** (1999) 439;
C. Royon, L. Schoeffel, J. Bartels, H. Jung and R. B. Peschanski, Phys. Rev. D **63** (2001) 074004;
J. Lamouroux, R. B. Peschanski, C. Royon and L. Schoeffel, Nucl. Phys. B **649** (2003) 312;
C. Royon, L. Schoeffel, R. B. Peschanski and E. Sauvan, Nucl. Phys. B **746** (2006) 15; Nucl. Phys. B **781** (2007) 1.

[8] K. J. Golec-Biernat and A. Luszczak, Phys. Rev. D **76** (2007) 114014.

[9] CDF Collaboration, Phys. Rev. Lett. **88** (2002) 151802.

[10] CDF Collaboration, Phys. Rev. Lett. **84** (2000) 5043; Phys. Rev. Lett. **87** (2001) 141802.

[11] C. Royon, Acta Phys. Polon. B **37** (2006) 3571.

[12] M. Rangel, C. Royon, G. Alves, J. Barreto, R. Peschanski, Nucl. Phys. B**774** (2007) 53.

[13] CDF Collaboration, Phys. Rev. Lett. **99** (2007) 242002.

[14] CDF Collaboration, hep-ex/0712.0604.

[15] O.Kepka, C. Royon, Phys. Rev.D **76** (2007) 034012.

[16] FP420 Coll., see http://www.fp420.com; AFP TDR in ATLAS to be submitted; see: http://project-rp220.web.cern.ch/project-rp220/index.html; C. Royon, preprint arXiv:0706.1796, proceedings of 15th International Workshop on Deep-Inelastic Scattering and Related Subjects (DIS2007), Munich, Germany, 16-20 Apr 2007.

[17] A.H. Mueller, Nucl. Phys. **B335** (1990) 115;
N.N. Nikolaev and B.G. Zakharov, Zeit. für. Phys. **C49** (1991) 607.

[18] A. Bialas and R. Peschanski, Phys. Lett. **B378** (1996) 302; Phys. Lett. **B387** (1996) 405;
H. Navelet, R. Peschanski, C. Royon, S. Wallon, Phys. Lett. B **385** (1996) 357;
H. Navelet, R. Peschanski, C. Royon, Phys. Lett. B366 (1996) 329;
A. Bialas, R. Peschanski, C. Royon, Phys. Rev. D **57** (1998) 6899;
S. Munier, R. Peschanski, C. Royon, Nucl. Phys. B **534** (1998) 297;
E. Iancu, K. Itakura and S. Munier, Phys. Lett. B **590** (2004) 199.

[19] C. Marquet, R. B. Peschanski and G. Soyez, Nucl. Phys. A **756** (2005) 399; Phys. Rev. D **76** (2007) 034011.

[20] K. J. Golec-Biernat and M. Wusthoff, Phys. Rev. D **59** (1999) 014017; Phys. Rev. D **60** (1999) 114023;
A. M. Staśto, K. Golec-Biernat and J. Kwieciński, Phys. Rev. Lett. **86** (2001) 596;
J. Bartels, K. J. Golec-Biernat and H. Kowalski, Phys. Rev. D **66** (2002) 014001;
K. Golec-Biernat and S. Sapeta, Phys. Rev. **D74** (2006) 054032.

[21] C. Marquet and L. Schoeffel, Phys. Lett. B **639** (2006) 471.

[22] J. Breitweg et al. [ZEUS Collaboration], Eur. Phys. J. **C 2**, 2 (1998);
M. Derrick et al. [ZEUS Collaboration], Eur. Phys. J. **C 6**, 603 (1999);
C. Adloff et al. [H1 Collaboration], Eur. Phys. J. **C 13**, 371 (2000);
S. Chekanov *et al.* [ZEUS Collaboration], PMC Phys. A **1** (2007) 6.

[23] C. Adloff et al. [H1 Collaboration], Phys. Lett. **B 483**, 360 (2000);
S. Chekanov et al. [ZEUS Collaboration], Nucl. Phys. **B 718**, 3 (2005).

[24] S. Chekanov et al. [ZEUS Collaboration], Nucl. Phys. **B 695**, 3 (2004);
A. Aktas et al. [H1 Collaboration], Eur. Phys. J. **C 46**, 585 (2006).

[25] J. Breitweg *et al.* [ZEUS Collaboration], Phys. Lett. B **437** (1998) 432;
C. Adloff *et al.* [H1 Collaboration], Phys. Lett. B **483** (2000) 23.

[26] C. Adloff *et al.* [H1 Collaboration], Phys. Lett. B **517** (2001) 47;
A. Aktas *et al.* [H1 Collaboration], Eur. Phys. J. C **44** (2005) 1;
F. D. Aaron *et al.* [H1 Collaboration], Phys. Lett. B **659** (2008) 796; arXiv:0907.5289 [hep-ex].

[27] P. R. B. Saull [ZEUS Collaboration], arXiv:hep-ex/0003030;
S. Chekanov *et al.* [ZEUS Collaboration], Phys. Lett. B **573** (2003) 46; JHEP **0905** (2009) 108.

[28] M. Diehl, Eur. Phys. J. C **25** (2002) 223 [Erratum-ibid. C **31** (2003) 277];
J. P. Ralston and B. Pire, Phys. Rev. D **66**, 111501 (2002);
M. Burkardt, Int. J. Mod. Phys. A **18** (2003) 173;
A. V. Belitsky, X. d. Ji and F. Yuan, Phys. Rev. D **69** (2004) 074014;
L. Frankfurt, M. Strikman and C. Weiss, Ann. Rev. Nucl. Part. Sci. **55** (2005) 403.

[29] X. D. Ji, Phys. Rev. Lett. **78** (1997) 610; Phys. Rev. **D55** (1997) 7114;
M. Diehl, T. Gousset, B. Pire and J. P. Ralston, Phys. Lett. B **411** (1997) 193;
L. L. Frankfurt, A. Freund and M. Strikman, Phys. Rev. D **58** (1998) 114001 [Erratum-ibid. D **59** (1999) 119901];
A. G. Shuvaev, K. J. Golec-Biernat, A. D. Martin and M. G. Ryskin, Phys. Rev. D **60** (1999) 014015;
K. Goeke et al., Prog. Part. Nucl. Phys. **47**, 401 (2001);
A. V. Belitsky, D. Mueller and A. Kirchner, Nucl. Phys. B **629** (2002) 323;
M. Diehl, Phys. Rept. **388**, 41 (2003);
A. V. Belitsky and A. V. Radyushkin, Phys. Rept. **418**, 1 (2005).

[30] K. Kumerički, D. Mueller and K. Passek-Kumerički, Eur. Phys. J. C **58** (2008) 193;
K. Kumericki and D. Muller, arXiv:0904.0458 [hep-ph].

[31] M. Diehl, T. Feldmann, R. Jakob and P. Kroll, Eur. Phys. J. C **39** (2005) 1.

[32] L. Schoeffel, Phys. Lett. B **658** (2007) 33.

[33] L. L. Frankfurt, A. Freund and M. Strikman, Phys. Lett. B **460** (1999) 417.

[34] A. Airapetian *et al.* [HERMES Collaboration], Phys. Rev. Lett. **87** (2001) 182001; Phys. Rev. D **75** (2007) 011103; JHEP **0806** (2008) 066.

[35] S. Stepanyan *et al.* [CLAS Collaboration], Phys. Rev. Lett. **87** (2001) 182002;
C. Munoz Camacho *et al.* [Jefferson Lab Hall A Collaboration and Hall A DVCS Collaboration], Phys. Rev. Lett. **97** (2006) 262002;
S. Chen *et al.* [CLAS Collaboration], Phys. Rev. Lett. **97** (2006) 072002;
F. X. Girod *et al.* [CLAS Collaboration], Phys. Rev. Lett. **100** (2008) 162002.

[36] N. d'Hose et al., Nucl. Phys. A **711** (2002) 160.

[37] Ph. Hagler *et al.* [LHPC Collaborations], Phys. Rev. D **77** (2008) 094502.